

University of Denver

Digital Commons @ DU

Electronic Theses and Dissertations

Graduate Studies

1-1-2012

Plasma Spectroscopic Techniques Applied to Biological and Environmental Matrices

Morgan Steele Schmidt
University of Denver

Follow this and additional works at: <https://digitalcommons.du.edu/etd>

 Part of the [Analytical Chemistry Commons](#)

Recommended Citation

Schmidt, Morgan Steele, "Plasma Spectroscopic Techniques Applied to Biological and Environmental Matrices" (2012). *Electronic Theses and Dissertations*. 921.
<https://digitalcommons.du.edu/etd/921>

This Dissertation is brought to you for free and open access by the Graduate Studies at Digital Commons @ DU. It has been accepted for inclusion in Electronic Theses and Dissertations by an authorized administrator of Digital Commons @ DU. For more information, please contact jennifer.cox@du.edu, dig-commons@du.edu.

PLASMA SPECTROSCOPIC TECHNIQUES APPLIED TO BIOLOGICAL AND
ENVIRONMENTAL MATRICES

A Dissertation

Presented to

the Faculty of Natural Sciences and Mathematics

University of Denver

In Partial Fulfillment

of the Requirements for the Degree

Doctor of Philosophy

by

Morgan S. Schmidt

June 2012

Advisor: Keith E. Miller

©Copyright by Morgan S. Schmidt 2012

All Rights Reserved

Author: Morgan S. Schmidt

Title: PLASMA SPECTROSCOPIC TECHNIQUES APPLIED TO BIOLOGICAL AND ENVIRONMENTAL MATRICES

Advisor: Keith E. Miller

Degree Date: June 2012

Abstract

The purpose of this research was to apply the use of direct ablation plasma spectroscopic techniques, including spark-induced breakdown spectroscopy (SIBS) and laser-induced breakdown spectroscopy (LIBS), to a variety of environmental matrices. These were applied to two different analytical problems. SIBS instrumentation was adapted in order to develop a fieldable monitor for the measurement of carbon in soil. SIBS spectra in the 200 nm to 400 nm region of several soils were collected, and the neutral carbon line (247.85 nm) was compared to total carbon concentration determined by standard dry combustion analysis. Additionally, Fe and Si were evaluated in a multivariate model in order to determine their impacts on the model's predictive power for total carbon concentrations. The results indicate that SIBS is a viable method to quantify total carbon levels in soils; obtaining a good correlation between measured and predicated carbon in soils. These results indicate that multivariate analysis can be used to construct a calibration model for SIBS soil spectra, and SIBS is a promising method for the determination of total soil carbon.

SIBS was also applied to the study of biological warfare agent simulants. Elemental compositions (determined independently) of bioaerosol samples were compared to the SIBS atomic (Ca, Al, Fe and Si) and molecular (CN, N₂ and OH)

emission signals. Results indicate a linear relationship between the temporally integrated emission strength and the concentration of the associated element.

Finally, LIBS signals of hematite were analyzed under low pressures of pure CO₂ and compared with signals acquired with a mixture of CO₂, N₂ and Ar, which is representative of the Martian atmosphere. This research was in response to the potential use of LIBS instrumentation on the Martian surface and to the challenges associated with these measurements. Changes in Ca, Fe and Al lineshapes observed in the LIBS spectra at different gas compositions and pressures were studied. It was observed that the size of the plasma formed on the hematite changed in a non-linear way as a function of decreasing pressure in a CO₂ atmosphere and a simulated Martian atmosphere.

Acknowledgements

I wish to thank Keith Miller and Amy Bauer for their support through my tenure at the University of Denver. I want to thank Keith for his guidance throughout the soil project. His insight and discussions on this project were invaluable. I want to thank Amy for introducing me to the LIBS community, which provided several opportunities to present at the LIBS conferences. These experiences built friendships and business partnerships that I hope will last a lifetime.

I wish to thank PSI for supporting the research on the SIBS analysis of carbon in soil through the Department of Energy under contract DE-SC0001591.

I also need to thank the constant support of my family and friends, especially Mark Schmidt for his unwavering encouragement and patience during my time at the University of Denver.

Table of Contents

CHAPTER 1 : INTRODUCTION	1
1.2 Development of SIBS and Literature Review	4
1.2.1 SIBS Emission Measurements of Air	4
1.2.2 SIBS to Monitor Metals in Soils.....	10
1.3 Comparison of SIBS and LIBS.....	11
1.4 Need and Research Objectives.....	12
1.4.1 Specific Research Goals	12
1.4.2 Methods of Detection of Carbon in Soils with Ablation Techniques	15
1.4.3 Methods of Detection of BWAs with Ablation Techniques	18
1.4.4 Use of LIBS to Study Plasma Properties under Low Pressure	20
1.5 Study Design and Dissertation Format	21
CHAPTER 2 : REVIEW OF ATOMIC EMISSION SPECTROSCOPY	23
2.1 The History of Atomic Spectroscopy	23
2.2 An Introduction to Electronic Structure and Hydrogenic Atoms	25
2.3 Multi-Electronic Atoms	31
2.4 Radiation of Atomic and Molecular Species	32
2.5 The Shapes of Emission Spectral Features	33
2.5.1 Line Spectra	33
2.5.2 Band Spectra and Diatomic Molecules.....	36
2.6 Spectral Intensities of Lines.....	39
2.6.1 Continuum Emission.....	39
2.7 Spectral Line Broadening	40
2.7.1 Stark Line Broadening	41
2.7.2 Self-Absorption.....	42
CHAPTER 3 : PLASMA PHYSICS.....	44
3.1 An Introduction to Laser-Matter Interactions	45
3.2 Plasma Fundamentals.....	46
3.3 Plasma Shielding.....	47
3.4 Plasma Models	50
3.4.1 Plasmas Having Local Thermodynamic Equilibrium.....	50
3.5 Plasma Spectral Emission.....	51
3.5.1 Continuum Emission.....	52
3.5.2 Electron Density.....	58
3.5.3 Plasma Opacity	59
3.5.4 Plasma Temperature.....	60
CHAPTER 4 : DEVELOPMENT OF EARLY SOIL CARBON ANALYSIS BY SIBS.....	62
4.1 Rationale of Soil Carbon Analysis by SIBS	62

4.2 Preliminary Soil Carbon Analysis	65
4.2.1 Soil Processing and Characterization.....	66
4.2.2 Instrumentation and Soil Delivery	69
4.2.3 Establishment of the Optimal Spectral Region for Analysis	73
4.2.4 Collection Conditions	79
4.3 Regression Analysis.....	79
4.4 Regression Analysis Results.....	81
4.5 Chapter Conclusions	84
CHAPTER 5 : THE DEVELOPMENT OF A SIBS PORTABLE SOIL CARBON ANALYZER....	85
5.1 Introduction.....	85
5.2 Experimental Design.....	87
5.2.1 Soil Processing and Characterization.....	87
5.2.2 Surrogate Soil Analysis.....	93
5.2.3 Construction of Samples for Curves of Growth (COG) Experiments	95
5.3 Sample Delivery – Impact of Particle Size	98
5.4 Instrumentation of Soil Analysis	99
5.4.1 Initial SIBS Screw-Feed Instrumentation	100
5.4.2 Miniaturization of SIBS Instrumentation.....	103
5.5 Data Processing and Statistical Model Development	106
5.5.1 Initial Regression Analysis	106
5.5.2 Initial Regression Analysis on Portable SIBS Instrument	109
5.5.3 Incorporation of the CN (B-X) to the Development of a Multivariate Model	109
5.6 Results.....	110
5.6.1 Surrogate Soil Response Curve Results.....	110
5.6.2 Results of Particle Size	117
5.6.3 Univariate Results of Soil Carbon Analysis	124
5.6.4 Initial Multivariate Regression Analysis Results.....	128
5.6.5 Replication of Regression Analysis on the Portable SIBS Instrument	135
5.6.6 The Inclusion of TC, IC and OC.....	138
5.7 Chapter Conclusions and Future Work.....	142
CHAPTER 6 : PRELIMINARY CORRELATIONS OF FEATURE STRENGTH IN SIBS OF BIOAEROSOLS	144
6.1 Introduction.....	144
6.2 Bioaerosol Generation and Instrument Design	146
6.3 Preliminary Electrode Position Correlations	150
6.4 SIBS of Bioaerosol Samples.....	152
6.4.1 Biological Simulants.....	152
6.4.2 Data Acquisition of Three Bioaerosols.....	153
6.5 Results.....	153
6.5.1 Electrode Position Results	154
6.5.2 Elemental Composition Results.....	157
6.5.3 SIBS Atomic and Molecular Features	159

6.5.4 Spectral Results.....	161
6.6 Chapter Conclusions	171
CHAPTER 7 : LIBS SPECTROSCOPIC STUDIES OF HEMATITE IN SIMULATED MARTIAN ATMOSPHERE	173
7.1 Introduction.....	173
7.2 Experimental Design.....	175
7.2.1 Establishment of Early LIBS Experiments	176
7.2.2 Experimental Design Comparing Earth, CO ₂ and Mars Atmospheres	180
7.3 Results.....	185
7.3.1 Results of a Pure CO ₂ Atmosphere.....	185
7.3.2 Results of LIBS Spectra under Earth, CO ₂ and Martian Atmospheres.....	193
7.4 Chapter Conclusions and Future Research	203
CHAPTER 8 : CONCLUSIONS AND FUTURE WORK.....	205
8.1 The Development of a Portable SIBS Analyzer	205
8.2 The Use of SIBS to Study Bioaerosols	208
8.3 Plasma Dynamics as a Function of Pressure and Atmospheric Composition	212
WORKS CITED	214

List of Figures

Figure 1.1 Schematic diagram of the incinerator simulator test configuration adapted from Hunter <i>et al.</i> , 2000 [8].	8
Figure 2.1 Energy level diagram of a hydrogen atom adapted from Singh and Thakur, 2007 [4].	27
Figure 2.2 Typical transitions seen in an atom or ion which gives rise to optical emission. Adapted from Cremers, 2006 [5].	30
Figure 2.3 Energy level diagram of (A) atomic emission lines of Ca II atom, and (B) an example of a molecular emission profile. Adapted from Skoog, 2007 [1].	35
Figure 2.4 Sample spectrum of atomic emission lines including C (I), Si (I) and Fe (I).	35
Figure 2.5 Potential energy curve of the observed electronic states of the CN molecule adapted from Herzberg, 1950 [58].	38
Figure 3.1 Schematic diagram of expanding laser produced plasma in ambient gas. The plasma plume has several zones, all of which are labeled. The plasma temperature cools with increased distance from point of impact. Adapted from Singh and Thakur, 2007 [4].	49
Figure 3.2 A schematic overview of the temporal profile of a LIBS plasma derived from a single laser pulse. Adapted from Cremers, 2006 [5].	54
Figure 3.3 Dynamics of the emission from the GRX-2 sample measured upon excitation at 1064 nm as a function of the delay from the laser pulse. The gate width is fixed at 1 μ s. Reprinted with permission from Springer Publishing Company [83].	57
Figure 4.1 Schematic diagram of SIBS design for soil analysis. Soil falls from the syringe into the funnel and through the spark gap.	72
Figure 4.2 A sample spectrum of activated charcoal in the wavelength region of 248 nm, with a 20 μ s delay time. The C (I) line is labeled.	75
Figure 4.3 A sample spectrum of LECO synthetic carbon standard (0.53 %) in the wavelength region of 193 n, with a 20 μ s delay time. The C (I) line is labeled, as well as the nearby O and N features.	75
Figure 4.4 A sample spectrum of LECO synthetic carbon standard (0.53%) in the wavelength region of 248 nm, with a 20 μ s delay time. The C (I) line is labeled.	76

Figure 4.5 A sample spectrum of soil A in the 248 nm wavelength region, with a 20 μ s delay time. The C (I) line is labeled.....	76
Figure 4.6 A sample spectrum of soil A in the 355 to 395 nm region, with a 20 μ s delay time. The CN vibrational features of interest are labeled.	78
Figure 4.7 Measured vs. predicted carbon % levels from PLS analysis using 5 LVs.	83
Figure 5.1 Schematic diagram of the SIBS instrumentation [18].....	102
Figure 5.2 Schematic diagram of the first SIBS portable soil analyzer.....	105
Figure 5.3 Prototype of the portable SIBS soil instrumentation. A) External casing which houses the SIBS instrumentation. B) Side view of the hopper, screw-feeder and spark chamber, as well as the power supply.....	105
Figure 5.4 Sample spectra of iron oxide in clay from 0-10% iron. The Fe (I) 248.32 nm was used to create response curves of iron concentration vs. peak intensity. Spectral outliers were removed prior to averaging each data set.....	111
Figure 5.5 Response curve of Fe (248.32 nm) baseline corrected peak intensity; $R^2 = 0.89$	111
Figure 5.6 A comparison of organic, inorganic and elemental carbon at approximately 4.3% relative carbon. In each case, outliers from each sample were removed prior to averaging the spectral data.....	112
Figure 5.7 A comparison of response curves of the three forms of carbon in clay.	112
Figure 5.8 Sample spectrum of Fe in clay in the 363 nm region with Fe concentrations ranging from 0.8 to 10 %.....	115
Figure 5.9 Response curves of Fe baseline corrected peak intensity for Fe (I) lines; $R^2=0.97$ for each of the four curves.....	115
Figure 5.10 Raw (no outliers removed) averaged data of soil 4 in the 248 nm region. This graph illustrates the differences of signal intensity between the three mesh sizes.	118
Figure 5.11 A.) 200 mesh soil 4 B.) 100 mesh soil 4 C.) 20 mesh soil 4. A-C represents total cumulative data points, with no outliers removed. As the particle size increases, the carbon peak variability decreases. The carbon peaks are base-line corrected.....	119
Figure 5.12 Carbon peak variability of soil 4 20 mesh with outliers removed from the data set.	120

Figure 5.13 Total carbon of 9 soils compared to signal intensity.....	125
Figure 5.14 Total organic carbon of 9 soils.....	125
Figure 5.15 Total carbon of 8 soils, $R^2=0.94$	127
Figure 5.16 Total organic carbon of 8 soils, $R^2= 0.97$	127
Figure 5.17 SIBS spectrum of soil 4 from 245 to 256 nm. Principal emission features in this region are C I (247.86 nm), Fe I (248 to 249 nm) and Si I (250 to 253 nm). These lines were used to evaluate the prediction models [18]......	129
Figure 5.18 Loadings plot from the first latent variable (LV1) from SIBS, capturing 50.14% of the variance. A comparison is made between the LV1 regression coefficient and the spectral data in the 248 nm region. The most weighted wavelength in the spectrum corresponds to the neutral C line at 247.86 nm [18]......	131
Figure 5.19 Plot of calibration error (RMSEC) and cross-validation error (RMSECV) as a function of the number of latent variables retained in the PLS model for carbon. The data set included a summation of 10 shots with 10 data points per soil sample [18]......	134
Figure 5.20 Plot of measured vs. predicted total carbon from 8 samples using SIBS. Use of Carbon only with 3 LVs, with a summation of 10 shots and 10 data points per soil sample [18]......	134
Figure 5.21 SIBS spectrum of soil 4 from 245 to 256 nm. Principal emission features in this region are C (I), Fe (I) and Si (I)......	137
Figure 5.22 SIBS spectrum of soil 4 from 350 to 370 nm. The principal emission feature in this region is the CN (B-X) in the 358 to 359 nm region. The region of 352 to 366 nm was used to evaluate the prediction models.....	140
Figure 6.1 Drawing of spark gap and lens tube section interfaced to an aerosol generator that produces the sample described in the text. Air is pumped through the porous cylinder that forms the generator and dries and delivers the particles produced by the nebulizer to the spark gap [17]......	148
Figure 6.2 Photographs of the SIBS design. A). Close-up of the electrodes and the optical translation. B). Photograph the collection optics. C). The $\frac{1}{4}$ m monochromator coupled with the ICCD detector.	151
Figure 6.3 Time profile of calcium II (393.36 nm) focused at hot electrode.	155
Figure 6.4 Time profile of calcium II (393.36 nm) focused at ground electrode.	155

Figure 6.5 Bt 81 mg/100mL from 365-405 nm. Focused on hot electrode, and the Ca line at 393.36 nm is highlighted.....	156
Figure 6.6 Elemental analysis of <i>Bacillus thuringiensis</i> (Bt), ragweed pollen, and Johnson grass smut. Major elements were measured with a Perkin-Elmer CHN analyzer by Elemental Analysis Inc., Lexington, Kentucky, USA [17].....	158
Figure 6.7 Elemental analysis of <i>Bacillus thuringiensis</i> (Bt), ragweed pollen, and Johnson grass smut. Minor elements were measured with proton-induced x-ray emission (PIXE) by Elemental Analysis Inc., Lexington, Kentucky, USA [17].....	158
Figure 6.8 SIBS spectra of <i>Bacillus thuringiensis</i> (Bt), ragweed pollen (RW), and Johnson grass smut (smut) from 350 to 390nm. Principal emission features in this region are Ca (370.60 and 373.69 nm), CN (B to X, 387.1 and 388.2 nm), N ₂ ⁺ (between 350 and 360 nm) and Si (390.55 nm) [17].....	162
Figure 6.9 SIBS spectra of <i>Bacillus thuringiensis</i> (Bt), ragweed pollen (RW), and Johnson grass smut (smut) from 285 to 320nm. Principal emission features in this region are Ca (315.89, 317.93, and 318.13 nm) and Si (299.5 nm). The bright feature at 288.8 nm is an electrode line [17].....	162
Figure 6.10 Background corrected CN temporal profile at 388.2nm (0 to 0 vibrational band) for Bt, RW, Johnson grass smut smut, and air with matched relative humidity as a background [17].....	165
Figure 6.11 Modeled molecular spectra convolved with electrode lines. This synthetic spectrum models the same spectral region seen in Figure 6.8. Molecular features (CN and N ₂ ⁺) were modeled at 6000 K [17].....	165
Figure 6.12 Background corrected Ca II temporal profiles (373.69 nm) for Bt, RW, and smut [17].	167
Figure 6.13 Plot of integrated background corrected peak height of CN (387.1nm) feature versus % N by weight as analyzed by combustion in the laboratory. R ² of line drawn through these data is 0.934 [17].	170
Figure 6.14 Plot of integrated background corrected peak height of Ca II (373.69 nm) versus % Ca by weight as analyzed by PIXE. R ² of a line through these data is 0.995 [17].	170
Figure 7.1 A schematic diagram of the early experimental LIBS setup for analyzing oolitic hematite sample under a CO ₂ atmosphere. A digital camera mounted on a stand was used to collect plasma images.....	179

Figure 7.2 A schematic diagram of the LIBS setup for analyzing hematite sample under a CO ₂ and Martian atmosphere. Each cylinder was attached to a valve and flowmeter. A mixing valve was in place prior to the glass chamber in order to allow proper gas ratios into the chamber.....	184
Figure 7.3 Sample spectra under a CO ₂ atmosphere at a variety of pressures from 360 nm to 400 nm with a 500 ns delay. Key elemental features are labeled, and the majority of the lines in this region consist of Fe.....	187
Figure 7.4 Four sample spectra under a CO ₂ atmosphere in the 390 nm to 398 nm region. This narrow region illustrates the change in linewidth and intensity with an increase in pressure.	187
Figure 7.5 A comparison of the Ca (II) 396.85 nm baseline corrected line intensity of hematite under a CO ₂ atmosphere. The intensity of the Ca line begins decreasing around 30 T.	188
Figure 7.6 Ca (II) 396.85 nm linewidth comparisons of three different gate width delay times. As the pressure increases, the linewidth increases nonlinearly.....	190
Figure 7.7 Plasma area (pixels) compared to pressure (T) under a CO ₂ atmosphere.	192
Figure 7.8 Sample spectra of five different pressures under a Mars-like atmosphere with a gate delay of 1.5 μs.	197
Figure 7.9 Sample spectra of five different pressures with a 1.5 μs delay under a Mars-like atmosphere. These close-up spectra illustrate the change in line width with a change in pressure.	197
Figure 7.10 Comparison of an Al I line under two different atmospheres at a gate delay of 1.5 μs from 0.1 to 10 T.	198
Figure 7.11 Comparison of a Ca II line under two different atmospheres at a gate delay of 1.5 μs from 0.1 to 10 T.	198
Figure 7.12 Comparison of a Fe I line under two different atmospheres at a gate delay of 1.5 μs from 0.1 to 10 T.	199
Figure 7.13 Signal intensity of the Ca (II) 396.85 nm line compared to the pressure...	200

Figure 7.14 A-D (left to right), Output of plasma formation: A.) Laser flashlamp illuminating hematite sample just prior to laser pulse. B). During laser pulse, creation of plasma. This used to determine plasma size. C and D. Post laser pulse, the degradation of the plasma. These pictures were collected under Mars-simulated atmosphere at 5.1 T with 500 μ s, 700 μ s, 800 μ s, 900 μ s; frames and time from beginning of picture collection.....	202
Figure 7.15 Plasma area compared to pressure of the two different atmospheres.....	202
Figure 8.1 Diagram of the sheath flow design.....	211

List of Tables

Table 4.1 Soil location, description and rating of 8 soil samples. *Information obtained from the USDA Web Soil Survey [99].	67
Table 4.2 Total carbon and nitrogen values for 8 soils. Standard deviations reported were determined by three trials for each sample. *Indicates samples that were not further used in analysis due to high standard deviation. ** Indicates standard deviation values were not available.	67
Table 4.3 A summary table of the different regressions that were used to evaluate the data.	83
Table 5.1 Soil location and description of 9 soil samples. * Information obtained from the USDA Web Soil Survey [99]. ** Denotes sample that was not used in regression analysis.	89
Table 5.2 Percent of TC determined by CHN analysis. Percent IC and OC determined by difference. Elemental results of Fe and Si determined through HF digest followed by ICP-OES. ** Denotes sample that was not used in regression analysis.	92
Table 5.3 Composition and relative percentages of the major components found in KGa-1b.	94
Table 5.4 Table of organic carbon in the form of KHP added to KGa-1b in the range of 0-10.8 % C.	96
Table 5.5 Table of inorganic carbon in the form of K_2CO_3 added to KGa-1b in the range of 0-8.69 % C.	96
Table 5.6 Table of elemental carbon in the form of coal added to KGa-1b in the range of 0-9.46 % C.	96
Table 5.7 Iron in the form of iron oxide (Fe_2O_3) added to KGA-1b in the range of 0-10.04 % Fe.	97
Table 5.8 A comparison of the average carbon signal results of three soils with three different mesh sizes. Raw averaged data was used to determine average peak intensity, standard deviation and relative standard deviation. As the particle size increases in each sample, the relative standard deviation decreases.	123

Table 5.9 A comparison of the three soils of a 20 mesh particle size. Prior to averaging, all outliers were removed from the data set using PCA with a commercial software package (PLS Toolbox, Eigenvector). By removing outliers, the RSD is further decreased within each data set.	123
Table 5.10 Summary table of regression model which includes elements in the model, C prediction error, RMSECV when using 2 and 3 LVs. The RMSECV is reported as percent (%). Data includes the summation of 10 shots and 10 data points per soil sample [18].	131
Table 5.11 A comparison of the two different SIBS instrumentation and the prediction.	137
Table 5.12 Peak wavelengths of the molecular bands of the CN emission lines found in the UV spectral region. The (1-0), (2-1) and (3-2) vibrational bands were used to evaluate the prediction models [122].	140
Table 5.13 Prediction results using 3LVs of TC, OC and IC. IC was determined by the difference between the prediction of TC and OC.	141
Table 5.14 TC and OC RMSEC and RMSECV values for both 3 and 4LVs. The R ² values are also listed. The error is associated with each PLS model.	141
Table 6.1 Principal lines observed in the SIBS analysis of bioaerosols [17].	160
Table 7.1 Elemental composition determined by XRF of the hematite used during data analysis.	179
Table 7.2 Widths of emission lines in the 360 nm to 400 nm range under various conditions. Error was determined from the line fits.	199
Table 7.3 Intensities of emission lines in the 360 nm to 400 nm range in Earth, Mars and CO ₂ atmospheres. Error determined from the number of repetitions.	200

Table of Abbreviations Used in This Dissertation

AES	ATOMIC EMISSION SPECTROSCOPY
BT	BACILLUS THURINGIENSIS
BWAS	BIOLOGICAL WARFARE AGENTS
CCD	CHARGED COUPLED DEVICE
CHN	CARBON HYDROGEN NITROGEN
CPP	COMBINED PULSE PLASMA
CE	CORONAL EQUILIBRIUM
CEM	CONTINUOUS EMISSION MONITORING
CLS	CLASSICAL LEAST SQUARES
CRSS	COLLISIONAL RADIATIVE STEADY STATE
EPA	ENVIRONMENTAL PROTECTION AGENCY
EPIC	PRODUCTIVITY IMPACT CALCULATOR
DOE	DEPARTMENT OF ENERGY
FWHM	FULL WIDTH HALF MAXIMUM
GUI	GRAPHICAL USER INTERFACE
GXR	GEOCHEMICAL EXPLORATION REFERENCE
HEPA	HIGH-EFFICIENCY PARTICULATE AIR
HFHM	HALF WIDTH HALF MAXIMUM
HZ	HERTZ
ICP-OES	INDUCTIVELY COUPLED PLASMA OPTICAL EMISSION SPECTROMETRY
IC	INORGANIC CARBON
ICCD	INTENSIFIED CHARGED COUPLE DEVICE
J	JOULE
K	KELVIN
KV	KILOVOLT
LV	LATENT VARIABLE
LIBS	LASER-INDUCED BREAKDOWN SPECTROSCOPY
LOD	LIMIT OF DETECTION
LOQ	LIMIT OF QUANTITATION
LTE	LOCAL THERMODYNAMIC EQUILIBRIUM
MCP	MICROCHANNEL PLATE
MLR	MULTIPLE LINEAR REGRESSION
MS	MILLISECOND
μ S	MICROSECOND
NG	NANOGRAM
NM	NANOMETER
NIST	NATIONAL INSTITUTE OF STANDARDS AND TECHNOLOGY
OC	ORGANIC CARBON
OLS	ORDINARY LEAST SQUARES
OSHA	OCCUPATIONAL SAFETY AND HEALTH ADMINISTRATION
PC	PRINCIPAL COMPONENTS

PPBW	PARTS PER BILLION BY WEIGHT
PCA	PRINCIPAL COMPONENT ANALYSIS
PIXE	PROTON-INDUCED X-RAY EMISSION
PLS	PARTIAL LEAST SQUARES REGRESSION
PSI	PHYSICAL SCIENCES, INC.
RSD	RELATIVE STANDARD DEVIATION
RM	REFERENCE METHODS
RMSEC	ROOT MEAN SQUARE ERROR OF CALIBRATION
RMSECV	ROOT MEAN SQUARE ERROR OF CROSS-VALIDATION
RW	RAGWEED
SIBS	SPARK-INDUCED BREAKDOWN SPECTROSCOPY
SMUT	JOHNSON GRASS SMUT
S/N	SIGNAL TO NOISE RATIO
SNV	STANDARD NORMAL VARIABLE SCALING
SOC	SOIL ORGANIC CARBON
STD	STANDARD DEVIATION
TC	TOTAL CARBON
USDA	UNITED STATES DEPARTMENT OF AGRICULTURE
USGS	UNITED STATES GEOLOGICAL SURVEY
WSS	WEB SOIL SURVEY

Chapter 1 : Introduction

Over the years, the use of analytical methods to identify and quantify elemental constituents within a sample has become critical in order to meet the needs of chemical analysis of solids, liquids, and aerosols. One large group of analytical methods, known as spectrometric methods, is based on molecular and atomic spectroscopy. Spectroscopy is a general term for the science that deals with radiation-matter interactions. Historically, radiation-matter interactions of interest consisted of electromagnetic radiation and matter [1]. The majority of spectrometric methods are based on electromagnetic radiation in the form of light and radiant heat. Gamma rays, X-rays, ultraviolet, microwave and radio-frequency are also forms of electromagnetic radiation [1]. However, scientific advances in spectrometric methods have broadened the field to include interactions between matter and other forms of energy. These other forms of energy include acoustic waves and particle beams made of ions and electrons.

Spectroscopy can be used to determine the identity, structure and the environment of atoms and molecules by analysis of the radiation emitted or absorbed by them [2]. The light from a gaseous discharge, when analyzed by wavelength to form a spectrum, is found to consist of discrete line or band features. Each line or band is characteristic of some property of a particular atom or molecule, and once the characteristic line pattern of an atom is known, its appearance in the spectrum establishes the presence of sample atom in the source. This aspect of spectroscopy is known as spectrochemical analysis [2].

Spectrochemical analysis has become a powerful instrumental technique for the determination of the chemical elements. This technique provides the ability to analyze a variety of sample types and sizes, concentrations levels and at vastly different cost and time consumption. Spectrochemical analysis also provides the possibility to determine monoelement and multielement species in a single sample with a broad range of accuracy and precision using various techniques [3]. In order for advancements in spectrochemical analysis to be made, an understanding of the basic principles of atomic and molecular spectroscopy as well as spectrochemical analysis must be known. Research in this discipline will enable innovative developments of new techniques to be achieved to continuously improve the power of detection, increased accuracy and at relevant costs.

One advancement of spectrochemical analysis for elemental analysis was laser-induced breakdown spectroscopy (LIBS). The use of the acronym LIBS was first used by D. A. Cremers and L. J. Radziemski at Los Alamos National Laboratory (Los Alamos, NM) in 1983 [4]. This method was developed approximately 20 years after the first lasers (acronym for light amplification by stimulated emission of radiation) were developed around 1963. LIBS is a technique in which spectra of laser-produced plasmas are used for qualitative and quantitative spectrochemical analysis of condensed and gaseous samples with minimal sample preparation [4]. Since the development of LIBS, several advances have produced more reliable lasers, detectors and miniature spectrographs with the capabilities to monitor spectra over a wide range of wavelengths [4]. Thus, LIBS has become an analytical method with the potential of detecting a wide range of chemical elements in a sample with minimal preparation, real-time responses, and of close-contact or stand-off analysis of targets [4, 5].

A more recent technique known as spark-induced breakdown spectroscopy (SIBS) was developed in the late 1990's at Physical Sciences, Inc. (Andover, MA). Like traditional spark spectroscopy, the plasma is formed electrically. However, traditional spark spectroscopy is generally performed upon conductive samples (metals) and is predominantly used in alloy analysis [6]. SIBS, on the other hand, does not require a conductive sample. SIBS is similar to LIBS, except that it uses an electrical spark to create the plasma and to analyze elements of interest instead of a focused laser beam. SIBS has been applied to a wide range of analyses, including heavy metals in airborne particulates, bioaerosols and soils. However, SIBS is a relatively new technique, and additional research is still needed in order to determine its detection limits, accuracy and precision and cost performance on a variety of sample matrices.

Both SIBS and LIBS have proven to be useful tools for rapid analytical techniques for both environmental and biological applications. For example, there is an increased need to monitor gas and particle emission originating from exhaust stacks for regulation enforcement purposes [7]. Several heavy metals, such as copper, lead, and chromium have been identified as particulate pollutants. An on-line measurement system is ideal for the detection and monitoring of toxic metals, and therefore, the use of LIBS and SIBS has the potential to be applied to continuous air monitoring [7-9]. In addition, both SIBS and LIBS can be used to monitor hazardous biological aerosols. Bioaerosols include pollen, fungi, bacteria and viruses, and they are found nearly everywhere. In some cases, their concentrations may not be high, but they can still cause allergic reactions or diseases when inhaled [4, 10, 11]. Furthermore, LIBS and SIBS have been used to study both metal contaminants in soils as well as carbon in soils [12-15].

1.2 Development of SIBS and Literature Review

The following sections will present the early research and development of SIBS as it applies to air and soil monitoring.

1.2.1 SIBS Emission Measurements of Air

SIBS was developed and tested by Hunter *et al.* as a new real-time monitoring technique for heavy metal aerosols and particles in air [16]. The technique is based on temporally resolved atomic emission resulting from plasma excitation of aerosolized heavy metal samples. In general, SIBS requires a method of spark formation, some type of optical detection, a sampling scheme and a pump to allow the sample to travel through the spark gap. The spark formation is generated electrically with a power supply (<2000 V, 100 J/s) integrated with a capacitor bank [16]. After the capacitors are charged, a trigger pulse initiated the creation of an ion channel between the electrodes through a high-voltage (40 kV), low-current pulse provided by an automotive ignition coil [16]. This channel provided a low resistance path for the discharge of the capacitor bank. This first generation power supply had a total discharge energy range of 1 to 5 J. In addition, the spark frequency had a range of 1 to 10 Hz, but was usually operated at 1 Hz. The power supply was connected to two rod-shaped electrodes with a 4-6 mm gap, which facilitates the formation of for the spark. This spark gap was placed at the centerline of the sampled gas flow [16]. The electrodes are composed of a proprietary material chosen for high corrosion resistance, high melting temperature and low ablation propensity [16]. Additionally, the electrode material does not produce any spectral interference in the wavelength regions of interest (200 nm to 400 nm) even though there are several

electrode lines found in this region. After excitation, optical detection is delayed to minimize interference from broadband plasma Bremsstrahlung (recombination) radiation. When the plasma has cooled, atomic and molecular emissions are quantitatively measured using a gated intensified charged coupled device (ICCD) interfaced with a spectrometer. Using this type of detector, wide spectral regions can be recorded with sub-nanometer resolution in a single spark [17]. The concentration of species of interest in the sample is deduced from the intensity of the emission by comparison to a calibration curve. Since the development of SIBS, it has been used as an analytical method on a variety of applications [8, 12, 16-18].

The first application of SIBS was for the continuous emission monitoring (CEM) of hazardous air pollutant metals [8]. In 1997, the Environmental Protection Agency (EPA) and Department of Energy (DOE) collaborated on a joint study to test various prototypes and commercially available CEM technologies at the EPA laboratory in Research Triangle Park, NC. SIBS was one of seven CEMs tested side by side in a duct following a rotary kiln incinerator simulator. Two different concentrations, 15 and 75 $\mu\text{g}/\text{dry standard cubic meter}$, of six metals were introduced into the incinerator. These metals included beryllium (Be), arsenic (As), chromium (Cr), cadmium (Cd), lead (Pb) and mercury (Hg).

Figure 1.1 is a schematic diagram of the test configuration, which allowed for all seven CEMs to collect data simultaneously. Prior to running the experiments at the EPA test center, the instrument was calibrated in the laboratory for Cr and Pb. The laboratory calibrations for both Cr and Pb demonstrated detection limits of 9 parts per billion by weight (ppbw), which corresponds to $\sim 10 \mu\text{g}/\text{acm}$ (actual cubic meter). The calibration

curves were linear up to the maximum concentration tested of 1 part per million by weight (1 ppmw) [8]. This information provided calibrations for the real-time determinations of the concentrations in the gas stream at the EPA test center. In addition to SIBS data, reference methods (RM) were performed simultaneously along with each CEM method. The SIBS data was then compared to the reference method results.

Data were collected and analyzed for Cr and Pb, the only metals from the provided analytes targeted for testing. The average Cr results for this experiment determined by the SIBS analyzer were $96 \pm 13.2 \mu\text{g}/\text{m}^3$, and the average Pb results were $22.7 \pm 4.3 \mu\text{g}/\text{m}^3$. The measured Cr average concentration by the SIBS analyzer was $38.6 \pm 15.6 \mu\text{g}/\text{m}^3$, and that for Pb was $5.2 \pm 4.2 \mu\text{g}/\text{m}^3$. However, the data did show discrepancies when compared to the RM. The RM data exhibited a high degree of variability from run-to-run and from station-to-station within a run. The run-to-run variability was explained by poor reproducibility of the metals into the incinerator system. The station-to-station variability was thought to be due from systematic difference between the stations. Due to these variabilities, it was hard to compare the results from the different CEM s, and only averages over the entire test were compared. Comparison of the SIBS averages against the RM averages indicated that the measured SIBS Cr values typically exceeded the RM Cr values by a factor of 2. The measured SIBS Pb averages were about a factor of three below the RM values.

Although there were discrepancies between the SIBS and RM values, this experiment provided data for the first field test of SIBS. More importantly, these data provided the ground works for future SIBS experimentation and design modifications. Even though these results were outside the relative accuracy goal of 20%, the results

indicated that SIBS can be used as a new analytical tool to measure toxic heavy metals in air through continuous emission.

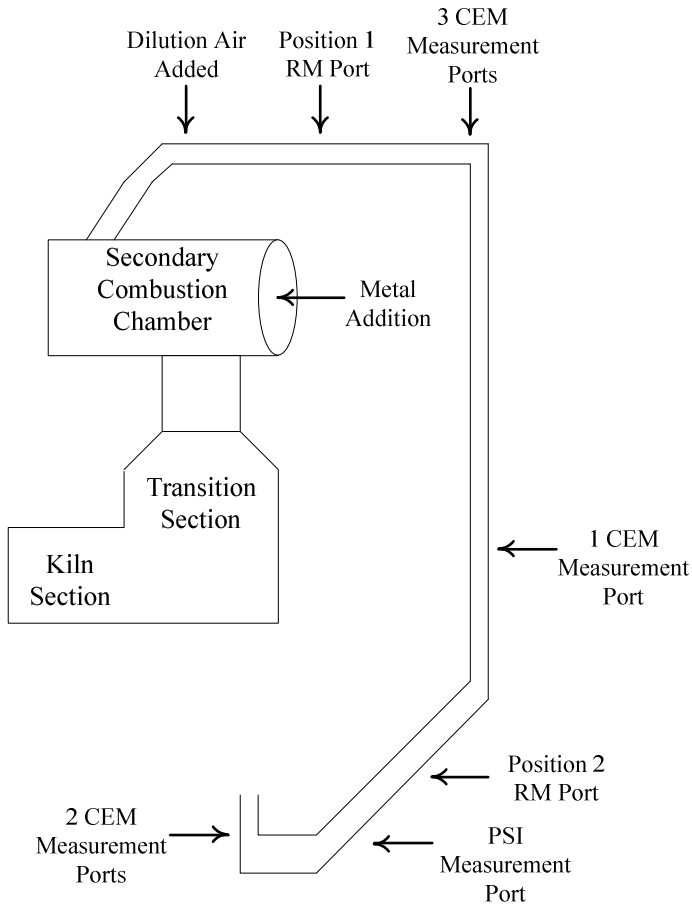


Figure 1.1 Schematic diagram of the incinerator simulator test configuration adapted from Hunter *et al.*, 2000 [8].

Another important SIBS experiment involved monitoring air above a Cr plating tank [19]. This monitoring event took place at the Marine Corps Logistics Base in Albany, Ga. The SIBS monitor acquired real-time data and was used to survey the total Cr concentrations above the plating bath surface over a range of ventilation rates in conjunction with operation of an experimental liquid recirculation system. This system was developed by the U.S. Army Construction Engineering Research Laboratories, in order to see if a newly designed liquid flow system had the potential to reduce chromium exposure by reducing the exhaust ventilation rate. The concentrations of Cr measured ranged from $<10 \mu\text{g}/\text{m}^3$ (the lower detection limit) to $>1000 \mu\text{g}/\text{m}^3$. SIBS data were correlated with the ventilation rate as well as the total mass of Cr collected on the internal filters. Seven filter samples were sent to an independent laboratory for total Cr mass analysis, and compared to the SIBS monitor data by integrating the measured concentrations. Two of the seven filters contained high Cr concentrations and were excluded from the correlation between SIBS spectral data and measured Cr mass. For the five valid points, the correlation was good, and had an R^2 value of 0.995. In addition, four of the five SIBS measured points were within $\pm 20\%$ of the filter measurements. Even though the sample set for this study was small, it still provided proof-of-principle data that SIBS can be used to measure Cr of airborne particulate.

A third fundamental SIBS study involved the development of a Pb monitor for deployment in an indoor firing range [16]. The indoor firing range introduced clean air behind the shooting booths. During shooting, the air flow picks up Pb and carries it away from the shooters downrange by a ventilation system. The Pb particles were then collected on high-efficiency particulate air (HEPA) filters. Prior to testing, the SIBS

instrument was calibrated for Pb and Cr aerosols in the laboratory over the 0 to 10000 $\mu\text{g}/\text{m}^3$ range.

The first test of the firing range was placed in front of active firing booths. The results indicated that the measured lead concentration was near the detection limit of 10 $\mu\text{g}/\text{m}^3$, which is well below the Occupation Safety and Health Administration (OSHA) regulated level of 50 $\mu\text{g}/\text{m}^3$. In addition, lead-free ammunition was fired directly above the sample inlet at two sampling locations, and no significant lead reading was obtained. A second test was done at the same range in which the SIBS monitor was placed down range just before the HEPA filters. When active firing took place lead concentrations as high as 3000 $\mu\text{g}/\text{m}^3$ were detected in the ventilation room. This high concentration value was considered reasonable due to the sample location, and this range is reached only in the ventilation room. The results from these SIBS monitoring experiment illustrated that Pb can be detected at concentrations of 10 $\mu\text{g}/\text{m}^3$, in-situ and in real-time.

1.2.2 SIBS to Monitor Metals in Soils

Although SIBS was first developed to monitor air for heavy metals, it was later adapted to screen soil for certain heavy metals [12]. In this study, the spark chamber was modified so that the sparks were made on the surface of the soil by a pair of electrodes. These electrodes were angled toward the surface near the soil, and as the sparks occurred, some of the soil was incorporated into the plasma. The spark chamber was connected to a power supply, function generator, miniature spectrometer and a laptop personal computer. The power supply used in this experiment has been previously described in section 1.2.1, and the function generator was used to create acquisition delay.

In the preliminary research, standard additions of aqueous solutions of Pb, Cr, Ba, Hg and Cd metals were used to make spiked subsamples of soil. These samples were dried and analyzed. Each soil subsample was analyzed by taking averages of 20 successive sparks generated at the soil surface. Between each sample, the electrodes were cleaned with nitric acid, deionized water and methanol to prevent carry-over. Once the spectral data were obtained, the signal intensities for the metals were baseline corrected and normalized to a nearby Fe line. The concentration of Fe is characteristic of the sample matrix. The intensity of this line should not change with the amount of metal contaminant added to the aliquot during standard addition. This is due to the fact that the soil samples are not being diluted with the addition of the metals of interest. Instead, the Fe feature only varies with the changes in the quantity of spark-processed material and with the individual strength of the spark. By ratioing the contaminant to the Fe line, the calibration curve was a signal-level ratio verses contaminant concentration [12]. The results of this study indicated detection limits for all investigated metals to be ~25 mg/kg. This study was demonstrated that SIBS can be used to identify and quantitate a variety of contaminant metals in soil.

1.3 Comparison of SIBS and LIBS

SIBS is similar to LIBS in that a plasma is used to excite atomic species of analyte atoms within the sample. As previously noted, SIBS uses a pulsed plasma generated with an electric spark to excite the sample of interest. The spark creates air plasmas at temperatures in excess of 10,000 K, and occurs between two rod-shaped electrodes. Material initially within the plasma volume is vaporized and all molecular

species are atomized. The high plasma temperatures excite atoms in the volume to high-energy electronic states. The subsequent emission from these states provides the signal to be monitored [12, 16, 20].

LIBS has been under development since the mid-1960's, and has been promoted as a way to obtain elemental composition on a variety of samples with minimal or no sample preparation. The LIBS technique is based on direct ablation of sample material using a high power density ($> 1 \text{ GWcm}^{-2}$) laser. The laser focused tightly onto the sample surface leads to the formation of a plasma. The light emitted by the plasma is collected into a spectrometer and resolved both spectrally and temporally in order to obtain the analytical information about the elemental composition of the sample [20]. Identification of the spectral lines and measurement of their intensities provides qualitative and quantitative information, respectively.

1.4 Need and Research Objectives

The goals of the research described in this dissertation were to evaluate two different plasma spectroscopic techniques in both biological and environmental matrices. Specifically, SIBS and LIBS were used as analytical tools to characterize carbon in soil, biological aerosols and plasma characterization of hematite formations under a Mars-like atmosphere.

1.4.1 Specific Research Goals

New and innovative approaches to the detection of carbon in soil are required to increase the understanding of the role of carbon as it relates to soil carbon sequestration.

As the global community begins to realize the imminent risks associated with climate change, simple and low cost methods to detect and mitigate greenhouse gas emissions are important. Specifically, there is a need for the development of a portable, robust, real-time, fieldable monitor for the detection of carbon in soils. Soil carbon sequestration and the mitigation of carbon dioxide (CO₂) has become an important research topic within the soil science community. Several agricultural practices promote soil carbon sequestration by including a reduction in tillage disturbance, intensification of cropping rotations, or the replacement of annual crops with perennial vegetation [21]. Determining changes in soil carbon (C) stocks is difficult due to the relatively small inter-annual changes in soil C stocks compared to the total carbon stored in soils [22]. Verification of C storage focuses on accurately measuring small changes in terrestrial carbon pools and being able to distinguish sequestration from natural variation in C concentrations [23, 24]. Because of the requirement to make measurements of small changes, reducing uncertainties associated with measurements of the soil carbon component of terrestrial carbon pools is critical. It requires the measurement of large numbers of soil samples, which may not be economically feasible using current measurement technology [25, 26]. Therefore, the development of sensitive, robust, and cost-effective instrumentation to monitor the carbon content of soils in order to improve estimates of terrestrial C inventories and fluxes is necessary. The overall goal of this research was to use SIBS to develop a fieldable soil carbon monitor to quantify and monitor carbon in soils. In addition, the SIBS soil carbon monitor has the ability to be portable, which will allow for an increased sample through-put and as a consequence, an increased data set of soil carbon concentrations.

The second goal of this research was to study the use of SIBS as a new analytical method for the comparison of biological warfare agents (BWAs) simulants through the use of atomic and molecular emission profiles. The possible release of biological warfare agents is a current concern among both military and civilian governmental entities. One dispersal method involves the release of hazardous biological samples in a respirable aerosol composed of particles with aerodynamic diameters of 1-2.5 μm . Therefore, the threat of bioterrorism has led to a need for the development of two types of systems involving aerosol detection. The first of these systems is envisioned as a coarse sensor to indicate a rapid change in the amount of airborne biological material. The output of this sensor will be used to trigger a second, more sensitive confirmatory sensor.

Confirmatory sensors are biological assays capable of establishing the identity of a biological organism, sometimes even the level of biological genus and species. Trigger instruments under development are normally based upon observation of fluorescence in individual airborne particles and have been paired with LIBS.

In addition to military and defense applications, there are ongoing needs within the health care community to monitor airborne biological species such as molds and pollen because bioaerosols are known to induce immunological and infectious responses in those exposed. The detection and classification of bioaerosols could also be helpful in preventing the spread of disease in hospitals and other areas of dense or health compromised populations. An alternative to relatively fragile biological aerosol detection methods such as LIBS is the use of SIBS to monitor air for hazardous biological material. SIBS instrumentation was modified to study various, non-hazardous

bioaerosols in hopes to distinguish between sample types such as pollen, smuts and bacteria.

The final goal of this work was to use LIBS to compare two different atmospheric conditions, CO₂ and a Mars-simulated atmosphere, under low pressures. In 2011, a LIBS instrument was built into the rover that was sent to the Martian surface, with the expectation that it can be used to perform geological classification [27, 28]. Mars has an atmosphere which is comprised of approximately 95.3% carbon dioxide, 2.7% nitrogen and 1.6% argon. The average atmospheric pressure on Mars is about 7 Torr, but varies from 1 to 9 Torr, depending upon altitude and meteorological conditions. The atmospheric pressure on Mars changes seasonally; winter temperatures are sufficiently cold that some of the carbon dioxide freezes out of the atmosphere and is deposited at the polar cap. This reduces the partial pressure of carbon dioxide in the atmosphere. During the summer, when the polar cap warms up again, the carbon dioxide sublimates into the atmosphere, increasing the atmospheric pressure [29]. Clearly, the harsh environment of Mars presents a challenge for scientists who hope to not only collect geological data using LIBS, but also accurately analyze and determine geological classifications of such formations. Therefore, in order to accurately classify and quantify various elements that comprise the geological formations found on Mars, data must be collected using precise, replicated conditions found on Mars.

1.4.2 Methods of Detection of Carbon in Soils with Ablation Techniques

Fieldable measurement methods of the carbon content in soils are critical to assessing the efficiency of the sequestration process, and various approaches have been

taken to develop such an instrument. One method currently under development for the measurement of carbon in soils is LIBS, and several studies have been documented [30]. Early research into the application of LIBS to measure total soil carbon was performed by Cremers *et al.* [31]. They found that carbon could be identified and quantified using LIBS and a univariate analysis using calibration curves of laboratory carbon values against LIBS carbon signals. Furthermore, they determined that when the neutral C (I) line (247.85 nm) was ratioed to the signal from silicon, the measurement precision increased. This was done as an attempt to minimize large shot-to-shot variability in the carbon signal. Overall they were able to estimate the LIBS detection limits, within the sets defined by their calibration curves, to be 300 mg C/kg. Martin *et al.* studied the use of LIBS for environmental monitoring of soil carbon and nitrogen [32, 33]. The goal of Martin's research was to quantify carbon in a variety of soils through the use of the C (I) line at 247.85 nm, and compare these results to standard carbon, hydrogen and nitrogen (CHN) analysis. Measurements of the concentration of carbon in fifteen soil samples with varying levels of carbon were obtained. The preliminary results indicated that LIBS can be used in the direct quantitation of soil carbon, and the authors reported a linear calibration curve with a good correlation coefficient ($R^2 = 0.962$). The authors also took the ratio of carbon to silicon to improve the reliability of data; this decreased the standard deviations, and improved the correlation in carbon measurements between CHN and LIBS. More recent studies by Martin *et al.* looked at the use of LIBS to analyze soils using two different wavelengths and three different excitation energies in order to provide a reliable estimate of total soil C [15]. They found that the wavelength and energy of the excitation laser are important parameters when LIBS is used to determine C

concentration in soil. Using LIBS spectra processed with both principal components analysis (PCA) and partial least squares regression (PLS), these researchers were able to generate a model that was independent of soil type. Using 38 samples of varying soil type, PLS models were developed that showed the highest quality data were collected using an excitation wavelength of 532 nm with a pulse energy of 45 mJ. This excitation combination resulted in the best correlation statistics between LIBS signals and combustion CHN measurements. Their correlation coefficient was reported to be 0.97 and the root mean square error of cross validation was determined to be 0.31, using 3 PCs. Belkov *et al.* compared two LIBS techniques for the measurement of total carbon in soils [34]. The first method was the combination of a single-pulse laser ablation with spark excitation of the plasma plume, known as combined-pulse plasma (CPP). Spark excitation was created using tungsten wire electrodes with a 3 mm gap set at a distance of 1.5 mm from the sample surface, and the results compared to those obtained with the use of a double-pulse laser system. Their results indicated nonlinear trends in the actual range of carbon signals with both methods. They also found that the line intensity amplification in the CPP over what was observed in the two-pulse experiment was due to the increase of plasma volume and duration of the plasma emission. One potential issue using the C (I) line at 247.85 nm is the underlying Fe (II) line at 247.857 nm and Fe (II) line at 247.987 nm. Glumac, Dong and Jarrell in 2010 studied the potential elemental interferences with this region [35]. They compared samples of graphite and Fe oxides and their spectral and temporal signatures. Proper time gating, along with high resolution, allowed linear correlation ($r^2 = 0.94$) between measured percent soil organic carbon (SOC) and the integrated LIBS counts under the C (I) line. While their study did

not examine highly Fe-rich soils, based on their findings, there is negligible Fe interference in soil samples less than 4% total Fe. Therefore, under proper conditions, correlation of C (I) between measured carbon and predicted carbon is obtainable even with Fe present.

Early applications of SIBS to monitor soil involved the production of sparks in or near the surface of the soil sample followed by acquisition and analysis of the resulting emission with an ICCD [12]. The surface approach had reproducibility problems which motivated the development of a power feed mechanism for sample introduction to the spark gap. This early work also involved the use of modest sample pre-processing and standard addition of known quantities of analytes to enable quantitative analysis of toxic metals in soil [12].

1.4.3 Methods of Detection of BWAs with Ablation Techniques

Both indoor and outdoor ambient aerosols contain particulate material having biological origins, which exist in a wide range of sizes. Non-agglomerated single airborne bacteria have aerodynamic diameters between 0.5 and 2 μm ; mold spores are between 2.5 and 35 μm [36]. Pollen sizes generally are reported to range between 5 and 50 μm [37]. Nonviable fragments of microorganisms are also commonly encountered in ambient air and have been identified in the submicron size range [38]. The larger particles have much lower residence times in air, because of their greater settling velocity, but exert a deleterious effect to human health, even though they are a small part of the overall biogenic aerosol background. The bioaerosol background has been estimated at approximately 1.9 biological particles/ cm^3 , with about 30% of the total

particles measured in this particular region having a biological origin [39]. Pollen and biological warfare agents have in common that very small concentrations of particles can exert a large effect on the health of human populations and also that any attempt to monitor them must take the large background into account.

In attempting to develop a spectroscopic method of determining the types of hazardous bioaerosols in air, several groups have been working to utilize the appearance of molecular features in LIBS to perform various types of bioaerosol analysis. Boyain-Goitia *et al.* performed a set of experiments using LIBS and Raman microscopy to analyze single pollen grains [10]. These techniques are used together to differentiate pollen particles from background materials and also to obtain some classification information for the pollen. Samuels *et al.* have used a deposition sampling technique to collect relatively large quantities of individual species of bacterial spores, molds, pollen, and proteins on porous silver substrates [11]. These substrates were submitted to LIBS analyses, and principal component analysis was applied to discriminate between the different biomaterials. Even larger sample quantities were used in Morel *et al.*, where pellets of individual species of stimulants for biological warfare agents were submitted to LIBS analysis [40]. These authors hypothesize that the CN bands that are ubiquitous in direct plasma analysis of biological samples arise from the recombination of carbon originating in the sample matrix and nitrogen from the atmosphere. They saw no additional CN in the emission spectrum of the sample when additional CN sources are added to the sample materials.

The ability to classify biological organisms with direct ablation plasma techniques depends on the ability to generate spectral fingerprints indicative of the differential

elemental content of the spores [41]. Biological aerosols contain several inorganic elements such as K, Na, Ca, Mg, and Si, as well as organic constituents such as C, N, O, and H [11, 42]. Therefore, signals associated with these elements can be used to potentially distinguish between species of spores and bacteria. Spectroscopic interrogation of the bioaerosols also yields molecular features such as CN (B-X), OH, CH (A-X), and N_2^+ . Therefore, SIBS was used to study bioaerosols by analyzing both atomic (Ca, Si, Fe, Al) and molecular (CN (B-X), OH, CH (A-X) and N_2^+) features found in various biological samples.

1.4.4 Use of LIBS to Study Plasma Properties under Low Pressure

LIBS is another technique for a wide variety of analytical applications such as soil analysis [15, 25, 34] and geomaterial classification [43], forensics [44, 45], and detection and classification of biological contaminants and aerosols [46, 47]. Recently, many researchers have studied potential challenges of using a LIBS analysis on the Martian surface. Dreyer *et al.* studied the use of LIBS combined with Raman spectroscopy under Mars atmosphere-simulated conditions [48]. They observed significant plasma dynamic changes and consequently a decrease in spectral intensity of ionic species between 5 and 7 Torr which could be explained as a decrease in plasma temperature and electron density below 5 Torr.

Buhler *et al.* compared the electrical breakdown in a Martian gas mixture versus pure CO_2 [49]. The results suggested that at low pressures, a clear difference in the breakdown potentials can be seen. Specifically, small concentrations of nitrogen, carbon monoxide, oxygen and argon greatly alter the Paschen curve (breakdown voltage versus

pressure) for pressures ranging between 1 and 10 mm Hg. However, these preliminary results showed strong polarity dependence when using symmetric electrodes. It has been argued when using symmetric electrodes, reversing the polarity should not alter the effect on the electrons, and should only change the direction the electrons move [50]. Manning *et al.* also studied electric discharge and Paschen curves under a Martian atmosphere using identical, spherical electrodes. Their results indicated that the CO₂ and Mars gas had comparable curves, suggesting that the addition of small amounts of N₂ and Ar does not considerably alter the discharge potential [50]. Clearly, there are some discrepancies between authors studying the effects of different atmospheric conditions on LIBS spectra. Many variables can affect LIBS signal such as, temperature, laser power, gating delay and width and sample surface conditions. However, further studies will improve the ability to optimize the use of LIBS in harsh environments such as Mars.

1.5 Study Design and Dissertation Format

In this work, three different studies were performed using both SIBS and LIBS. The first study utilized SIBS as a new method to detect and quantify carbon in soils. Within the framework of this study, a portable SIBS instrument was built by our collaborators at Physical Science, Inc., and several soil samples were analyzed in order to determine detection limits, linear range and quantitation limits. The second project explored the use of SIBS as an analytical method to study bioaerosols. The goal of this research was to try to classify three different bioaerosol samples as well as improve sampling methods based on preliminary research. Finally, the third study sought to examine the changes in plasma characteristics using LIBS under low pressure similar to

the Martian atmosphere. The goal of this study was to compare spectral line widths and intensities with apparent plasma size under low pressure using a pure CO₂ atmosphere with a Mars-simulated atmosphere, and therefore to demonstrate the importance of an appropriate atmosphere for calibration.

A brief review of atomic emission spectroscopy and plasma physics is provided in Chapters 2 and 3. Chapter 4 provides the preliminary details on the materials, methods, and specific instrumentation used to study carbon in soil. Additionally, Chapter 4 provides the results for the various studies performed to determine carbon in soil. Chapter 5 is a more detailed chapter on the miniaturization of SIBS, and the development of a fieldable soil carbon monitor. Chapter 6 provides experimental details and results for the detection of bioaerosols using SIBS, and the use of LIBS to compare spectral features under low pressure can be found in chapter 7. Conclusions and future work are provided in Chapter 8.

Chapter 2 : Review of Atomic Emission Spectroscopy

The purpose of this research is to use emission spectroscopy to study BWA simulants as well carbon in soils. In addition, this dissertation discusses the use of LIBS as an analytical method to study changes in plasma characteristics as well as atomic emission behavior under low pressures. SIBS and LIBS are similar in that both are atomic emission (AE) techniques that can be used to quantify the concentration of elements in samples. The following chapter describes the theory involved in atomic emission spectroscopy (AES). AE is a method used to determine the identity, structure and the electronic environment of atoms by analyzing the radiation emitted by them [4]. By identifying the wavelengths of atomic lines, one can determine the energy levels of an atom, which provides experimental basis for the theories of atomic structure. One can also determine various elements in a sample by observing characteristic lines emitted by a particular atom [4]. This chapter will discuss the generalized theory of AES. Chapter 3 will discuss the theory of plasma physics as it relates to AES, and the use of SIBS and LIBS as analytical tools.

2.1 The History of Atomic Spectroscopy

The origins of atomic spectroscopy date back to the work of Bunsen and Kirchhoff in the mid-19th century, and is one of the oldest instrumental techniques for elemental analysis [3, 51]. In general, the work by Bunsen and Kirchhoff in 1860

showed how the optical radiation emitted from flames is characteristic of the elements present in the flame gases or that which is introduced into the flame through various methods. For example, through this technique, one could see that the color yellow corresponded to Na, and red corresponded to Ca. Prior to their work, it had already been observed that there was a correlation between the concentration of elemental species present and the intensities of the element-specific features in the spectra. Based on this information, the basis for qualitative and quantitative analysis with AES was discovered [3]. In addition, the Bohr theory of hydrogen in 1913 established the first link between the spectra and structure of atoms. In the 1920's, theoretical developments in quantum mechanics helped to develop accurate, experimental measurements on the fine and hyperfine structure of spectral lines. In more recent years, computational modeling and other technological advances have helped confirm and correlate studies between theory and atomic spectroscopy. Due to these scientific discoveries, several atomic spectrometric methods using flames and plasmas as excitation sources have been developed and are typically evaluated by comparing their analytical figures of merit with those of other methods for elemental analysis.

The signal used in atomic spectroscopy can be understood from the theory of atomic structure itself. The availability of optical spectra was instrumental in the development of the theory of atomic structure and the discovery of a series of elements. In the mid-19th century, the study of the relationship between the wavelengths of the chemical elements helped to determine a relationship between the atomic structure and the optical line emission spectra of the elements [3]. The following sections briefly

describe the basic theory of atomic structure in order to understand the basis of atomic spectroscopy as it applies to SIBS and LIBS analysis.

2.2 An Introduction to Electronic Structure and Hydrogenic Atoms

Spectroscopy deals with radiative transitions between stationary states of an atom or molecule. The term stationary state means the probability density does not change with time, and is therefore independent of time. The stationary states correspond to a quantum state with a single definite energy, and are defined by a single quantum number (n) [52]. Atoms consist of a positively charged nucleus and a number of negatively charged electrons. In a neutral atom, the total negative charge of all the electrons is equal to the total positive charge of the nucleus. The predominant forces that hold atoms together are electrostatic, which consist of the attraction between each electron and the nucleus and repulsions among all the atomic electrons. The basic process in optical atomic spectrometry involves the outer electrons (valence) of the atomic species. For atoms or ions in the elemental state, the energy of any given state arises from the motion of electrons around the positively charged nucleus. These energy states are known as electronic states [1, 4]. The stationary states of the hydrogen atom are as shown in Figure 2.1, and the hydrogen energy level diagram is the simplest of diagrams. A single quantum number n , defines the stationary states. The numerical value of energy in units of cm^{-1} is known as the term value T , and transitions between two stationary states i and j can be shown on an energy diagram by vertical arrows. Figure 2.1 defines each level in the energy diagram by the quantum, for example. These arrows point up for absorption

of radiation and down for emission. The difference of the two term values: $\sigma_{ij} = T_i - T_j$ is the wavenumber of the transition [2].

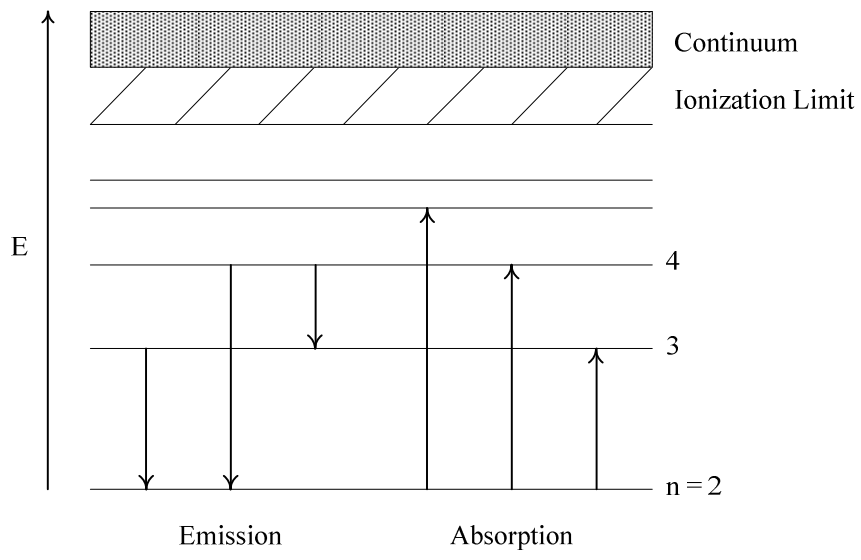


Figure 2.1 Energy level diagram of a hydrogen atom adapted from Singh and Thakur, 2007 [4].

The atomic wavefunction $\Psi_{n\ell m}$ is a function of the coordinates (x, y and z) of the electron's position in three-dimensional space. These coordinates are called quantum numbers, and result from the exact solution of the Schrödinger equation. The principal quantum number (n) is related to the size and energy of the orbital, whereas ℓ and m determine the angular momentum and orientation of the orbital in space relative to the other orbitals in the atom. For a given value of n , the value of ℓ for the wavefunction can be: 0, 1, and 2..., ($n-1$). In the same way, the values of quantum number m for a given ℓ are: $-\ell, (-\ell + 1), (-\ell + 2), \dots, 0, 1, 2, (\ell - 1), \ell$ [4].

The wavefunction $\Psi_{n\ell m}$ represents an atomic orbital, and any atomic orbitals belonging to a given value of n define a shell and those associated with a given value of ℓ represent a subshell [4]. Atomic orbitals corresponding to $\ell = 0, 1, 2, 3, 4 \dots$ are called s, p, d, f, g orbitals respectively. A fourth quantum number, s , was derived from the Schrödinger equation, and is called the spin quantum number. The spin quantum number is related to the magnetic moment of the electron and can only have two values, which include $+1/2$ and $-1/2$. Thus, the four quantum numbers describe the electronic configurations of atoms with many electrons.

The zero energy is defined for the electron and proton at rest at infinite separation, and therefore, is arbitrary. The energy corresponding to the principal quantum number n is $-\mathbf{R}_H/n^2$ where \mathbf{R}_H is the Rydberg constant for hydrogen [4]. The ground state energy of hydrogen atom is $-\mathbf{R}_H$ (109678 cm^{-1}) corresponding to $n = 1$. The lowest state of energy is $n = 1$, also known as the ground state. Lines in the spectrum of hydrogen are related to the Rydberg formula

$$\frac{1}{\lambda} = R \left(\frac{1}{n_1^2} - \frac{1}{n_2^2} \right) \quad \text{Equation 2.1}$$

The separation between consecutive energy states decreases as n increases, until it approaches the ionization limit. This corresponds to the complete removal of the electron, and the energy difference between i and j (the ground state and ionization limit), is the ionization energy of the atom [2, 4]. Once ionized, the states of positive energy correspond to the sum of the proton, electron and kinetic energies. This energy is no longer quantized, and there exists a continuum of states as seen in Figure 2.1. The transition of atom between a pair of discrete states is possible under certain conditions resulting in a spectral line. Transitions between the continuum and a discrete state are known as free- bound transitions (recombination radiation) and free-free transitions (Bremsstrahlung emission). Figure 2.2 refers to the typical transitions in an atom or ion. E_g refers to the ground state, E_1 and E_2 are excited state; the ionization limit is also noted.

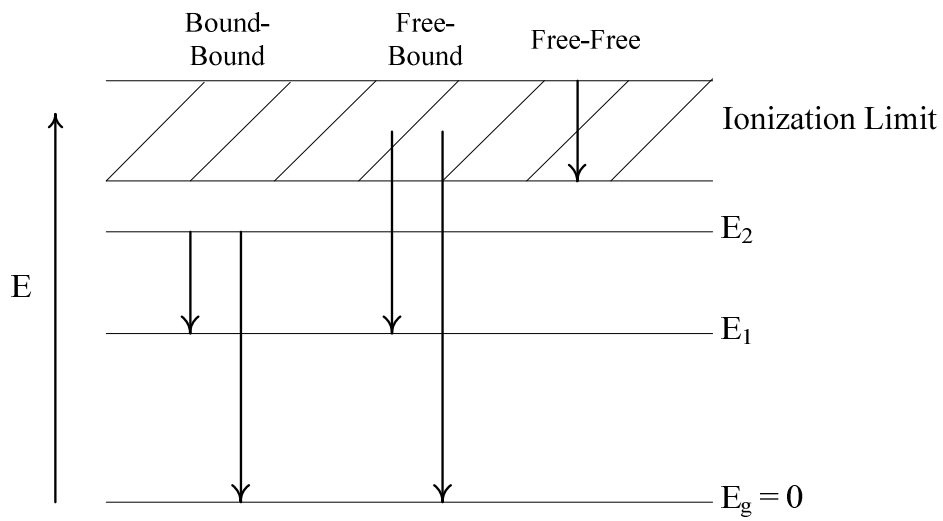


Figure 2.2 Typical transitions seen in an atom or ion which gives rise to optical emission. Adapted from Cremers, 2006 [5].

2.3 Multi-Electronic Atoms

The hydrogen diagram can also represent the energy of the electron or that of the atom as a whole. However, in a multiple-electron system, there are repulsions between each pair of electrons, and the hydrogenic orbitals do not account for this interaction. Due to the interactions between electrons, the resulting stationary states are characteristic of the whole atom instead of the excited electron. The resulting energy level diagram of a many-electron atom will be more complex than the hydrogen atom seen in Figure 2.1. The more readily excitable electrons are those found in the outer shell, and are loosely bound. However, it is possible to excite and remove a tightly bound electron or even two electrons at the same time. This would result in the atom would be in the ion state instead of the neutral (ground) state [2]. In addition to electronic states in the case of atomic emissions, molecules also have quantized vibrational states that are due to the energy of interatomic vibration, and quantized rotational states that arise from the rotation of molecules around their mass center. Thus, the total energy of the molecule (E) is not given exclusively by the electron energy (E_e), but by the vibrational energy (E_v) and the rotational energy (E_r) also contribute [53]. The total energy is given by the equation

$$E = E_e + E_v + E_r \quad \text{Equation 2.2}$$

During the excitation of the molecule, the vibrational and rotational energies also change along with the electronic energy. Therefore, the change in total energy is given by the equation

$$\Delta E = \Delta E_e + \Delta E_v + \Delta E_r \quad \text{Equation 2.3}$$

According to quantum theory, the electronic, vibrational and rotational energies are bound by quantum mechanics in addition to atomic energy states [53].

Energy levels of atoms or molecules and observed spectra can be used to infer information about the environment of the atom or molecule. The observed intensity of a line depends on the distribution of population among the various excited states as well as on the intrinsic transition probabilities.

2.4 Radiation of Atomic and Molecular Species

In 1900, the quantum theory was proposed by Max Planck in order to explain the properties of emission radiation of heated bodies [54, 55]. This theory was later extended to rationalize other types of emission and absorption processes. Two important postulates of quantum theory include:

- (1) Atoms, ions and molecules can exist only in certain discrete stable states, and that these allowed states possess specific, quantized, energies. When a species changes its state, it absorbs or emits an amount of energy that is equal to the energy differences between the states.

(2) The absorption or emission of these species produces radiation when making the transition from one energy state to another. The frequency (ν) or the wavelength (λ) of the radiation is related to the energy difference between the states by the equation

$$E_2 - E_1 = h\nu_{12} = hc/\lambda \quad \text{Equation 2.4}$$

where E_2 is the energy of the higher state and E_1 is the energy of the lower state. The terms c ($3.00 \times 10^8 \text{ m sec}^{-1}$) and h ($6.62 \times 10^{-34} \text{ J sec}$) are the speed of light and the Planck constant, respectively [1, 56, 57].

2.5 The Shapes of Emission Spectral Features

Radiation from an excited source can be characterized by means of an emission spectrum, which usually takes the form of a plot of the relative intensity of the emitted radiation as a function of wavelength or frequency. Two types of spectra can be seen in an emission plot, and include line and band emissions. The following two sections briefly discuss the characteristics of both line and band emission.

2.5.1 Line Spectra

The line spectrum is made up of a series of sharp, well-defined peaks caused by the excitation of individual atoms [1]. As previously discussed, the resonance equation 2.1 corresponds to the electronic transitions between two energy levels. Only absorption and emission spectra from atoms are considered sharp lines [56]. When dealing with

atoms, the sharpness of an atomic spectrum occurs because the energies (E_1 and E_2) of electronic states of atoms can be accurately described by specifying the electronic energies of the electronic orbitals. At low pressures in the gas phase for an atom there are no vibrations, rotations, or collisions that broaden the values of E_1 and E_2 . Therefore, $h\nu$ has a precisely defined magnitude since E_1 and E_2 are sharply defined. Thus, at low pressure in the gas phase, both atomic absorption and emission spectra show very sharp lines. For example, both the absorption and emission spectra of the gaseous H atom in the visible region of the spectrum consists of four lines at 410, 434, 486 and 656 nm, respectively. There is nearly an exact correspondence between positions of the absorption and emission, because the energy of orbitals involved in the ground and excited states in the transitions do not change significantly for an atom [56]. The promotion of an electron and emission of a photon for line spectrum occur on the order of 10^{-8} s. Figure 2.3 illustrates an energy level diagram of atomic emission (A), which indicate two Ca (II) emission lines at 315 nm and 373 nm. In addition, Figure 2.3 illustrates an energy level diagram of molecular emission, which is described in section 2.5.2. Figure 2.4 is an example that represents an atomic emission spectrum of C (I), Si (I) and Fe (I) found in soil in the spectral window of 245 nm to 260 nm. It is important to point out some spectroscopic terminology of ionic and neutral atoms. The spectrum of a neutral atom is designated I, while the spectrum of a singly ionized atom II, and a doubly ionized atom III. For example, Si (I) is the designation for a neutral atom while Mg (II) and Fe (II) are the designation of a singly ionized atom [2].

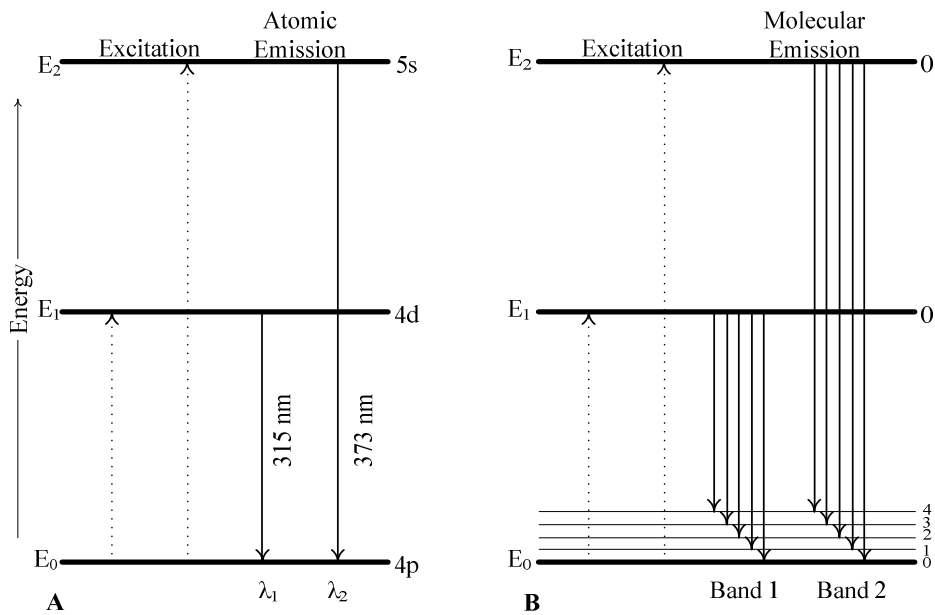


Figure 2.3 Energy level diagram of (A) atomic emission lines of Ca II atom, and (B) an example of a molecular emission profile. Adapted from Skoog, 2007 [1].

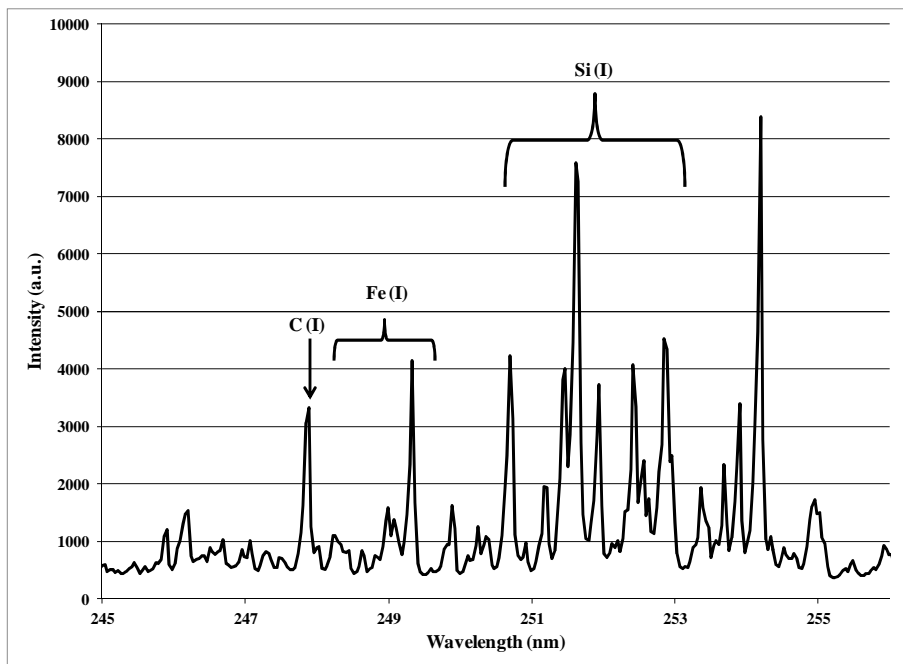


Figure 2.4 Sample spectrum of atomic emission lines including C (I), Si (I) and Fe (I).

2.5.2 Band Spectra and Diatomic Molecules

Although the majority of material discussed in this dissertation deals with atomic emissions, portions of the research include the study of molecular emissions such as CN ($B^2\Sigma^+ - X^2\Sigma^+$), OH ($A^2\Sigma^+ - X^2\Pi_i$) and N_2^+ ($B^2\Sigma_u^+ - X^2\Sigma_g^+$). Therefore, it is important to give a brief background on this. The term symbols used with CN, OH and N_2^+ are the values for distinguishing the electronic transitions of the molecular features. B, A, and X define the transitions between electronic states. By convention, the upper state is always written first. The term X describes the ground state, followed by A and B (in increasing energy). The terms Σ and Π define the vibrational and rotational perturbations corresponding to the specific energy level [58]. The superscripts ($^2\Sigma^+$ and $^2\Pi_i$, for example), refer to the singlet or doublet transitions, in which a superscript of 1 refers to the singlet transition and a 2 refers to the doublet transition [58]. Thus, this terminology illustrates which vibrational bands are observed in the spectral data. Figure 2.3 illustrates the difference between atomic and molecular emission, and a sample spectra of molecular emissions can be seen (B).

A potential energy curve of the observed states of the CN molecular feature can be seen in Figure 2.5. In addition to line spectra, molecules, even in the gas phase at low pressures, do not have pure electronic transitions. With small dispersion, these consist not of single, sharp lines as seen with atomic emission, but of less broad wavelength regions known as bands [58]. Band spectra are often encountered in spectral sources where gaseous radicals or small molecules are present, and arise from the numerous

quantized vibrational levels that are superimposed on the ground-state electronic energy level of a molecule [1].

Often in emission spectroscopy, bands and lines occur mixed together. In general, bands usually have a sharp edge at one end; this is called a *band head*. At the band head, the intensity falls sharply to zero, while on the other side the intensity gradually decreases. Unlike line spectra, molecular spectra have vibronic transitions that possess a range of energies. This is due to coupling between the electrons and vibrations. In order to describe the electronic states of a molecule, one must consider not only the motions of the electrons, but also the motions of nuclei relative to one another and the vibrations and rotations of the molecule as a whole. Thus, a molecular electronic transition between the energy states does not correspond to a well-defined single quantum of energy. As a result, the absorption and emission spectra of a molecule may involve many vibrational transitions over a range of energies. Instead of sharp lines, molecular absorption is replaced by a set of closely spaced lines. Usually these closely spaced lines cannot be resolved and are termed an absorption or emission band [56].

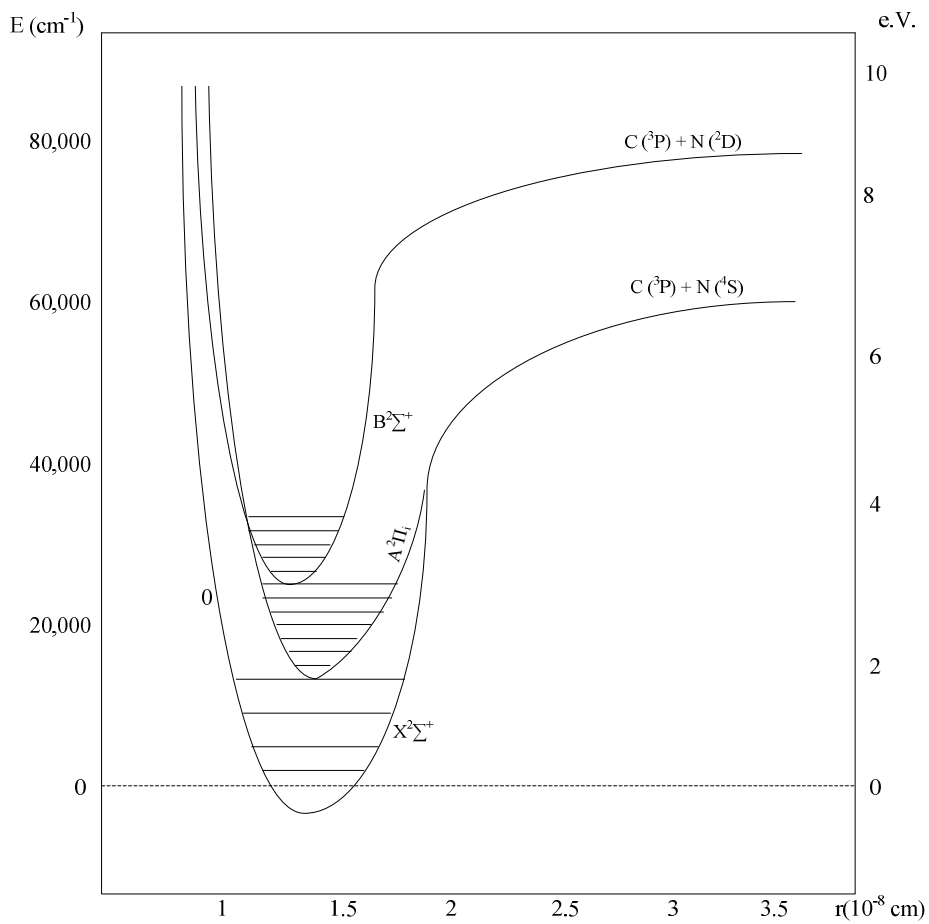


Figure 2.5 Potential energy curve of the observed electronic states of the CN molecule adapted from Herzberg, 1950 [58].

2.6 Spectral Intensities of Lines

The observed spectral intensities, which originate from radiative transitions, depend on two different factors. The first factor is the intrinsic probability, or transition probability, of the atom. This is also referred to as the line strength, and is known as the f -value [4]. The intensity of a spectral line depends on the atomic population of the initial level and also on the transition probability to the final level. Only transitions which are allowed will produce spectral lines, provided that the frequency of the oscillating field obeys the relation $h\nu = |E_2 - E_1|$. The transition probability refers to both absorption and emission, in which they are proportional to each other. The second factor is the interaction between the atom and the radiation source. In order for an electron to be excited, the electron temperature must be higher than the temperature defined by the kinetic energy of atoms or ions [4].

2.6.1 Continuum Emission

As noted early in this chapter, there exists a free-free, free-bound or bound-bound state of an electron-ion system in which the energy is positive. Continuum emission is when a transition between a free state and a stationary state (E_{ij}) of the atom occurs. The following equation gives rise to continuum emission whose frequencies are

$$h\nu = \xi - E_j + \frac{1}{2}mv^2 \quad \text{Equation 2.5}$$

where $\frac{1}{2}mv^2$ is the kinetic energy of the free electron and ξ is the ionization energy of the atom. Radiative recombination is another term for this emission process, and occurs when an ion captures an electron and makes a transition to the bound energy state E_j [4]. Continuum emission occurs shortly after, in the case of LIBS, the laser plasma formation. Similarly, continuum emission found in SIBS is expected near the time of the spark. The continuum is dominated by electron deceleration as they pass close to ions [59]. Since this emission occurs within the first few microseconds after plasma initiation, it can be eliminated from measurements. Chapter 3 will discuss in detail how continuum emission can be avoided and eliminated from measurements.

2.7 Spectral Line Broadening

Line widths are related to the electron density and temperature of the plasma. The environment of the atom and sample of interest impacts the intensities of spectral lines and molecular bands. In an ideal setting, the intensity of a line will have a frequency dependency described by a Lorentzian profile having the form

$$I(\nu) = I_0(\gamma/4\pi)^2/[(\nu - \nu_0) + (\gamma/4\pi)^2] \quad \text{Equation 2.6}$$

where I_0 the intensity at the center of the line profile ν_0 , and γ is the radiation damping constant [4]. The full width half maximum (FWHM) is the natural broadening $\left(\frac{\gamma}{2\pi}\right)$ of the spectral line. However, the ideal condition in which a spectral line solely contains

natural broadening only occurs under conditions with low atomic densities. In non-ideal conditions, natural broadening is accompanied by Doppler broadening which results in a Gaussian profile instead of a Lorentzian profile. Doppler broadening causes linewidths of atomic transitions, which is due to the random thermal movements of atoms [60].

Doppler and natural broadening can be neglected in most cases due to the fact that these broadening features contribute only a small portion of the overall line broadening seen in spectroscopy. However, the dominant line-broadening occurs between atoms and charged particles through electric fields, and is known as Stark broadening [4].

2.7.1 Stark Line Broadening

Collisions with ions and electrons result in the Stark effect, which produces Stark broadening. This broadening of emission lines is proportional to the electron density of the plasma; the higher the electron density, the greater the Stark broadening. The Stark effect also produces a shift of the emission line central wavelength, which can be used to determine the plasma electron density [61].

The broadening and shift of emission lines due to the Stark effect arises from the perturbation of emitting species by nearby charged particles [62]. In the presence of an external electric field, energy levels for a given transition are split into separate degenerate sub-levels. These sublevels are identified by the quantum number m_J (the z component of the total angular momentum J). In most cases, the transitions between the sublevels are not symmetric, which results in an asymmetric shift line [2, 5]. On the other hand, if the splitting of the sublevels is not too large, then a symmetric-broadened

line will result. Regardless, the splitting causes broadening and a wavelength shift in the emission line of that transition. In the case of SIBS and LIBS, the electric field experiments come from the collisions of electrons, ions and the charged nature of the plasma. Stark broadening is the main broadening mechanism seen in plasmas resulting from both SIBS and LIBS analysis [4, 5, 63, 64].

2.7.2 Self-Absorption

Spectral lines that arise through the combinations between the ground level and the lowest excited levels are called resonance lines. When these lines are absorbed and excited, the emission transition is to the ground state, and often, resonance lines are very strong [65, 66]. Therefore, resonance lines are confined to states combining with the ground state. If the electrons in a particular atom only come from the ground state, the electron can only absorb those photons capable of inducing a transition from this same ground state. This is why there are so few resonance lines in relation to all the spectral lines of the atom [60]. The mention of resonance lines is important due to the fact that these lines have a very large probability of re-absorption before leaving the plasma discharge. This is known as self-absorption, which tends to broaden the profile of the spectral line. In extreme cases of self-absorption, the peak of the spectral line will appear to be flattened. Self-reversal is another issue that occurs when the excitation temperature drops around the outer regions of the discharge region and the passage of the light through these colder gas layers. When self-reversal occurs, the line not only broadens but also shows an intensity dip at the resonance frequency [66]. This phenomenon can be

easily mistaken for doublets. Broadening due to resonance lines that give rise to self-absorption and self-reversal can cause problems when analyzing data. A false line width will appear to artificially elevate electron density, which in some calculations, correlates to the overall concentration of the element within a sample. Self-absorption also leads to saturation of signal intensity. Thus, at high elemental concentrations within a sample, the peak intensities begin to decrease. As a consequence, attempting to simply correlate signal intensity to concentration of an element becomes invalid when self-absorption of spectral lines is observed.

Chapter 3 : Plasma Physics

In chapter 2, the theory of atomic emission was discussed in detail. In this chapter, the physics of plasma both in LIBS and SIBS is explained. Since SIBS is similar to LIBS, the same physical aspects may be applied to the understanding of plasma characteristics created from various samples. The use of a high intensity laser beams to produce plasmas has been an active research topic for several years. A laser beam has the capability to dissociate, excite and ionize the constituent atomic species in the sample being studied. In addition, SIBS also has the capability to dissociate, excite and ionize a sample of interest through the use of a highly energized electrical spark. Both of these methods produce a plasma, which expands either in the vacuum or in the ambient gas depending on experimental conditions. When laser-matter interaction occurs, various processes may occur such as ablation of material, high energy particle emission, and emission of radiation ranging from the visible to hard X-rays depending on the intensity of the laser [4]. Although there are many applications to these various processes, the research presented in this dissertation focuses on the study of optical emission from plasma. This chapter outlines the basic physics of plasma relevant to LIBS and SIBS. Some calculations mentioned in this chapter were not performed during these analyses. However, these calculations were discussed in general terms throughout this dissertation. Thus, a brief description is necessary for the understanding of these terms and calculations.

3.1 An Introduction to Laser-Matter Interactions

Several authors over the years have reviewed material on laser-matter interactions [67-69]. When a focused, high-powered laser beam or a high voltage spark (in the case of SIBS) interacts with a target material (solid, liquid, gas, or aerosol), the sample is exposed to extreme local heat and evaporation. Once this occurs, the reaction is followed by plasma formation. A plasma is a local assembly of atoms, ions, and free electrons, overall electrically neutral, in which the charged species often act collectively [5]. In general, plasmas are characterized by many parameters, the most basic being the degree of ionization. Plasmas can either be weakly ionized or highly ionized. Weakly ionized plasmas are where the ratio of electrons to other species is less than 10%, where highly ionized plasmas may have atoms stripped of many of their electrons. This results in very high electron to atom/ion ratios [5]. It is known that LIBS plasmas usually fall into the category of weakly ionized plasmas.

The interaction between the laser beam or spark with a solid material is very complex. In LIBS, this ablation process is based on many variables which include the power of the laser, the laser pulse width, and spatial and temporal fluctuations of the laser. SIBS also has variables such as spark power and repetition rate, as well as the spatial and temporal fluctuations associated with the spark. In addition, the target material itself plays an important role in laser or spark-induced ablation. The chemical and physical properties of the target material, whether it be a solid, liquid, or gas, affects the outcome of the laser-matter interactions.

3.2 Plasma Fundamentals

Plasmas are considered to be a distinct phase of matter, and their properties are different than liquids, solids and gases. In fact, plasmas have often been described as a fourth state of matter [70]. Plasmas have a high electrical conductivity due to the presence of charged particles within them. Plasmas have free moving electrons and ions, whereas in a gas, they are bound to the atom. In order to create a plasma, energy is required to separate the electrons from the atoms and/or molecules. In the case of both LIBS and SIBS, plasma creation results from intense heat as the source of energy, which allows for vaporization, excitation and ionization of the sample and the surrounding atmosphere. These plasmas are typically very hot, and in the early formation, consist of ions and electrons. Atoms and molecules are present as the plasma cools over time. Plasmas also interact with their surrounding environment, which is an important factor in supporting the propagation or quenching of the plasma [71].

The hot expanding plasma interacts with the surrounding gas mainly by two mechanisms:

- (1) The expansion of high pressure plasma compresses the surrounding gas and drives a shock wave, and
- (2) During this expansion, energy is transferred to ambient gas by the combination of thermal conduction, radiative transfer and heating by shock wave [4, 71].

Figure 3.1 illustrates how the hot vapor plasma interacts with the surrounding ambient atmosphere. Understanding how the plasma interacts with its environment is imperative to interpreting the results from the plasma creation. In addition, the evolution of the plasma depends on the intensity of the laser, its wavelength, size of focal spot, target vapor composition, ambient gas composition and pressure [71]. It has also been found that the plasma parameters such as radiative transfer, surface pressure, plasma velocity, and plasma temperature are strongly influenced by the nature of the plasma [4]. At early times of the plasma, the degree of ionization and vaporization is high (Figure 3.1). Over time, electron-ion recombination occurs, followed by neutral atoms and then molecules form. The outer region of the plasma consists of the shock wave that is in front of the region containing the line emission. At low irradiance, the vapor plasma is too thin to produce energy efficiently by radiation. This results in a lack of plasma formation, and the inability to produce ionization in the sample and sample atmosphere. On the other hand, if high irradiation exists, then shock heat dominates, and produces a large shock wave front [71].

3.3 Plasma Shielding

During laser ablation, there are three primary processes and mechanisms that occur. These include: plasma ignition, plasma expansion and cooling, and the ejection of particles from the sample surface and condensation. Each of these processes depends of the laser irradiance and pulse duration and therefore on the formation and subsequent evolution of the plasma [72]. The vapor produced by the laser interacts with the latter

time of the laser pulse, which can be absorbed by the laser induced plasma. This is known as plasma shielding and it influences how much of the laser energy reaches the sample surface to initiate ablation [73]. As a result, plasma shielding influences how much of the solid mass is converted into vapor [4]. For example, Shaikh *et al.* performed electron density and temperature measurements of ND:YAG-induced zinc plasmas. The laser was operated at 1064, 532, and 355 nm, while maintaining the same laser power density ($4 \times 10^{10} \text{ Wcm}^{-2}$) for each wavelength [74]. Results indicated that the plasma electron excitation temperature increased at longer laser wavelengths. This was attributed to a more efficient laser-plasma interaction and energy transfer. The plasma electron density also decreased with longer wavelengths due to the increased amount of target material ablated (at shorter wavelengths). This led to reduced plasma shielding. A discussion of plasma shielding as it relates to pressure is discussed in Chapter 7 of this dissertation.

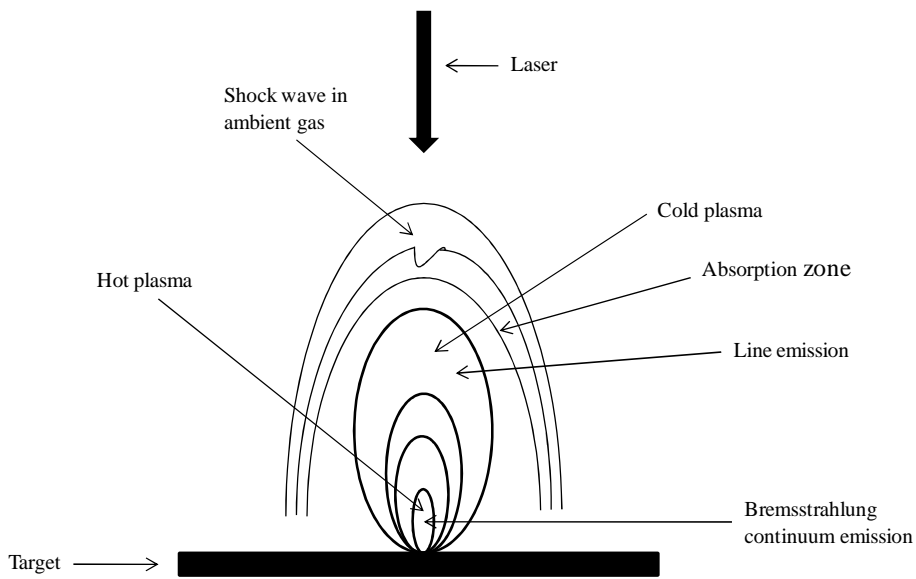


Figure 3.1 Schematic diagram of expanding laser produced plasma in ambient gas. The plasma plume has several zones, all of which are labeled. The plasma temperature cools with increased distance from point of impact. Adapted from Singh and Thakur, 2007 [4].

3.4 Plasma Models

Plasmas are generally separated into two main classifications: Local Thermodynamic Equilibrium (LTE) plasmas and Coronal Equilibrium (CE) plasmas [2]. LTE plasmas are characterized by a single temperature (order of 10^4 K), and usually have electron densities greater than $\sim 10^{15}$ cm^{-3} . CE plasmas on the other hand, are characterized by higher temperatures (order of 10^6 K) than LTE plasmas but low electron densities ($\sim 10^8$ cm^{-3}) [2, 62]. There is a third plasma model known as the Collisional Radiative Steady State (CRSS), but it is less commonly seen. This model describes plasmas that fall between the LTE and CE plasmas [70]. Generally, plasmas produced by LIBS and SIBS are treated as though they fall into the regime of LTE [5]. Therefore, the CE and CRSS plasmas are not encountered during this work and will not be described.

3.4.1 Plasmas Having Local Thermodynamic Equilibrium

It is important to briefly discuss LTE plasmas traditionally found in LIBS research. In the case of LTE plasma, it is treated as having a single temperature. This means the free electrons, ions and neutral species making up the plasma are assumed to all be at the same temperature ($T_{\text{ion}} = T_{\text{electron}} = T$). In the LTE model, both atomic and ionic states must be populated and de-populated by collision processes rather than radiative processes [75]. For the LTE model to be valid in a plasma, the collisions with electrons have to dominate over the radiative processes, which requires a sufficiently large electron density [76]. McWhirter proposed a criterion that was based on the existence of a critical electron density for which collisional rates are at least ten times the

radiative rates [77]. In order to maintain a high collision rate, the electron density must be sufficiently rich so that following criterion is satisfied by the plasma to be in LTE

$$N_e \geq 1.6 \times 10^{12} \Delta E^3 T_e^{1/2} \quad \text{Equation 3.1}$$

where ΔE (eV) is the energy difference between the upper and lower states, T_e (K) is the excitation temperature. In the expanding plasma, LTE is only possible locally, and for a specific time segment during the plasma evolution. It typically takes approximately 1 μ s for full LTE conditions to stabilize in a static plasma at $T \sim 10,000$ K and $N_e \sim 10^{16}$ cm⁻³ [2]. However, LTE conditions will never exist for the entire lifetime of the plasma.

Some researchers contend that the assumption of LTE within typical LIBS plasmas is questionable, with spectroscopic analysis yielding different electron and ion temperatures for a given plasma. Although the use of LTE may not be a mutually agreed upon model that describes the plasma formation condition for qualitative analysis, this model points out the fact that time delay is crucial for obtaining the best operating conditions in the SIBS and LIBS plasma [4]. The relationship between LTE and plasma temperature is further discussed in section 3.5.4.

3.5 Plasma Spectral Emission

Chapter 2 discussed spectral emission as it relates to atomic emission. However, it is important to discuss spectral emission properties as they relate to the plasma. In

addition, an in depth review of continuum emission, temporal and spatial resolution and plasma temperature and pressure will be in this chapter.

3.5.1 Continuum Emission

As discussed in chapter 2, the continuum is primarily due to free-free (Bremsstrahlung emission) and free-bound (recombination) events. Shortly after plasma initiation, the emitted light is dominated by Bremsstrahlung radiation, derived from the recombination of free electrons and ions which has little intensity variation as a function of wavelength [78]. In the Bremsstrahlung process, photons are emitted by electrons accelerated or decelerated in collisions with positively charged ions, and is characterized by a high intensity of “white light” [5]. However, Bremsstrahlung radiation decays rather quickly, and therefore, the weaker atomic radiation produced by both ions, neutral species and molecules can be detected as sharp emission lines or bands. By delaying the light collection after plasma generation and Bremsstrahlung radiation, atomic and molecular features of interest can be detected with high signal to background ratios [78-80]. The time delay necessary is contingent on the energy used to make the plasma and the conditions under which it expands. This delay allows for radiation transition (free-bound) to be observed. In radiation transition, a free electron is captured into an ionic or atomic energy level, and transfers its excess kinetic energy in the form of a photon [4]. Figure 3.2 is a schematic overview of the temporal profile of a single laser pulse from a LIBS plasma. This figure illustrates that at early times, the plasma is dominated by the continuum radiation produced by the laser pulse. The temporal difference between the

laser irradiation and the beginning of the observation window is called the delay time (t_d). After a designated delay time, the gate width, or collection window occurs. This is known as t_b , and is the region in which the signal is collected. Clearly, the plasma characteristics change over time, and therefore it is important to determine the ideal delay. The ideal collection conditions vary depending on the power and wavelength of the laser. This is also true for SIBS in that as the power of the spark changes, differences will be seen in the length and intensity of the continuum emission.

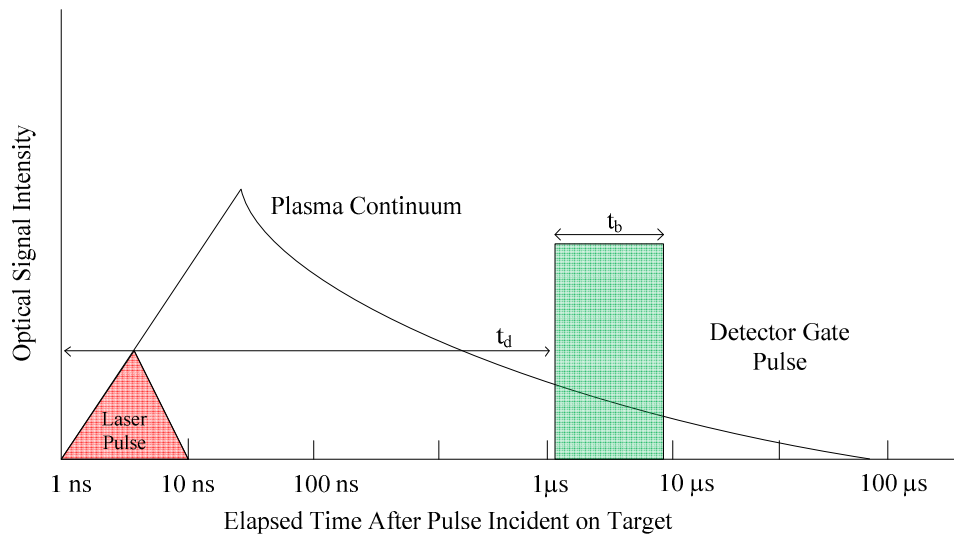


Figure 3.2 A schematic overview of the temporal profile of a LIBS plasma derived from a single laser pulse. Adapted from Cremers, 2006 [5].

One example, performed by Hohreiter (2004), studied the LIBS plasma continuum emission at three different wavelengths (270 nm, 400 nm and 530 nm) against time (ns) [81]. The continuum emission of all three bands peak between 20 and 40 ns were collected following the peak of the plasma initiating laser pulse. For all three spectral bands, the continuum emission was observed to decay by one order of magnitude during the first 200 ns. This represents a decrease in the temperature of approximately 70% based on emissive power per the Planck distribution. The 70% decrease in temperature is consistent with other reported temperature measurements [81]. Even though the background continuum decays faster than spectral lines, information is still available from the data. Therefore, by using time resolution of the plasma light, one can discriminate between the regions where the signals of interest predominate. Thus, recording line emission for the purpose of elemental analysis depends on choosing the proper delay time, when the ratio of line emission to background continuum emission has been optimized.

Another example by Camacho *et al.* (2010) studied the time-resolved evolution from laser-induced air plasma [82]. They showed that during the initial stages after the laser pulse, the continuum emission dominates the spectrum. As time evolves, N^+ , O^+ , and O^{2+} emissions dominate the spectrum. These ionic lines quickly decrease for higher delay times, and the emission lines become progressively and spectrally narrower as a consequence of the electron number density and variation. This indicates that the electron density and excitation temperature decrease during the plasma expansion [82].

A study conducted by Ciucci *et al.* examined trace pollutants in soil by time-resolved laser-induced breakdown spectroscopy [83]. Certified soil samples (Geochemical Exploration Reference (GXR-2) silicate) from the United States Geological Survey (USGS) were obtained. Figure 3.3 is a result from the use of GXR-2 at 1064 nm. This figure shows that the plasma continuum emission dominates the spectra in the early stages of plasma development. Conversely, the line emission, which is characteristic of the trace elements present in the soil sample, becomes evident at longer time delays [83].

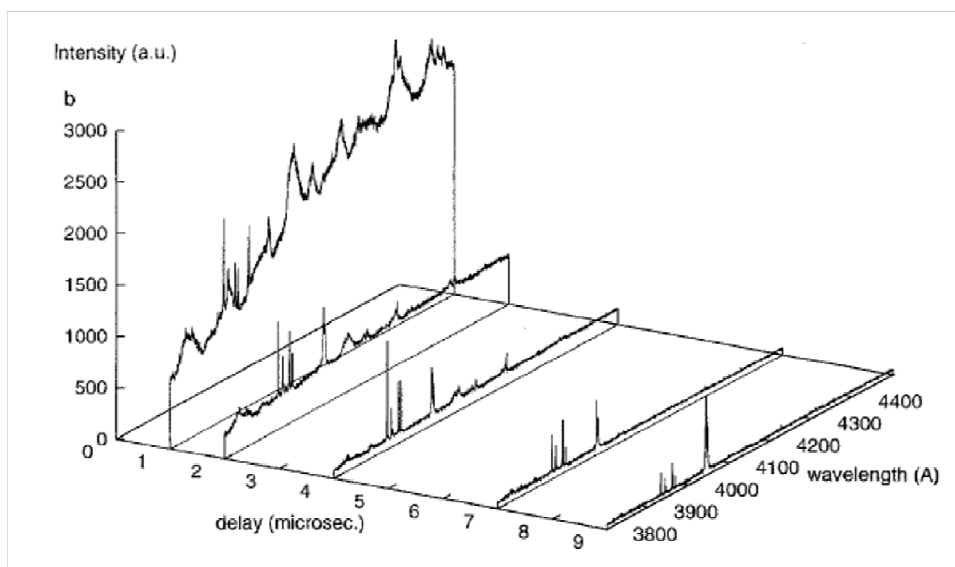


Figure 3.3 Dynamics of the emission from the GRX-2 sample measured upon excitation at 1064 nm as a function of the delay from the laser pulse. The gate width is fixed at 1 μ s. Reprinted with permission from Springer Publishing Company [83].

Based on the examples given, it is evident that for each experiment, one must determine the optimal delay and collection conditions. It is important to note that there are differences between SIBS and LIBS in the plasma production, volume, and delay timing. These differences will be discussed in later chapters.

3.5.2 Electron Density

The electron density of a plasma is essentially the number of electrons present in the plasma per unit volume. Knowledge of the temperature and electron density is vital to the understanding of the dissociation, atomization, ionization and excitation processes occurring in the plasma [84]. Line widths are related to the electron density in the plasma, and therefore, proportional to Stark Broadening. One can determine electron density of discharge plasma from the measurement of Stark broadening of spectral lines. The following expressions relate line width and shift to electron and ion densities [5, 61]

$$w_{total} \sim [1 + 1.75A(1 - 0.75r)](n_e / 10^{16})w \quad \text{Equation 3.2}$$

$$d_{total} \sim [1 \pm 2.00A(1 - 0.75r)](n_e / 10^{16})d \quad \text{Equation 3.3}$$

where w_{total} is the measured half-width at half maximum (HFHM), A is a parameter giving the ion contribution, r is the ratio of the mean distance between ions to the Debye radius and w is the HWHM Stark width caused by the electron density. If A is 0, then the electron density is $10^{16}/\text{cm}^3$ [5]. Although studying the electron density of any given plasma is important, specific measurements were not conducted in any of the SIBS or

LIBS experiments reported here. However, generalized discussions of electron density as it relates to specific experiments are discussed throughout this dissertation.

3.5.3 Plasma Opacity

Plasma opacity is another important aspect to plasma physics, and can be used as a diagnostic tool. There are two categories of plasma opacity, and they include optically thick and thin plasmas. A plasma is considered optically thin when the emitted radiation escapes along the length of the plasma without significant absorption or scattering. The intensity of radiation emitted from a plasma is given by

$$I(\lambda) = [\varepsilon(\lambda) / \alpha(\lambda)] \{1 - \exp[-\alpha(\lambda)L]\} \quad \text{Equation 3.4}$$

where $\varepsilon(\lambda)$ is the emissivity and $\alpha(\lambda)$ is the absorption coefficient [5]. When α is small, the plasma is considered optically thin. In addition, the ideal condition is for the plasma to be optically thin, which results in a reduction of lines that are not re-absorbed. Thus, a plasma that is optically thin is not associated with the lines involving the ground state [66]. On the other hand, when optically thick plasmas are present (high plasma density), the plasma itself absorbs its own emission and results in spectral line re-absorption and in extreme cases, signal saturation. As mentioned in section 2.7.2, self absorption poses a problem when measuring the peak area, and results in the inability to convert peak area to concentrations. An emission line that is not self-absorbed will best fit a Lorentzian profile, where a self-absorbed line will fit a Gaussian profile [85, 86].

3.5.4 Plasma Temperature

Plasma temperatures are another important aspect to understanding the complex spectroscopic sources as well as improve their applications [87]. The temperature can be determined through spectroscopy from the measurement of ratios of the intensities of ion to neutral lines and neutral to neutral lines from the same element [4]. If a thermodynamic equilibrium is achieved, then a single plasma temperature ($T_{\text{ion}} = T_{\text{electron}} = T$) can be defined. However, in the expanding plasma, a complete thermodynamic equilibrium is never achieved, and instead, the approximation of LTE is used. This approximation assumes that within a particular region, the equilibrium does not vary. However, the equilibrium may still vary from region to region. In order for this approximation to be applicable, a sufficient number of collisions must occur to thermalize the plasma. In other words, energy must be spread in the plasma across volume and species. It should be noted that LTE may not be achieved for all species at the same time. Heavier species (atoms and ions) do not equilibrate as fast as light species (electrons) due to the fact that particles of similar masses tend to share energy more equally with the colliding particles. The more the particles interact within a plasma, the longer it takes to reach equilibrium [5, 71].

The method for determining the temperature in an LTE plasma is based on the theory that the number densities in various excited states follow the Boltzmann distribution [4]. From this, a Boltzmann temperature may be calculated, and typically involves the intensity of multiple emission lines from a wide variety of upper states. The most widely method used to determine temperature is through a Boltzmann plot, which

provides the excitation temperature from the measurement of the line emissions from a single species. The simplest Boltzmann plot (temperature) may be obtained from two emission lines, having enough difference on their upper energy levels [88-90].

Chapter 4 : Development of Early Soil Carbon Analysis by SIBS

In this chapter, the experimental details, instrument design and the study of soil carbon experiments are described using SIBS. Theoretical discussions related to these methods and instruments are found in Chapters 2 and 3.

4.1 Rationale of Soil Carbon Analysis by SIBS

In recent years, soil carbon sequestration has become an important topic in the broader discussion and study of the influence of atmospheric CO₂ on climate change. Soil carbon sequestration is the process of fixing CO₂ from the atmosphere into the soil through crop residues and other organic solids, and in a form that is not immediately reemitted. Agriculture soils are responsible for a portion of greenhouse gas emissions over the last several hundred years, through the conversion from forest and rangelands to crops, intensification in cropping patterns and land management practices, and combustion of fossil fuels for agricultural use [91, 92]. The conversion of land to agricultural use disrupts and depletes soil carbon, and invariably results in a net loss of soil C [93]. For example, estimates on a global basis suggest that current agricultural practices and land use modification account for approximately one-fifth towards the radiative contribution towards global warming. Because these agricultural soils are now relatively C depleted, they represent a potential CO₂ sink if a portion of the lost carbon can be regained [94]. CO₂ can be stored in the soil through no-till planting, restoring

wetlands, converting cropland to permanent grass or trees, planting conservation buffers or using cover crops [95].

Encouraging efficient soil CO₂ sequestering is significant because it helps to offset emissions from fossil fuel combustion and other carbon-emitting activities while enhancing soil quality and long-term agronomic productivity. Several studies in the 1990's were started to assess the C sequestration potential on agricultural soils in industrialized countries [92, 96, 97]. For example, Lee and Phillips studied the effects of no-till practices in concurrence with planting winter wheat as a cover crop in the US corn belt [96]. For this study, an erosion productivity impact calculator (EPIC) model was used. The researchers selected statistically representative sample at 100 sites in the US corn belt, and ran a 100 year simulation at each site. The results suggested a change from current tillage practices to widespread use of no-till plus winter cover could conserve and sequester a total of 3.3×10^6 tons of carbon per year (t-C yr⁻¹) in the soil for the next 100 years [96]. Thus, researchers suggest that soil carbon sequestration can be accomplished by reducing soil disturbance through no-till crops or the replacement of annual crops with perennial vegetation, for example [21]. Therefore, the development of new instrumentation to monitor carbon content of soils is critical in reducing the time spent determining the long-term viability of soil carbon sequestration.

Determining changes in soil C is difficult due to the small, inter-annual changes in the total carbon stored in soils [22]. Due to the fact that small changes in C must be measured to accurately determine and verify soil C, real-time measurement of the C in soils is important to assessing the efficiency of this process. LIBS has recently been used

to quantify carbon in soils. da Silva *et al.* measured total carbon in whole tropical soil using a portable LIBS system from StellarNet (model PORTA-LIBS-2000) [98]. Six soil samples (0.3 to 0.7 %C) from the Brazilian Cerrado region were submitted to quantitative measurements of carbon. These authors noted that tropical soils are rich in iron oxides; and due to strong spectral interference of iron with the C 247.86 nm line, the C 193.09 nm line was used instead. Using this emission line, they reported correlation coefficients of 0.91, indicating the potential of using a portable LIBS systems for quantitative carbon measurements on tropical soils [98]. This is just one example of many (see Chapter 1) where LIBS has been applied to the measurement of carbon in soils. However, LIBS is still a relatively new analytical technique, and there are several disadvantages. For example, LIBS plasmas are quite small. The typical LIBS plasma have dimensions of approximately $3.0 \times 10^{-4} \text{ cm}^3$ produced from a 100 mJ Nd:YAG laser [71]. For comparison, the spark formed in SIBS has a visible volume on the order of $7.0 \times 10^{-2} \text{ cm}^3$ [6]. Although the size of the plasma is dependent on the energy output of the laser, the small excitation volume contributes to the very large spark-to-spark variations in emission intensities and high detection limits [6]. In addition to reduced sensitivity, the LIBS technique has the additional disadvantages of fragility and large laser power supply. Both of these liabilities limit the sensitivity and ability for LIBS to be a robust, portable instrument. In comparison to LIBS, SIBS systems typically have large plasma volumes and are substantially more rugged in design; thus the development of soil carbon analysis by SIBS was explored.

This chapter focuses on the application of SIBS to the measurement of carbon in soil to enable monitoring of soil quality and relative sequestration permanence. Early applications of SIBS to monitor metals in soil involved the production of sparks near the soil surface [12]. This previous work was based on a relatively uncontrolled presentation of the soil to the spark (described in Chapter 1). Thus, direct spark formation on soil presented some challenges. Because of the motion induced in the sample by the blast wave from the spark breakdown itself, smaller soil particles are actually removed from the spark gap, and the larger, heavier particles remain near the electrodes. In this way, the sample is progressively distilled until only the large particles are being sampled. Also, the early application of SIBS to soils did not include the quantification of carbon but instead, only studied metals in soil. This chapter reports the development and evaluation of a new sample delivery mechanism to the spark gap, and the prediction of carbon in soil.

4.2 Preliminary Soil Carbon Analysis

As previously mentioned, SIBS has been applied to the analysis of heavy metals in soils [16]. This early work provided the basis for the development of a field-portable SIBS instrument to measure and monitor carbon in soils. To assess the potential for SIBS to measure soil carbon, a small set of soil samples were collected and evaluated. The following sections present the soil processing, characterization, instrumentation, design and modeling needs for the analysis of the initial soil carbon studies.

4.2.1 Soil Processing and Characterization

A total of eight soil samples were collected from the Denver, CO metro area and New Mexico (B). One sample (G) was collected on the University of Denver campus. Three samples (C, E and F) were collected from crop fields around Parker, CO, which is approximately 45 kilometers (km) southeast from Denver. Another sample (A) was collected approximately 16 km miles southeast of Parker, CO. The last samples (D and H) were collected from pine forests in Elizabeth, CO, which is approximately 60 km southeast of Denver. The soil location and description of the 8 soils used for this initial study are summarized in Table 4.1. The soil description is listed to illustrate the types of soils analyzed during this research. The majority of soils originated in Colorado, and the soils are either clay or sand loams. It is important to note that no data could be found on the Web Soil Survey (WSS) concerning the University of Denver soil.

Table 4.1 Soil location, description and rating of 8 soil samples. *Information obtained from the USDA Web Soil Survey [99].

Soil ID	Location	Soil Description*
A	39°29'07.60"N, 104°36'26.46"W	Bresser Sandy Loam: Sandy loam, Sandy clay loam
B	33° 12' 23"N, 105° 52' 23"W	Gravelly fine sandy loam
C	39°27'54.97"N, 104°41'26.57"W	Fondis Clay Loam: Clay loam, Clay
D	39°21'44.93"N, 104°35'04.82"W	Elbeth Sandy Loam: Sandy loam
E	39°25'30.32"N, 104°36'22.02"W	Bresser Sandy Loam: Sandy loam and Sandy clay loam
F	39°29'04.22"N, 104°36'27.16"W	Bresser Sandy Loam: Sandy loam and Sandy clay loam
G	34°40'26.16"N, 104°57'42.85"W	No Data from WSS (University of Denver)
H	39°21'23.03"N, 104° 34'12.39"W	Elbeth Sandy Loam: Sandy loam

Table 4.2 Total carbon and nitrogen values for 8 soils. Standard deviations reported were determined by three trials for each sample. *Indicates samples that were not further used in analysis due to high standard deviation. ** Indicates standard deviation values were not available.

Soil ID	C (%)	±	N (%)	±
A*	1.74	0.55	0.11	0.010
B*	4.61	0.54	0.11	0.005
C	1.35	0.14	0.10	0.004
D	1.94	0.25	0.10	0.010
E	2.23	0.25	0.20	0.009
F	0.71	0.12	0.08	0.009
G	2.38	**	0.34	**
H*	3.64	1.76	0.19	0.065

In preparation for SIBS analysis in the DU laboratories, the samples were dried by placing all samples in an oven at 80 °F for 1 hour. Most researchers either air dry or oven dry soils, and routine oven drying of all soil samples is not required [100]. In addition, the soil analysis handbook of reference methods states that an oven can be used to dry soil samples [101]. But, temperatures should not exceed 38°C (100°F), as significant changes in the physio-chemical properties of the soil can occur at elevated drying temperatures [101].

After the samples were dried in the oven for one hour, the samples were removed from the oven to finish air drying overnight. Once samples were dry, any large twigs, rocks or roots were removed prior to grinding with mortar and pestle. Then, each soil was sieved to remove particles larger than 1mm in diameter (18 mesh size). All soils were placed in air tight, sealed bags at room temperature until further analysis was performed. Each sample was placed in a Cianflone ball grinder for 1 minute to homogenize the soil before the CHN analysis of the soils. This extra step was necessary because of the very small sample sizes used in the CHN analysis (15-17 mg). The soils were then analyzed for carbon with the CHN analyzer at the University of Denver (DU) with an EA 1108 Carlo Erba CHN analyzer. The CHN analysis results from DU are found in Table 4.2. Three (denoted by *) of the samples were not included in the data set used in the regression analysis. This was due to highly variable combustion carbon data (large standard deviation), indicating sample inhomogeneity. Sample G did not have a reported standard deviation for both carbon and nitrogen values from CHN analysis (Table 4.2).

4.2.2 Instrumentation and Soil Delivery

An aliquot of each soil, approximately 4 grams, was placed in a modified plastic syringe with the tip of the syringe cut off. The syringe was then placed in a Cole Parmer syringe pump set at 18.3 mL/hr. The syringe pump and syringe were both placed at an angle above a funnel to the electrode spark gap so that the soil would fall through the gap at a gradual rate. This set-up was positioned below the syringe filled with soil, and provided for gradual flow of soil through the spark gap during analysis. As the soil fell through the spark gap, the power supply (VTech Engineering Corporation, Andover, MA) was set so that sparks occurred at 1 Hz. The power supply was set at 700 mJ, and the electrodes were positioned approximately 4 mm apart. The spark is a two-step phenomenon in which an initial arc event (high voltage and low current) occurs to reduce the electrical resistance of the air in the electrode gap before a capacitor bank discharges across the spark gap. Full discharge of the spark circuitry has a time constant of approximately 8–10 μ s, during which time the plasma is formed and the sample ablated. The electrode material used throughout this research is proprietary, and will not be discussed in this dissertation. The collection fiber optic consisted of fiber optics made by CeramOptec Industries, Inc. (East Longmeadow, MA) mounted to a lens tube that collected emissions from the sparks. The fiber optics was coupled to a 1/4 m spectrometer with a 1200 lines/mm grating and an Andor iStar intensified charged-coupled device (ICCD, South Windsor, CT, USA) with 1024 pixels. Figure 4.1 is a schematic diagram of the SIBS instrument for the analysis of soils. The spectrometer has an approximate 40 nm collection window. As the soil particles were processed by the

spark, light from both atomic and molecular emission was focused into the optical fiber and transmitted to the spectrometer and then to the ICCD. Both the 193 nm and 248 nm wavelength regions were investigated to establish the optimal carbon feature for this research. In addition, the 363 nm wavelength region was investigated for optimization of the CN (B-X) molecular features. These regions are discussed in the following sections.

4.2.2.1 Intensified Charged-Couple Device (ICCD)

Charged-coupled devices (CCDs) are types of multichannel detectors in which movement of electrical charge can be converted into a digital output. This is accomplished through a photoactive region (transducer) made up of a silicon layer, and a transmission region which allows for the movement of the accumulated charges to the detection area [1]. An image is projected onto the capacitor array, causing each capacitor to accumulate an electric charge proportional to the light intensity at that location. Once the array has been exposed to the charge, a control circuit causes each capacitor to transfer its contents to its neighbor (known as the shift register). The charge at the last capacitor is transferred into a charge amplifier, where the charge is converted into a voltage that is proportional to the radiant intensity. After amplification, the signal is converted from analog to digital, and to a computer that controls the readout [102]. An ICCD is a CCD that is connected to an image intensifier mounted in front of the CCD. The microchannel plate (MCP), is the image intensifier in the ICCD and used to amplifying light. It works by converting the incoming photons to electrons on the detector side by photoemission. The electrons are then amplified, and the electrons

released from the MCP then strike the fluorescent screen and cause it to emit far more light than was incident on the photocathode [103]. The amount of incident light can be controlled, and is known as the MCP gain. The higher the MCP number, the brighter the output signal will be. The MCP allows for the ICCD to be gated, where one can control the time at which light (data) is collected as well as the observation window (length of data collection). The ability to gate this device is the one major advance the ICCD has over the CCD. A gate width is the time frame in which data is collected, whereas the delay time is the time at which the start of data collection occurs. These values are referred to in the following sections of this dissertation.

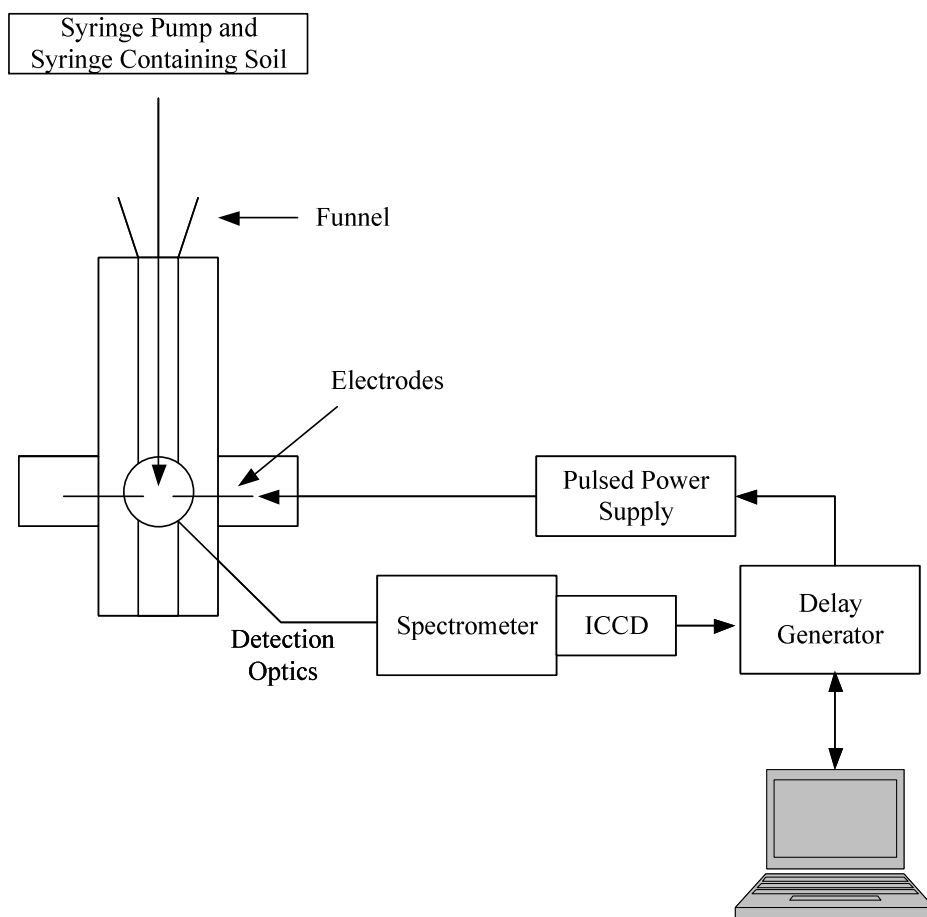


Figure 4.1 Schematic diagram of SIBS design for soil analysis. Soil falls from the syringe into the funnel and through the spark gap.

4.2.3 Establishment of the Optimal Spectral Region for Analysis

The first objective of this project was to establish the optimal carbon line for the analysis of total carbon in soil. The research group focused on two neutral atomic carbon (C I) lines at 193.09 nm and 247.86 nm. At each spectral region, a sample of activated charcoal was introduced into the spark gap. Activated charcoal was initially chosen due to the high carbon content and relatively simple matrix. Use of this sample matrix facilitated the identification of the C (I) line, and minimized (if not eliminated) interference from other elements with the carbon lines of interest. The collection conditions included a 10 μ s gate width, MCP 150 and the delay times varied from 10 μ s to 40 μ s. At each delay time, data was summed for 50 sparks at a rate of 1 Hz. Figure 4.2 is a sample spectrum of activated charcoal in the 248 nm region.

Once both carbon lines at 193.09 nm and 247.86 nm were established, a more complicated matrix was used to determine if there were any interfering lines with carbon. For this, two LECO (LECO Corporation, St. Joseph, MI) synthetic carbon standards were used. One standard had a carbon concentration of 0.14% (Part no. 502-632) and the other 0.53% (Part no. 502-630). There were two primary reasons for using these samples. First, the group wanted to establish that the instrumentation could detect the carbon line at low concentrations, and second to test the ability of the instrument to detect C in a complex matrix. Figure 4.3 is a sample spectrum of the 0.53% carbon LECO standard in the 193 nm region. Figure 4.4 is a sample spectrum of the 0.53% carbon LECO standard in the 248 nm region. The carbon line can be detected, and is noted. In addition, the instrument was also able to detect the carbon line in the lower, 0.14% carbon LECO

standard in the 248 nm region. Due to the highly ionized N and O lines surrounding the C (I) line in the 193 nm region, no further analysis was collected in this region.

Finally, soil sample A was used to verify the findings from the activated charcoal and LECO standards. Figure 4.5 is a sample spectrum of soil A in the 248 nm region. The neutral carbon line of interest is detected, and the soil matrix is more complex than both the activated charcoal and LECO standards. Based on this information, the C (I) in the 248 nm region was determined to be the optimal line of interest. This conclusion was reached because, while the line at 193.09 nm was observed, it was not observed to be as intense as the lower energy (247.86 nm) feature (Figure 4.3). This may well be because of the limitations of the fiber optic materials selected to transmit the light to the detection system, and/or the potential influence by bright nearby ionized nitrogen and oxygen features which prevented the increase of the gain on the ICCD used to acquire the data. In the 248 nm region, it was further demonstrated that electrode material for SIBS produced no interference lines in relation to the C line.

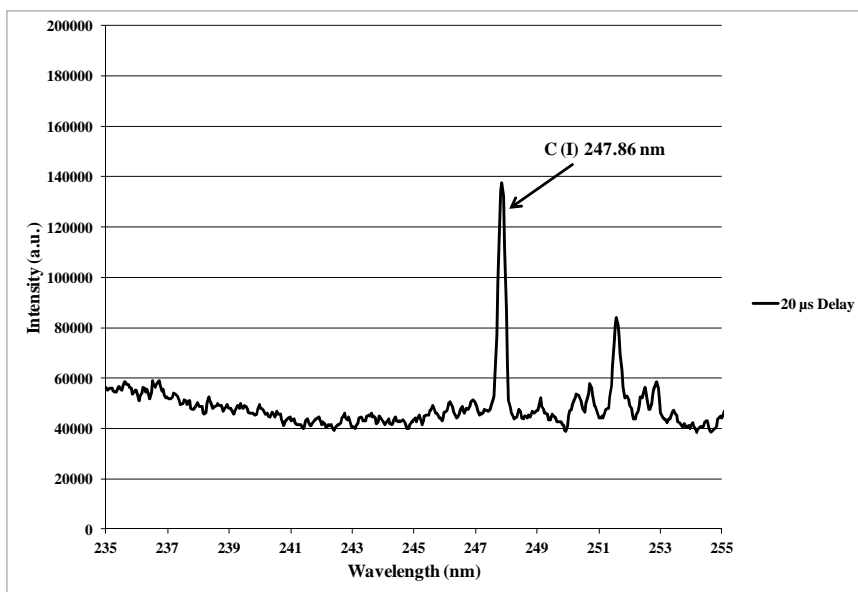


Figure 4.2 A sample spectrum of activated charcoal in the wavelength region of 248 nm, with a 20 μ s delay time. The C (I) line is labeled.

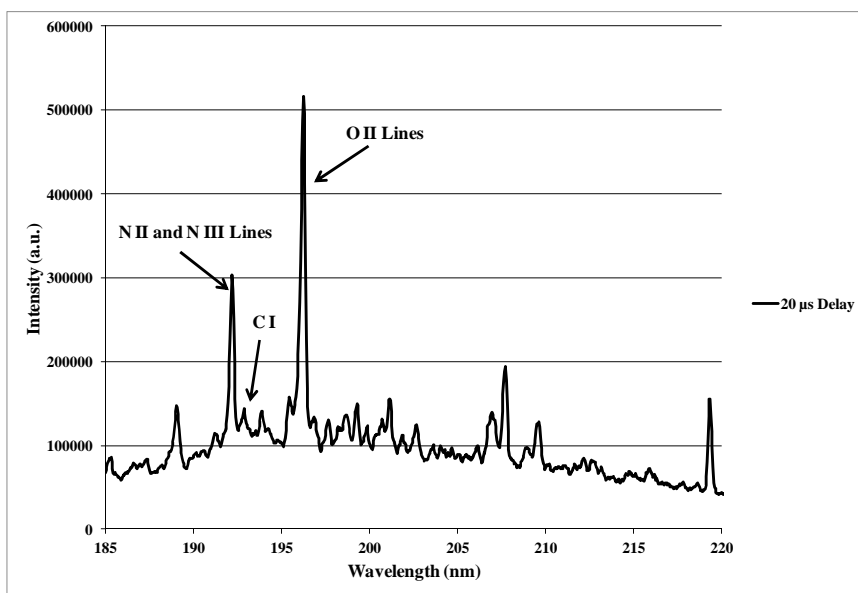


Figure 4.3 A sample spectrum of LECO synthetic carbon standard (0.53 %) in the wavelength region of 193 nm, with a 20 μ s delay time. The C (I) line is labeled, as well as the nearby O and N features.

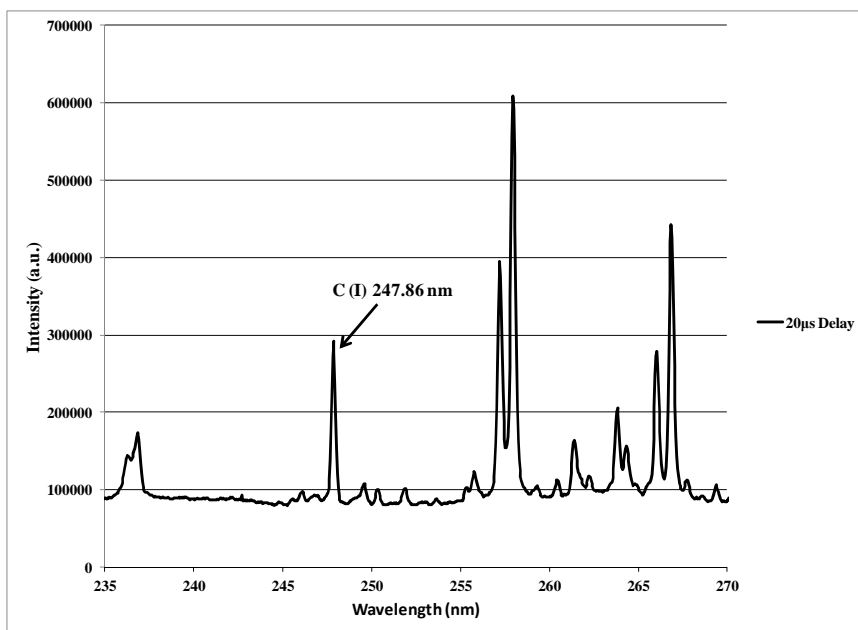


Figure 4.4 A sample spectrum of LECO synthetic carbon standard (0.53%) in the wavelength region of 248 nm, with a 20 μ s delay time. The C (I) line is labeled.

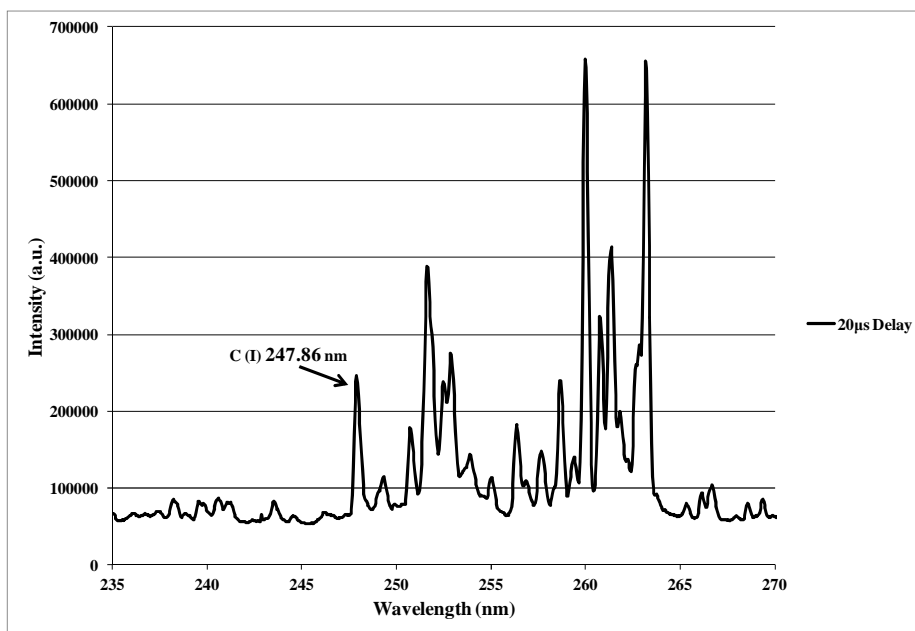


Figure 4.5 A sample spectrum of soil A in the 248 nm wavelength region, with a 20 μ s delay time. The C (I) line is labeled.

4.2.3.1 Investigation of the 363 nm Wavelength Region

In addition to atomic lines in the 248 nm region, molecular features associated with C in the 300 nm to 400 nm wavelength region were studied. Specifically, research focused on identifying the CN (B-X) vibrational band at 358 nm and 388 nm. These spectral features are of interest since they might provide information that may make differentiation of organic and inorganic carbon fractions possible. It has been reported that the CN (B-X) feature is related to organic molecules, and therefore, it might be possible to use information in this region to distinguish between organic and inorganic carbon fractions [104-106]. Figure 4.6 is a sample spectrum of soil A in the 355-395 nm region, and the CN molecular features are labeled. This preliminary data confirmed the observation of the CN feature, and the following section will provide details on the optimization of both atomic and molecular features of interest.

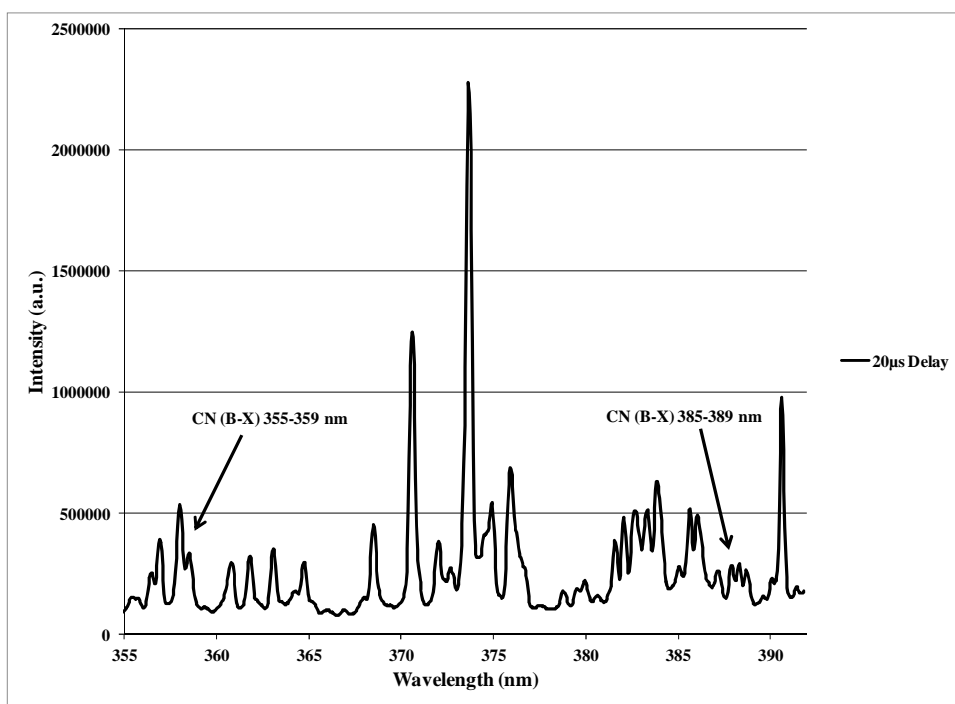


Figure 4.6 A sample spectrum of soil A in the 355 to 395 nm region, with a 20 μ s delay time. The CN vibrational features of interest are labeled.

4.2.4 Collection Conditions

In order to establish the optimal collection conditions in both the 248 nm and 363 nm region, data acquired at several delay times were evaluated. A single soil was used in this analysis in both spectral regions. First, the 248 nm region signal was studied, with the goal of optimizing the intensity of the neutral carbon line. A data series was collected with a delay range of 1-40 μs and a gate width of 1-300 μs . It was established that the optimal collection conditions consisted of an 11 μs delay, a 60 μs gate width and a MCP of 50. The spectrometer was then centered at the 363 nm region, and the same process was performed to optimize the CN (B-X) molecular feature. The optimal collection conditions for the CN (B-X) intensity included a 20 μs delay, a 21 μs gate width and a MCP of 10.

Three to six trials were taken with each soil sample in both the 248 and 363 nm wavelength regions. The specific collection conditions used in the two regions were the optimized conditions described above. During each trial, data was summed for 50 sparks at a rate of 1 Hz. Using these conditions, 3 to 6 averaged spectra were acquired in each wavelength region for each soil sample. These spectra were compared to the CHN values (Table 4.2), and evaluated by multivariate analysis, and are described in section 4.3.

4.3 Regression Analysis

Spectral data acquired with the modified syringe/pump arrangement were evaluated by both univariate and multivariate analysis techniques. Five different soil

samples were analyzed. Three samples were not included because combustion carbon data was quite variable, indicating material inhomogeneity that would not be beneficial to include in the model (Table 4.2). Three of the samples were analyzed in triplicate with the SIBS instrument, with the other two samples being analyzed six times. Using the C emission peak at 247.86 nm, the data were first evaluated by ordinary least-squares (OLS) regression using peak intensity (after baseline correction).

The same data were then evaluated by multiple linear regression (MLR). MLR is an extension of linear regression techniques where more than one response is considered during the regression [107]. In this case, the spectral data over a five nm window (245 nm to 250 nm) were used in the regression. A commercial software package, Solo (Eigenvector Research Inc., Wenatchee, WA), was used to evaluate the data. Data were pre-processed by mean-centering both the spectral intensities and carbon (%C) values.

The data were also evaluated using principal component regression (PCR) and partial least squares (PLS) analyses. These techniques rely on developing models based on a calibration set of data projecting data of higher order onto lower dimensional space. In both regression techniques, matrix algebra is used to reduce the complexity of the data. In the case of PCR, the data are projected into clusters of data that are then given a new coordinate system. This new coordinate system is described with principal components (PCs), with PC 1 describing the dimension in which the data cluster has the highest variability. Each subsequent PC (ie, PC2, PC3, etc.) is orthogonal to all previous PCs and contains less information than the previous PC. In the case of PCR, only the variability (error) in the x-block data (spectral data) is considered. Thus, like OLS, error

in the values of the y-block data (soil %C) is neglected. PLS models, however, have the ability to account for variability in both the x- and y-block data. Therefore, the coordinate system to describe the clusters of data in PLS are described by latent variables (LV), with LV1 describing the most dimension of highest variability, followed with higher LVs that describe (or capture) less and less of the variability in the data cluster [107, 108].

4.4 Regression Analysis Results

A representative plot of the PLS model is shown in Figure 4.7. The figure represents the results of using 5 LVs to fit the data. A better correlation ($r=0.973$, $n=21$) was observed when compared to the OLS, MLR and PCR regressions. In Figure 4.7, the green line represents the perfect 1:1 correlation between measured and predicted values; the red line represents the best-fit line for the data.

The data were all used to create the calibration model. In PCR and PLS models, a step can be added to perform a validation of the model as the model is being developed, and is termed cross-validation [109]. In calibration models generated here, cross-validation model of random splits was used. In this technique samples are randomly removed from the calibration set and used as test samples on a model that is generated with the remaining samples. This is an iterative process, and is continued until the error of the calibration model is minimized [110].

A summary of the different regression techniques used to evaluate the data are provided in Table 4.3. In addition to correlation coefficients, the root mean square error

of calibration (RMSEC), root mean square error of calibration-validation (RMSECV), limit of detection (LOD) and limit of quantitation (LOQ) are provided for comparison of the techniques. The units of RMSEC and RMSECV represent error in percent since the regression plot is measured vs. predicted % carbon. For example, a value of 0.13 represents a prediction error of a value of 0.13%. Meaning, if one is trying to predict a soil sample that has 2% carbon, then the error is $\pm 0.13\%$. For LOD and LOQ calculations, the standard deviation, s , of the predicted concentration of the sample with the lowest %C was determined. Using this value, the LOD was calculated for each regression such that $LOD = 3s/slope$ (of the regression). LOQ was calculated in a similar fashion; $LOQ = 10s/slope$. Although this initial study consisted of a small data set, the results were promising. The data in Table 4.3 indicate that SIBS followed by a partial least squares analysis is capable of predicted total carbon in soils.

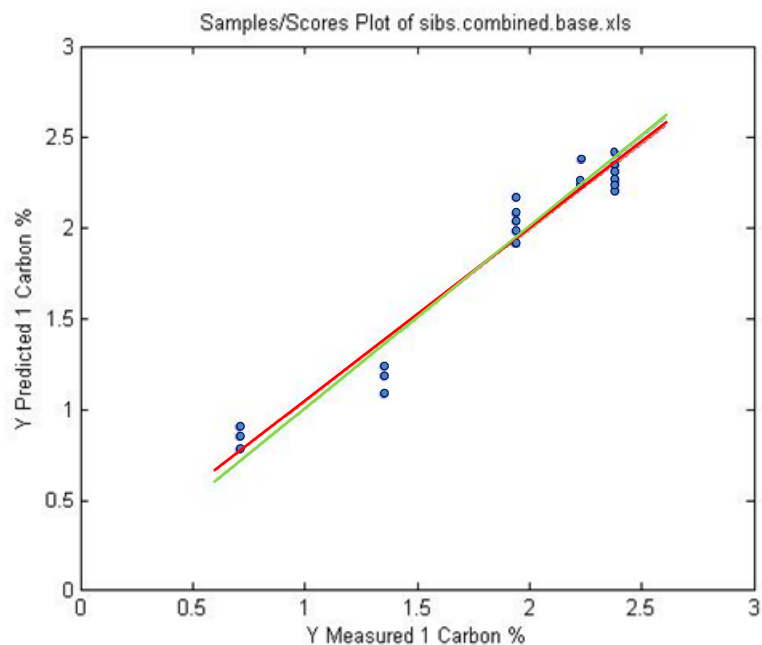


Figure 4.7 Measured vs. predicted carbon % levels from PLS analysis using 5 LVs.

Table 4.3 A summary table of the different regressions that were used to evaluate the data.

Summary Table of Regression Analysis

Regression Method	r	RMSEC	RMSECV	LOD (%C)	LOQ (%C)
OLS	0.808	-	-	0.42	1.40
MLR	0.937	-	0.214	0.91	3.03
PCR (3 PC)	0.835	0.314	-	0.27	0.89
PLS (3 LV)	0.943	0.190	0.270	0.29	0.96
PLS (4 LV)	0.966	0.148	0.270	0.22	0.74
PLS (5 LV)	0.973	0.131	0.232	0.20	0.68

4.5 Chapter Conclusions

The initial experiments described in this section resulted in the development of sample delivery hardware to the spark gap of the SIBS instrument, and some preliminary data analysis that demonstrated the possibility of the application of SIBS to a portable soil carbon monitor. During this phase, a successful spectral location was established where carbon emission lines are present and easily excited with the electrodes. Several local soil samples were collected and carefully characterized for total carbon. Subsets of the SIBS spectra of these characterized soils were subjected to a variety of univariate and multivariate data analyses. Using SIBS and partial least squares fitting with 3-5 latent variables, an estimate of total carbon in soil over a range of 0.71 – 3.64 % with a detection limit of between 0.2-0.3 % by dry weight was achieved. Although a small sample set was used for this experiment, reasonable results were found. The 350 nm to 400 nm spectral region was also studied to locate the CN (B-X) molecular feature. Results indicated that the SIBS instrument could detect this feature. Since the soil samples were only analyzed for total carbon and nitrogen percentages, the fraction of the inorganic and organic carbon was not known. Thus, the CN (B-X) feature was not included in any regression analysis. This study was useful in moving forward to the next phase of research, which was to develop a robust and fieldable SIBS soil carbon monitor.

Chapter 5 : The Development of a SIBS Portable Soil Carbon Analyzer

This chapter describes the experimental details, instrumentation and results for the initial development and miniaturization of a SIBS portable soil carbon analyzer. This research builds on the results found in Chapter 4. The objective of this phase of research was to analyze both soils and surrogate soils to provide key insights for the development of a robust predictive model. In addition, an evaluation of the first generation miniaturized SIBS analyzer for the quantitation of carbon in soil was performed. This chapter discusses each of these processes, and presents preliminary results of the SIBS instrumentation. The majority of the research in this chapter was peer reviewed and published in 2012¹.

5.1 Introduction

During this phase of research, several experiments were conducted in order to build upon and improve the SIBS instrumentation for the analysis of carbon in soils. In addition to analyzing soil samples, clay-based surrogate soils were analyzed in order to better understand the carbon spectral response. The analysis of both types of medium (soils and surrogate soils) was proposed to provide spectral data over a variety of carbon sources over varying concentrations, so that the most appropriate calibration technique

¹ Schmidt, M.S., et al., *Spark-induced breakdown spectroscopy and multivariate analysis applied to the measurement of total carbon in soil*. Applied Optics, 2012. **51**(7): p. B176-82

for the instrument could be selected. Thus, the analysis of signal response of three different carbon sources (elemental, organic and inorganic) was evaluated. In addition, a quantitative evaluation of the effect of spectral near-neighbors, such as Fe and Si, was performed. In particular, it is not clear how C, in the form of carbonate, contributes to the C intensity at 247.85 nm when contrasted with organic carbon (OC) in the sample. Although these surrogate soils are simplified and do not represent the complexity of the true composition of soils, they still provide insight on the fundamental emission line properties.

The signal response of Fe clay surrogates were also used to aid in the development of a robust predictive model. The rationale for studying the signal response is due to the fact that there are several Fe lines that either underlie the C (I) feature or are found nearby. Since these Fe lines dominate the 248 nm spectral region, a fundamental understanding of the emission intensity, including the impacts on the C feature from both the varying analyte concentrations and matrix effects, will aid in the development of a robust predictive model. By using known concentration of Fe in clays, the possible signal effects on C emission lines due to the presence of Fe can be monitored.

The study of the molecular feature, CN (B-X), to correlate the organic portion of total carbon was discussed in Chapter 4. In addition to accurately predicting TC using the portable SIBS analyzer, another goal of this research was to also try to predict separately OC and inorganic carbon (IC). Currently, the quantitation of C is a multistep process that must be performed in a laboratory setting. If a robust model can be built to predict all three fractions of C (TC, IC and OC), then it has the potential to produce a

rapid method for quantification of carbon in soils. Thus, this chapter also describes the use of the CN (B-X) region as part of the multivariate model in order to predict OC. The current approach is to use the TC and OC values determined through an independent laboratory in the model, along with the spectral regions around 248 nm (C (I) line) and 360 nm (CN (B-X)). Predictions of both TC and OC are determined from a model including these signals, and the IC fraction is determined by difference. This chapter describes the various approaches in the development of a multivariate model to predict carbon in soil through the use of a portable SIBS analyzer.

5.2 Experimental Design

5.2.1 Soil Processing and Characterization

To develop data analysis methods for optimizing the SIBS instrument, a total of nine soil samples were collected from Colorado, New Mexico, and Oklahoma (Table 5.1). The latitude and longitude coordinates were recorded for each soil sample, and soil classifications were determined from the USDA WSS [99]. Soil samples 1-6 were also used during the initial data analysis found in Chapter 4. Soil samples 7-9 were collected specifically for this research in order to diversify the soil types previously analyzed. Therefore, samples 1-6 were preserved from the previous research, and were refrigerated (5°C) during this portion of research. After samples 7-9 were collected, they were processed just as samples 1-6 were, and this information can be found in Chapter 4. All

soil samples were then stored in a refrigerator (5°C) until needed for further processing and analysis [100, 111].

Table 5.1 Soil location and description of 9 soil samples. * Information obtained from the USDA Web Soil Survey [99]. ** Denotes sample that was not used in regression analysis.

Soil ID	Location	Soil Description*
1	39°29'07.60"N, 104°36'26.46"W	Bresser Sandy Loam: Sandy loam, Sandy clay loam
2	33° 12' 23"N, 105° 52' 23"W	Gravelly fine sandy loam
3	39°27'54.97"N, 104°41'26.57"W	Fondis Clay Loam: Clay loam, Clay
4	39°21'44.93"N, 104°35'04.82"W	Elbeth Sandy Loam: Sandy loam
5	39°25'30.32"N, 104°36'22.02"W	Bresser Sandy Loam: Sandy loam and Sandy clay loam
6	39°29'04.22"N, 104°36'27.16"W	Bresser Sandy Loam: Sandy loam and Sandy clay loam
7**	34°26'57.34"N, 98°57'47.59"W	Tillman-Hinkle complex
8	34°26'56.35"N, 98°56'8.72"W	Vernon clay
9	34°26'49.02"N, 99° 0'38.48"W	Tillman silt loam

In addition to the initial processing of soils found in Chapter 4, further steps were added during the soil processing of the soils for this phase of research. CHN analysis is the standard for carbon analysis in soils. Thus, the research focused on preparing each sample as if the samples were going to be subjected to CHN analysis. Research literature recommends the soil must pass through a minimum of a 100 mesh (150 μm) sieve prior to CHN analysis. This is a critical step in sample preparation in order to obtain reproducible samples by reducing sample inhomogeneity [100, 112]. During the first phase of research, the soils were not homogenized to a minimum of 100 mesh prior to analysis (Chapter 4). However, the bulk soil for each sample was saved, and soil subsets were further processed using the following procedure.

Soils were sieved sequentially through various mesh sizes (4, 10, 20, and 40 mesh), and then placed in a ball mill grinder for 4 minutes to homogenize the soil. Each soil sample was then sieved to obtain a 200 mesh (75 μm) particle size. After homogenization and sieving, soil samples were refrigerated (5°C) until SIBS analysis was performed [100, 111]. Each mesh size fraction was saved and refrigerated in order to study the effect of soil particle size on signal intensity. Samples 1-6 were reanalyzed for carbon, and all nine soils were submitted to the Colorado State University (CSU) Soil, Water, and Plant Test Laboratory (Fort Collins, CO) to determine total carbon (TC) by a dry combustion CHN analyzer. In addition, the OC and IC (calculated from CaCO_3) fractions for each soil were determined. Elemental analysis was performed to determine Fe and Si content of all nine soils through HF acid digest followed by inductively coupled plasma optical emission spectroscopy (ICP-OES). Table 5.2 lists the results of

TC, IC, OC, Fe and Si for each of the nine soil samples. As noted in Table 5.2, soil sample 7 has an OC fraction higher than TC. These results make no sense; thus was not used in the regression analysis.

Table 5.2 Percent of TC determined by CHN analysis. Percent IC and OC determined by difference. Elemental results of Fe and Si determined through HF digest followed by ICP-OES. ** Denotes sample that was not used in regression analysis.

Soil ID	TC (%)	OC (%)	IC (%)	Fe (%)	Si (%)
1	1.62	1.54	0.08	1.56	38.30
2	4.31	3.02	1.29	1.53	35.30
3	1.39	1.25	0.14	1.80	39.70
4	2.50	2.38	0.12	0.52	39.30
5	2.22	2.15	0.07	1.63	39.70
6	0.64	0.58	0.06	1.66	41.70
7**	4.06	4.22	0.04	1.25	41.60
8	0.84	0.82	0.03	1.44	41.80
9	0.90	0.84	0.06	1.17	42.80

5.2.2 Surrogate Soil Analysis

One primary goal of this portion of the research was to obtain curves of growth (COG) for C and Fe. Additions of C and Fe sources were added to clay gravimetrically to produce surrogate clays with similar concentrations found in soil. This was done to study the SIBS response of C and Fe in the spectroscopic regions of 248 nm and 363 nm. KGa-1b (IN 47907-2054) from the Clay Minerals Society Source Clays Repository (Washington County, Georgia) was used as a base for the surrogate soils. KGa-1b was chosen due to it being a well-characterized and relatively inert matrix, and the negligible Fe and C concentrations. Table 5.3 provides a summary of the composition KGa-1b of the relevant elements for this research.

Table 5.3 Composition and relative percentages of the major components found in KGa-1b.

Chemical Composition	%
SiO₂	44.2
Al₂O₃	39.7
TiO₂	1.39
Fe₂O₃	0.13
FeO	0.08

5.2.3 Construction of Samples for Curves of Growth (COG) Experiments

Carbon was added to the clay substrate and analyzed in three forms: elemental (coal, NIST SRM 2683b), organic (potassium hydrogen phthalate (KHP), Sigma Aldrich) and inorganic sources (K_2CO_3 , Sigma Aldrich) over a range of 0-10%. The surrogate soil samples were made gravimetrically, with the difference in mass made up of clay (Kaolin). To simulate iron levels, iron oxide (Fe_2O_3) was added to the clay over the range of 0-10%. The source of the Fe_2O_3 was from a certified Fe sample (Thorn Smith). Table 5.4, Table 5.5, Table 5.6 and Table 5.7 illustrate the composition of the surrogate soils analyzed, as well as the range of carbon or iron found in the surrogate soils.

Table 5.4 Table of organic carbon in the form of KHP added to KGa-1b in the range of 0-10.8 % C.

Clay (g)	KHP (g)	Mix (% Carbon)
3.00	0.00	0.00
3.00	0.10	1.58
3.04	0.20	2.95
3.02	0.31	4.34
3.01	0.51	6.81
3.06	0.71	8.82
3.03	0.90	10.80

Table 5.5 Table of inorganic carbon in the form of K₂CO₃ added to KGa-1b in the range of 0-8.69 % C.

Clay (g)	K₂CO₃ (g)	Mix (% Carbon)
3.00	0.00	0.00
3.14	0.51	1.21
3.04	1.01	2.16
2.00	2.00	4.35
1.01	3.05	6.53
0.00	4.00	8.69

Table 5.6 Table of elemental carbon in the form of coal added to KGa-1b in the range of 0-9.46 % C.

Clay (g)	Coal (g)	Mix (% Carbon)
3.00	0.00	0.00
3.11	0.05	1.08
3.03	0.11	2.23
3.02	0.20	4.15
3.08	0.30	5.96
3.09	0.41	7.73
3.02	0.50	9.46

Table 5.7 Iron in the form of iron oxide (Fe_2O_3) added to KGA-1b in the range of 0-10.04 % Fe.

Clay (g)	Iron (g)	Mix (% Iron)
3.00	0.00	0.00
3.10	0.05	0.84
3.10	0.11	1.81
3.01	0.25	4.11
3.03	0.41	6.36
3.19	0.55	7.87
3.11	0.72	10.04

Each sample set was analyzed by the SIBS instrument, and the known concentrations were plotted as a function of either the baseline corrected neutral C (247.86 nm) or Fe (248.32 nm) peak intensity in the 248 nm region. All samples were analyzed in both the 248 nm and 363 nm regions. However, only the Fe lines in the 363 nm region were compared with the known concentrations of the surrogate soils, and the molecular feature of CN (B-X) was not analyzed during this portion of research. Initially, a univariate calibration approach was applied to the surrogate soils as well as the preliminary data from the nine soils collected at PSI. This method consisted of relating two single variables (peak intensity vs. concentration, for example) to each other, and is one of the simplest methods to perform [113]. This approach is called classical least squares (CLS). In this research, the concentration of a single element was compared to the measured peak intensity. This preliminary study was done to determine if a linear correlation existed between both measured C and Fe and the signal intensity obtained from the SIBS instrument. Results of the analysis of surrogate soils are reported in section 5.6.1.

5.3 Sample Delivery – Impact of Particle Size

The impact of soil sample size using the screw-feed delivery technique was investigated to evaluate the reproducibility of the mass of soil delivered to the spark. The purpose of these sample delivery experiments is to understand how the particle size impacts signal reproducibility within in an individual sample set as well as determine the optimal soil preparation required for SIBS analysis.

Sample delivery response was studied with three soils (4, 7 and 8) in this investigation. The three particles sizes were generated: 20, 100, and 200 mesh, which correspond to 850 μm , 150 μm and 75 μm maximum diameter, respectively. The three mesh sizes were determined in the following manner. Any particles that passed through the 20 mesh and not the 40 mesh sieve, was considered a 20 mesh sample. Any particles that passed through the 100 mesh and not the 200 mesh were considered 100 mesh sample. The 200 mesh sieve was the smallest used, so therefore, all soil particles that passed through the 200 mesh were kept as a 200 mesh sample.

Each of the three soil samples at each mesh size were analyzed in the 248 nm region. Specifically, the signal of the carbon line (247.86 nm) was evaluated to determine the differences in both peak intensity and shot-to-shot variability between each of the three mesh sizes.

5.4 Instrumentation of Soil Analysis

The following sections discuss the evolution of the SIBS analyzer instrumentation. The SIBS instrumentation was designed by PSI. During the initial phase of this research, a screw-feed design was implemented and used as a new technique to deliver soil to the spark gap. In addition, higher resolution was achieved through the use of a different spectrometer. The first data were collected at PSI. Midway through this project, the first portable SIBS analyzer for carbon was built by PSI and was delivered to DU for data analysis. These changes and new instrumentation are documented in section 5.4.2.

5.4.1 Initial SIBS Screw-Feed Instrumentation

The SIBS instrumentation consists of a soil sample delivery system, spark gap, collection optics, spectrometer, an ICCD and a pulsed current power supply. A schematic of the system is shown in Figure 5.1. The soil was placed in the hopper with a constant voltage (10V) applied to the gear motor; this voltage was maintained throughout all data collection. Soil samples were delivered from the hopper to the spark gap using a screw-feed mechanism. This method delivered soil via a feed screw, driven by a variable-speed DC gear motor, to the sample chamber where it falls in a thin stream through the spark gap. The use of a motorized screw-feed allowed for an automated delivery of soil to the spark gap. In theory, this method also provides a constant flow of soil through the spark gap, to minimize shot-to-shot variability due to inconsistencies in soil delivery.

As the particles passed through the spark gap and were ablated by the plasma, atomic emissions were focused into an optical fiber bundle and transmitted to a 1/3 m spectrometer with a 2400 lines/mm grating coupled to an Andor iStar ICCD (Andor Technology, South Windsor, CT). 400 mJ sparks were delivered at 1 Hz to the gap from an Arc-2 pulsed current power supply (VTech Engineering Corporation, Andover, MA). The power supply dimensions measure 3" x 4" x 9" (H x W x L) and weighs approximately 7.5 pounds. This generation of the power supply is considerably smaller and lighter than the previous power supply (5" x 20" x 22", 15 pounds) used to collect data during the initial phase of research found in Chapter 4 (section 4.2.2). The Arc-2

power supply delivers controlled energy pulses through the spark gap formed by the electrodes in order to produce a plasma.

The collected range of the spectrum is ± 10 nm around the center wavelength of 248 nm. The data acquisition conditions were 7 μ s delay from the plasma pulse and a 50 μ s gate width. Signals from each soil were collected for 2 minutes at 1 Hz, giving a total of 120 replicate spectra within each sample file. These conditions were held constant for all soil and surrogate soil acquisitions. In addition, these conditions were held constant during data collection in the 363 nm region. Initially, a univariate analysis was applied to the C (I) line as performed on the surrogate soils. This first data evaluation compared the OC and TC concentrations to the baseline corrected peak intensities of the soils. These results are reported in section 5.6.3. The procedure for the PLS regression analysis performed on this data is presented in section 5.5.1, and the results of these analyses are reported in section 5.6.4. Results reported in this section were from data collected at PSI prior to the development of the portable SIBS analyzer.

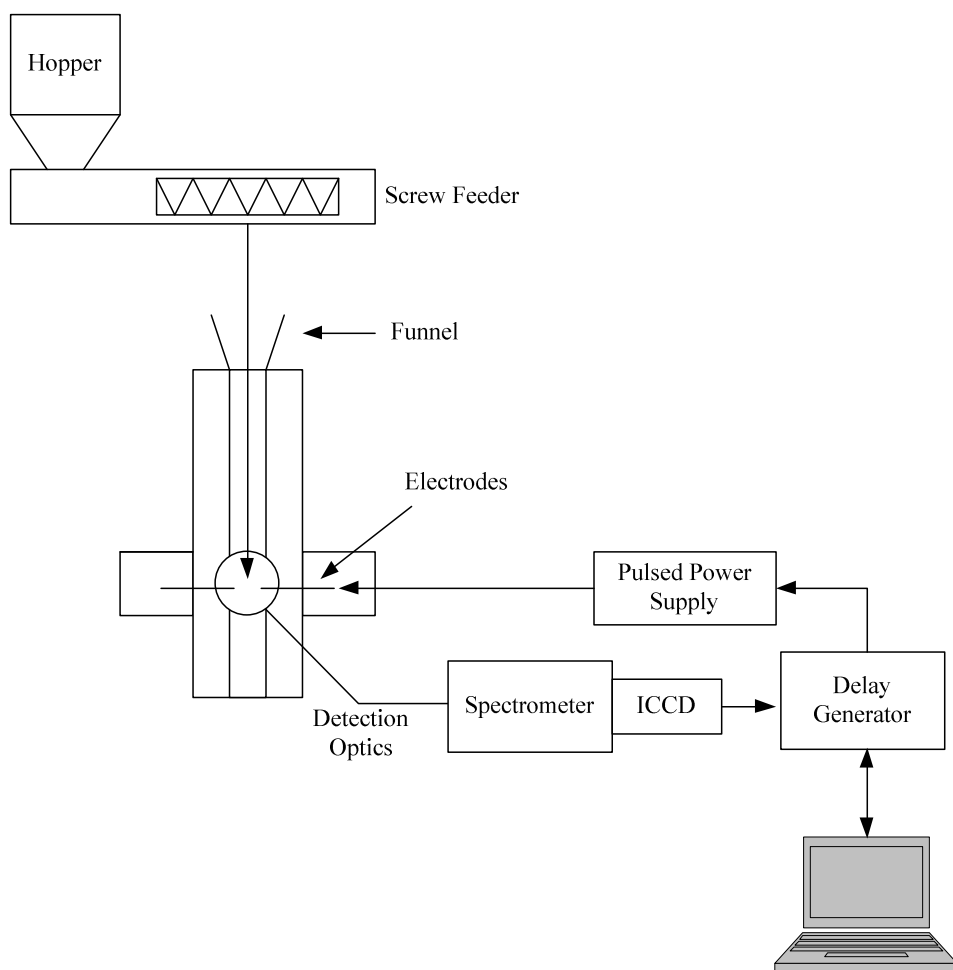


Figure 5.1 Schematic diagram of the SIBS instrumentation [18].

5.4.2 Miniaturization of SIBS Instrumentation

Over the course of this phase of research, PSI designed and built a portable SIBS analyzer. This second system, seen in Figure 5.2 is a schematic diagram of the first portable SIBS prototype for the analysis of soils. In order to miniaturize this instrument, several changes were made to the previous design. The same hopper and screw-feed design was used, however the spark chamber was made smaller. The spark chamber was coupled to collection optics and fiber optic bundle. The fiber optics were split, and fed into two Avantes, Inc. (Broomfield, CO) miniature spectrometers. The first spectrometer covered the 240 nm to 300 nm wavelength region, while the second spectrometer covered the 300 nm to 400 nm wavelength region. Each spectrometer was equipped with a 2048 pixel CCD detector. The lower wavelength spectrometer had a 3600 lines/mm grating installed, which produced a resolution of 0.06 (FWHM). The higher wavelength spectrometer had a 2400 lines/mm grating installed, which produced a resolution of 0.09 nm (FWHM). Each spectrometer had an entrance slit width of 10 μm . In addition, the more compact power supply described in section 5.4.1 was added as part of the portable SIBS analyzer.

A SIBS control module software was developed specifically for this instrument in order to control the power supply and data collection. The laptop runs the software, which has a main graphical user interface (GUI) that controls the following: the power output of the power supply, synchronization pulse to the Avantes spectrometers module, and acquisition of the spectra from the Avantes module. Thus, the operator can control

all the SIBS data acquisition parameters through a single user interface. Figure 5.3 includes photographs of the portable SIBS instrumentation.

5.4.2.1 Data Acquisition Conditions Using the Portable SIBS Analyzer

After the portable SIBS soil analyzer was delivered to DU, all nine soils were reanalyzed on this instrument. This was to verify all components of the instrument were functional, as well as to make sure that the spectral results on the new instrument were in agreement with those previously found. A 1-Hz collection rate was maintained, and sample replicates were collected over a 2 minute period. In general, two replicates were collected for each soil sample; thus, a total of 240 shots were collected sequentially and simultaneously in both the 248 nm and 363 nm region for each soil sample. The delay time was set to 22 μ s, while the gate width of the spectrometers was 1 ms. The 1 ms gate width is the minimal width for this instrument. Therefore, no control or optimization of the gate width was performed during these experiments. Sections 5.5.2, 5.6.5 and 5.6.6 include discussions and results from the use of the portable SIBS analyzer.

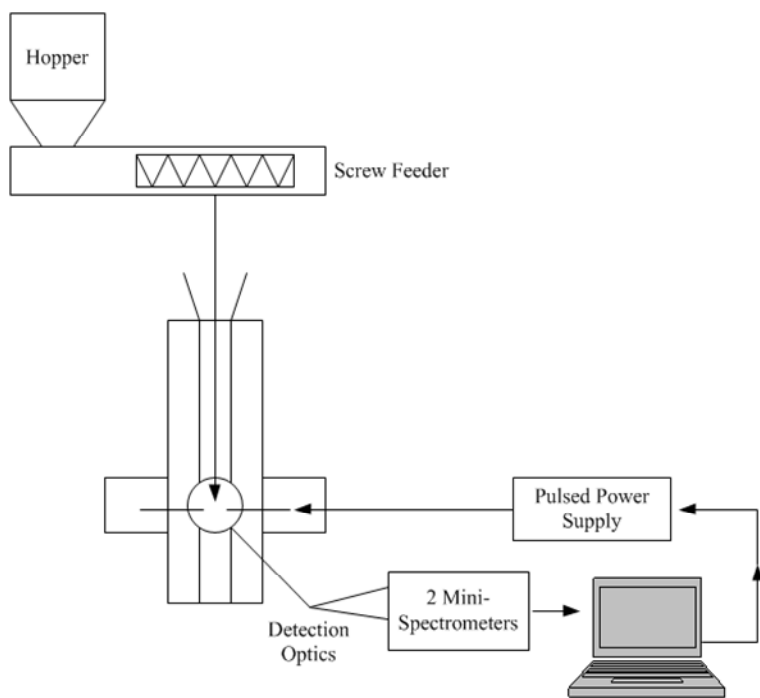


Figure 5.2 Schematic diagram of the first SIBS portable soil analyzer.



A



B

Figure 5.3 Prototype of the portable SIBS soil instrumentation. A) External casing which houses the SIBS instrumentation. B) Side view of the hopper, screw-feeder and spark chamber, as well as the power supply.

5.5 Data Processing and Statistical Model Development

The following section describes the introduction and development of a multivariate model to predict carbon in soils. The inclusion of additional elements (Fe and Si) was used in the model in order to determine their effects on the prediction of C in soil. The following section outlines the preliminary multivariate development.

5.5.1 Initial Regression Analysis

Data processing and modeling was performed on the nine soils analyzed at PSI prior to the miniaturization of the instrumentation. The 120 replicates for each sample (8 total due to the elimination of an outlier, Table 5.2) were first analyzed by principal component analysis (PCA) using multivariate software (PLS Toolbox, Eigenvector Research, Inc. Wenatchee, WA) to identify and remove outliers. As stated in section 5.2, each sample was homogenized and filtered through a 200 mesh sieve to ensure homogeneous samples in soil composition and density. Consistent sample density is important in delivery to minimize variations in plasma temperature that may give a change in signal. Changes in signal intensity from variations in sample density may create outliers that PCA analysis will remove. The criteria for identifying outliers were based on screening each set of data with the Hotelling's T^2 (the multivariate analogue to Student's t) and residual values of the spectra. The use of the T^2 in control chart applications has been reported as a technique to identify outliers where multiple components are varying [114]. In this work, those spectral acquisitions that were outside of a 95% confidence interval were considered outliers. Following outlier removal, each

removed spectrum was inspected, comparing the spectral response to the average spectral data to determine if PCA correctly identified the outliers. All outliers identified by the PCA approach had Si and/or Fe peaks that were statistically different (3 standard deviations) from the average of all 120 acquisitions. At most, the PCA analysis removed 12 replicate spectra from the 120 spectral sets. Because of the careful soil preparation, these outliers were attributed to inconsistent soil delivery or data collection without a soil sample. Spectra that failed to meet the criteria were discarded from all subsequent calculations.

After outlier removal, ten replicate acquisitions were summed for each of the soils samples creating a total of 10 subsamples for each of the 8 soils. These acquisitions were selected randomly so that individual acquisitions would not be summed in multiple samples. In this manner, 10 replicate samples for each of the soils were created. These data were then used to create a spectral data matrix for the regression analysis by PLS. PLS is a regression technique that has widespread use in chemical, environmental and engineering applications, and indeed has become one of the standard tools in the field of chemometrics [110, 114-116]. In PLS, numerous X-block variables can be modeled with several response variables (Y-block) [110, 115]. For this work, the spectral region (X-block) was truncated to 243 nm to 253 nm including the spectral region of the dominant C, Fe and Si spectral lines. A concentration matrix (Y-block) was created from C, Fe, and Si concentration values of the 8 soil samples obtained from ICP-OES and CHN analysis.

In order to determine the precision and accuracy of the CHN analyzer, three calibration block soils (3 samples with 5 replicates each) and two certified C standards were reanalyzed by CSU for total C (TC) by CHN analysis to ensure accuracy of the calibration. In the case of the soil samples, the maximum reported difference in measured TC was 0.01%; both reported TC from CHN agreed to within 0.01% of the stated TC from the certified standards. Therefore, the results from the CHN analyses are sufficient in both precision and accuracy for building a PLS model.

Prior to building the PLS model, the data block was aligned to the C emission line at 247.85 nm to remove hysteresis from the adjustable monochromator grating (two spectral regions were studied, necessitating changes in the grating position that caused hysteresis). After alignment, the data matrix was preprocessed using standard normal variate scaling, (SNV), and was baseline corrected with weighted least squares. SNV was chosen due to the fact that it is a scatter correction method often used when variation in samples is present, or when granular and/or powder samples are not delivered reproducibly [117]. SNV preprocessing is an appropriate technique in process analytical chemistry when data are collected continuously, because each spectrum in SNV is treated individually [113]. The data block and calibration block were then mean centered. Cross-validation of the model was performed using the “Venetian Blinds” approach with 9 data splits (blinds). When using venetian blinds, the total number of data points is randomized into 9 blinds or separate runs. In each run, a different block of data is left out and used to test the model produced [118]. This is an iterative process until all 9 data splits are tested in the model. Cross-validation is an effective way to test the predictive

power of the model, helping to ensure the model does not fit the data with degenerate components that will result in poor model predictions and accuracy [110].

5.5.2 Initial Regression Analysis on Portable SIBS Instrument

As mentioned previously, once the portable SIBS unit was delivered to DU, all nine soils were reanalyzed using SIBS. Then, each soil was used to create a spectral data matrix for the regression analysis by partial least squares regression (PLS). Instead of evaluating 10 subsamples and 10 replicates for each of the 8 soils, sums of 50 replicates and 7 points per soil sample, with a spectral region of 243 to 253 nm, were used. The purpose of this exercise was to ensure that the data collected with the new SIBS analyzer prototype was as good, or better than the previous data taken at PSI.

5.5.3 Incorporation of the CN (B-X) to the Development of a Multivariate Model

The inclusion of the CN (B-X) feature in the 360 nm region was also used in the PLS model. In addition, the spectral region (X-block) was truncated to the 245 to 250 nm region, and the 352 to 366 nm region, which included the spectral regions of the dominant C, Fe, and CN (B-X). A concentration matrix (Y-block) was created from TC and OC concentration values of the 8 soil samples obtained from ICP-OES and CHN analysis. Prior to building the PLS model, the data matrix was preprocessed as seen in section 5.5.1. Cross-validation of the model was performed using the “Venetian Blinds” approach with 9 data splits. The resultant model predicted both TC and OC, and IC was determined by the difference ($TC - OC = IC$) of the TC and OC prediction.

5.6 Results

5.6.1 Surrogate Soil Response Curve Results

Sections 5.6.1.1 and 5.6.1.2 report the results for the univariate analysis of C and Fe in surrogate soils prior to a more robust PLS regression analysis. In this approach, a direct correlation was determined between baseline corrected peak intensity and C and Fe concentrations.

5.6.1.1 Spectral Analysis of the 248 nm Region

Figure 5.4 includes sample spectra of Fe in clay at varying concentrations. Figure 5.5 is the response curve of iron (248.32 nm). Figure 5.6 includes sample spectra of organic, inorganic and elemental carbon at the 248 nm region. Figure 5.7 includes response curves of organic, inorganic and elemental carbon at the 248 nm region.

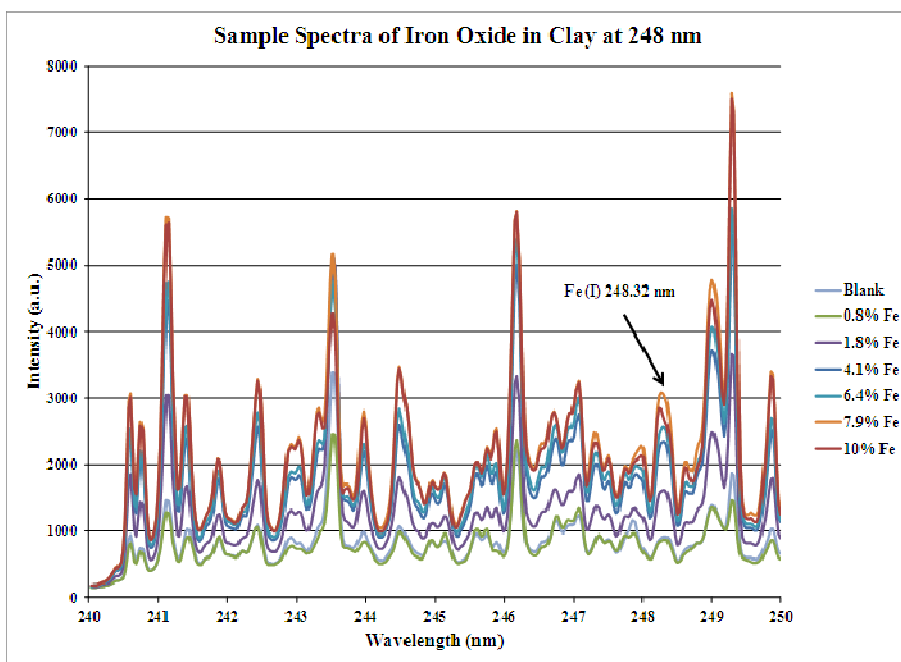


Figure 5.4 Sample spectra of iron oxide in clay from 0-10% iron. The Fe (I) 248.32 nm was used to create response curves of iron concentration vs. peak intensity. Spectral outliers were removed prior to averaging each data set.

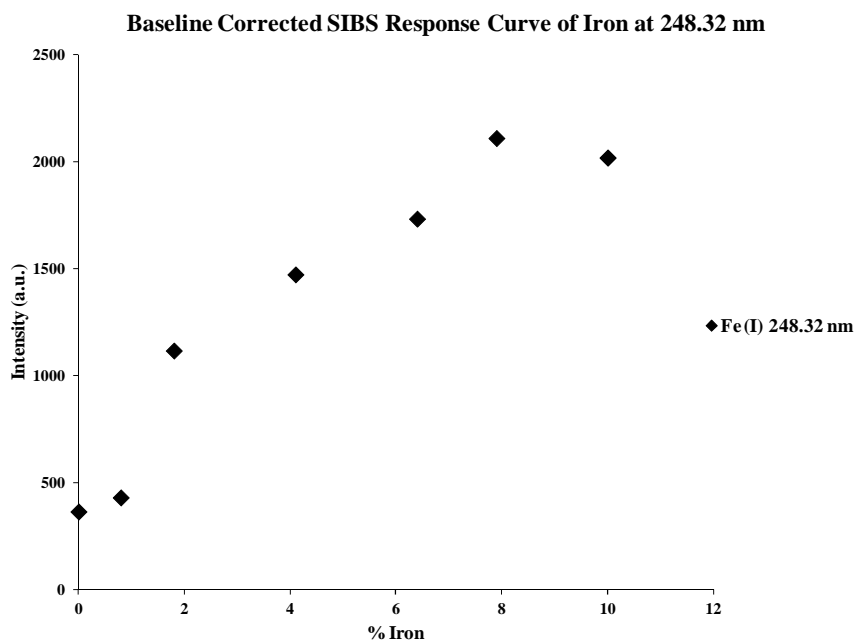


Figure 5.5 Response curve of Fe (248.32 nm) baseline corrected peak intensity; $R^2 = 0.89$.

Comparison Spectra of Organic, Inorganic and Elemental Carbon at 248 nm

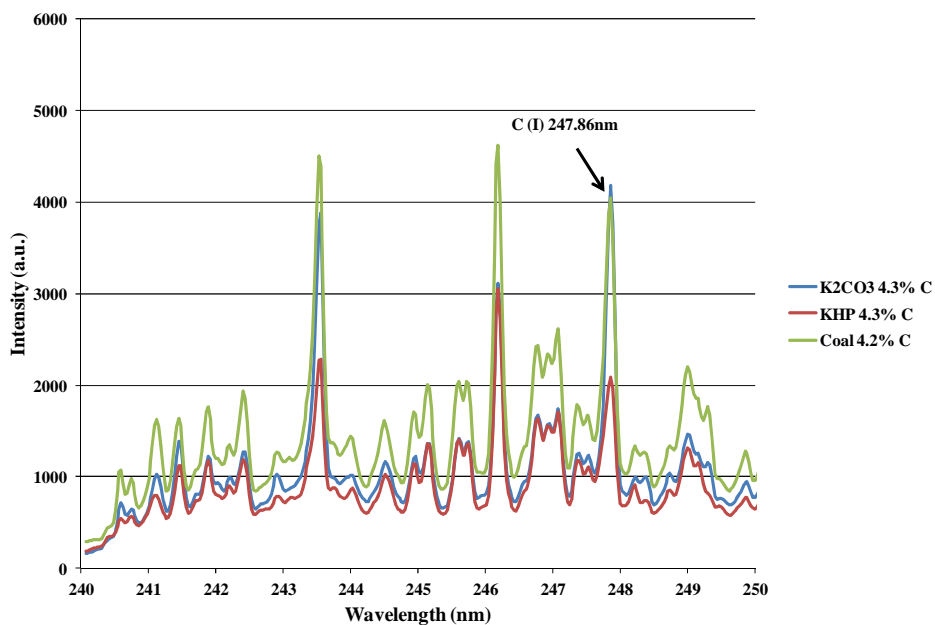


Figure 5.6 A comparison of organic, inorganic and elemental carbon at approximately 4.3% relative carbon. In each case, outliers from each sample were removed prior to averaging the spectral data.

Baseline Corrected SIBS Response Curves of Three Forms of Carbon at 247.86 nm

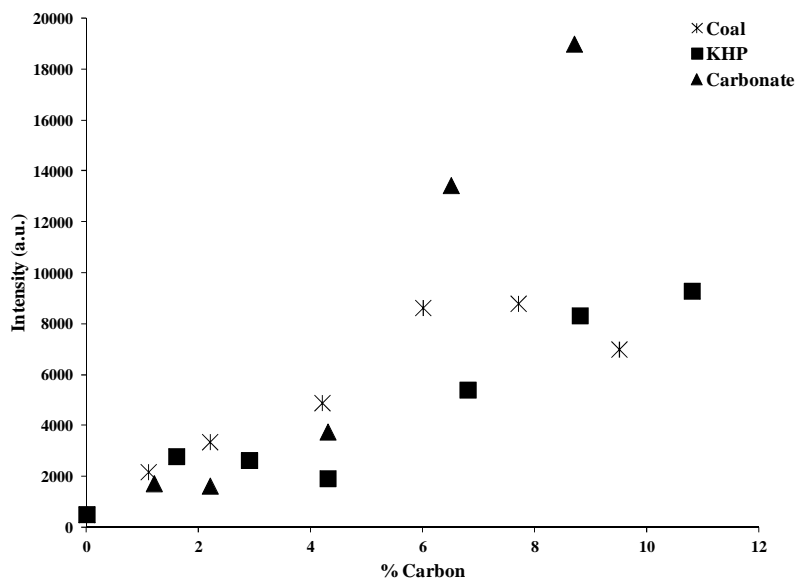


Figure 5.7 A comparison of response curves of the three forms of carbon in clay.

Results shown in Figure 5.5 show that there is a calculated correlation ($R^2 = 0.89$) between Fe concentration and peak intensity, in the 248 nm region. However, the response of the Fe line in this graph indicates that at higher concentrations, saturation of Fe occurs. Thus, a deviation at high concentrations from linearity is seen. Figure 5.7 shows that there is not a linear correlation between the three types of C and peak intensity. There are several proposed reasons for these observations. First, the current screw-feed design is not optimal for the type and density of the fine clay particles. Electrostatic interactions between the clay particles and the screw-feed system, and overall screw-feed design were not optimal for the clay samples. In addition, the density for the clay particles was approximately half of that for the soil samples, and the screw-feed delivery was optimized for the soil samples. This resulted in inconsistent flow rate and high peak intensity variability. Another reason for nonlinearity of both carbon and iron in the 248 nm region is due to self-absorption. Self-absorption occurs in the case of strongly emitting atomic lines, such as neutral iron or some calcium in soils. In the case of very high plasma density conditions, the plasma itself absorbs its own emission. This is mainly true for the resonance lines connected to the ground state, but other lines may also be affected [4]. In fact, the Fe (I) at 248.32 nm is a resonance line connected to the ground state, and has a high probability of self-absorption (Figure 5.5). As a consequence, attempting to simply correlate signal intensity to a broad range of concentration of an element becomes invalid.

5.6.1.2 Spectral Analysis of the 363 nm Region

Each of the surrogate soils was also analyzed in the 363 nm region. Figure 5.8 are sample spectra of iron in clay in this region. Response curves of iron peak intensity of four Fe (I) lines are plotted Figure 5.9, and include Fe (I) 360.88 nm, 361.87 nm, 363.14 nm and 364.78 nm.

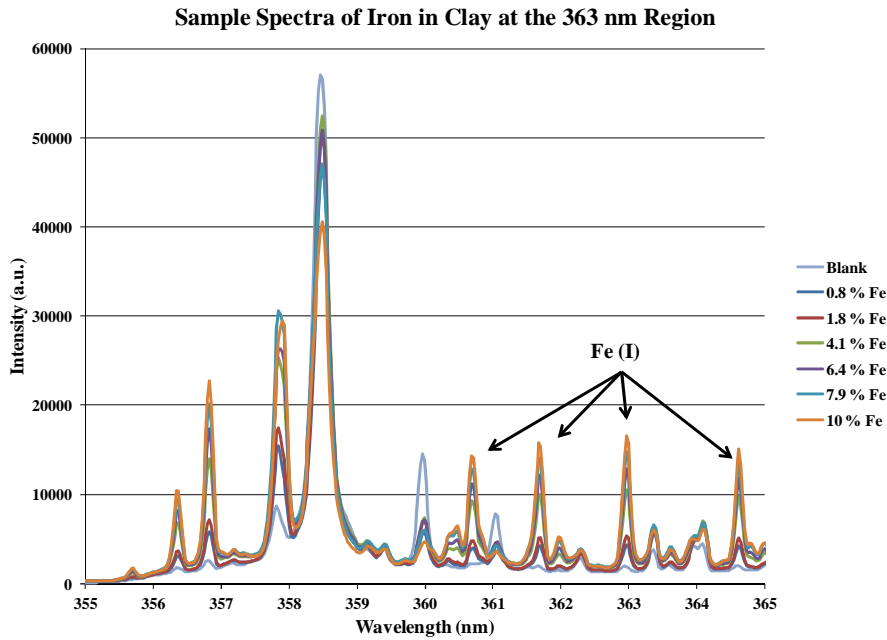


Figure 5.8 Sample spectrum of Fe in clay in the 363 nm region with Fe concentrations ranging from 0.8 to 10 %.

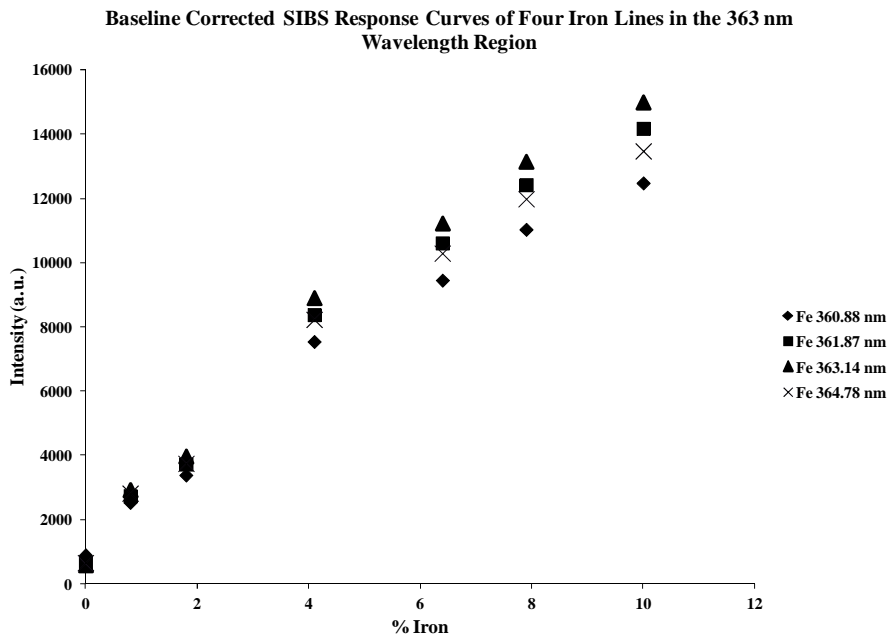


Figure 5.9 Response curves of Fe baseline corrected peak intensity for Fe (I) lines; $R^2=0.97$ for each of the four curves.

Inspection of the iron emission intensity curves in the 363 nm region, shown in Figure 5.9, indicate a linear response ($R^2 = 0.97$). This is expected due to the fact that each of the iron lines observed in this region are not resonance lines connected to the ground state. Therefore, their probability of self-absorption is low, and our results support the lack of self-absorption.

5.6.1.3 Surrogate Soil Conclusions

While the results from the surrogate soil testing have provided insight on the impact of soil composition (in the form of bulk density impacting signal intensity) and the emission response of Fe and C in both regions, the selection of the clay substrate is not a representative matrix for this work. The clay-based surrogate soils did not produce the expected linear results in the C samples. However, these results may reveal a limitation of the screw-feed design. The screw-feed configuration used during this research had been optimized for delivery of a more coarse, soil composition. Therefore, the various surrogates did not flow at a constant rate. In addition, signal nonlinearity as a function of concentration was observed with Fe lines connected to the ground state. This nonlinearity is caused by of both the inconsistent sample delivery of the clays as well as the expected saturation due to self-absorption at high concentrations. This preliminary research provided insight as to what linear range of concentrations can be quantified using SIBS for the analysis of soil. Because of the limitations seen in this research, future work would include an alternative series of matrices indentified and evaluated as

suitable matrices to study signal responses as it relates to C and Fe as well as the optimization of the soil delivery system for clays.

5.6.2 Results of Particle Size

Three soil samples (4, 7 and 8) were prepared for the study of the relationship between soil particle size and the variability of signal intensity through SIBS analysis. The intensity of the neutral carbon line at 247.86 nm was used to compare each of the three soils. Figure 5.10 is a sample spectrum of soil 4 with three different mesh sizes in the 248 nm region. Figure 5.11 (A-C) illustrate the base-line corrected carbon peak variability seen within a particular soil sample at the three different particle sizes studied. Figure 5.12 illustrates soil 4 with a particle size of 850 μm (20 mesh) with outliers removed prior to analysis. Similar results were seen with the two other soils. Outlier removal was accomplished using PCA.

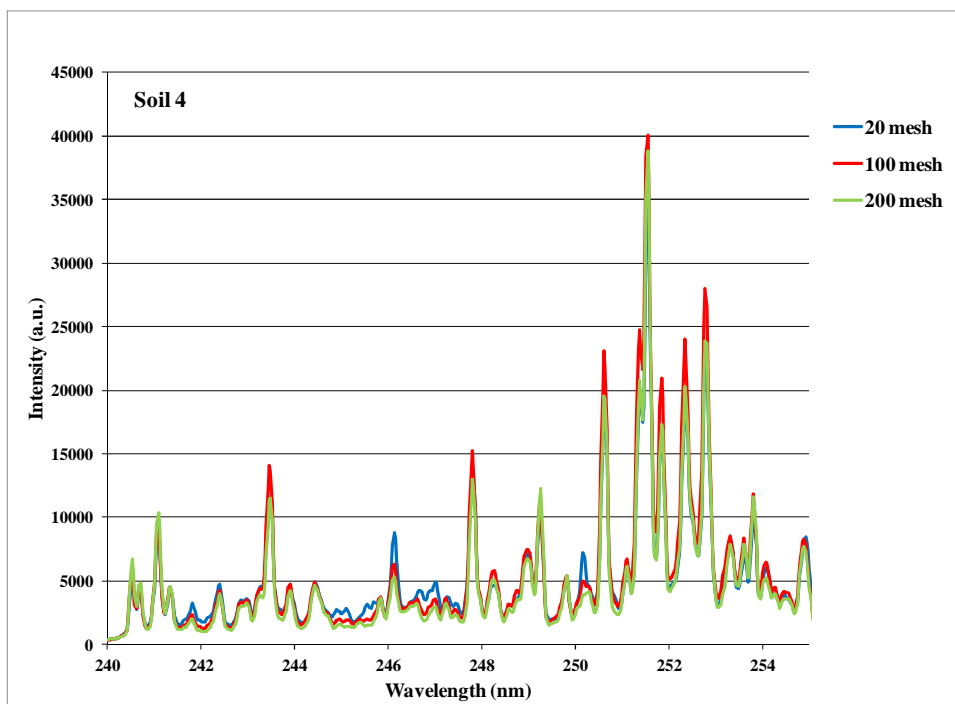


Figure 5.10 Raw (no outliers removed) averaged data of soil 4 in the 248 nm region. This graph illustrates the differences of signal intensity between the three mesh sizes.

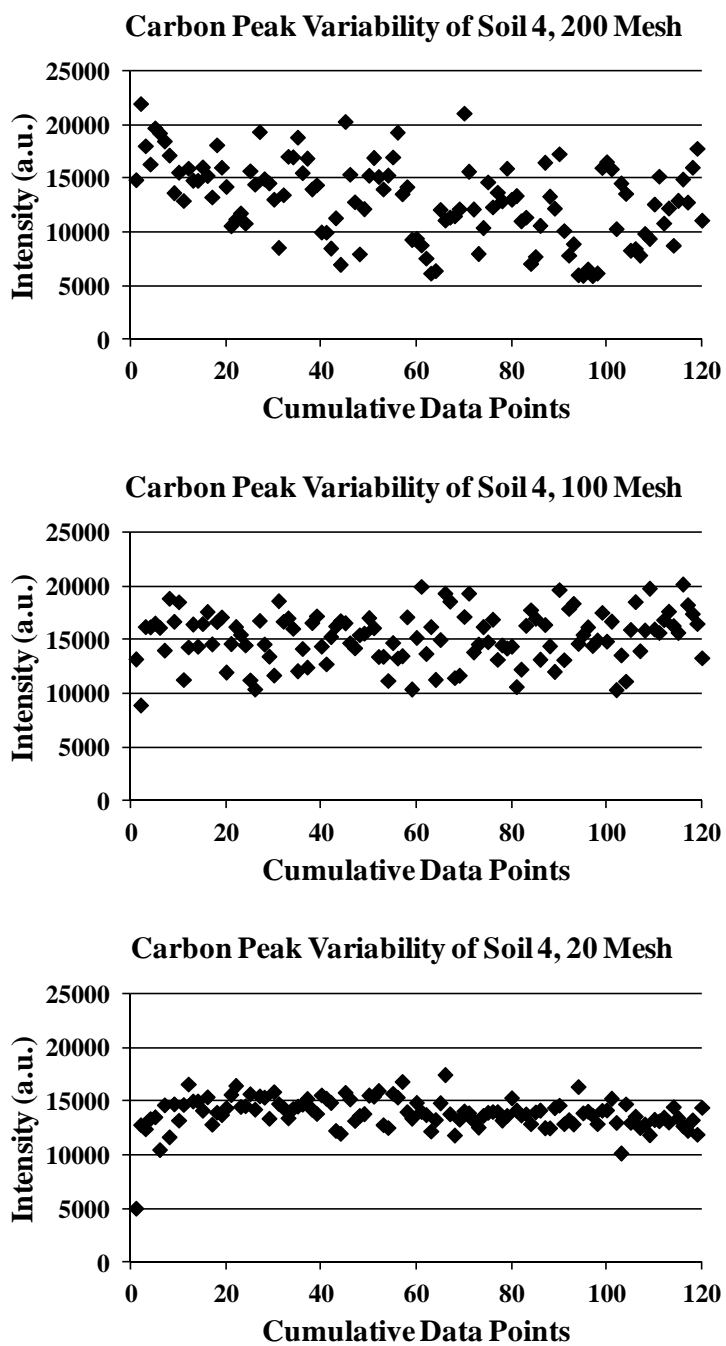


Figure 5.11 A.) 200 mesh soil 4 B.) 100 mesh soil 4 C.) 20 mesh soil 4. A-C represents total cumulative data points, with no outliers removed. As the particle size increases, the carbon peak variability decreases. The carbon peaks are base-line corrected.

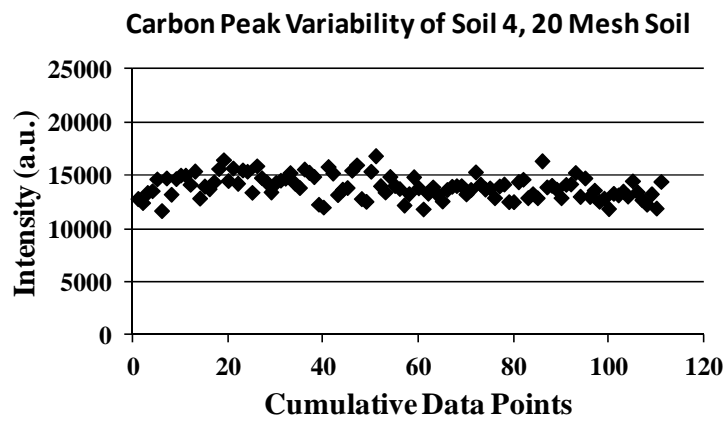


Figure 5.12 Carbon peak variability of soil 4 20 mesh with outliers removed from the data set.

Results show as the particle size decreases, the signal variability within a sample increases. Although the homogeneity of the soil samples of larger particle size decreases, there is a reduction of variability of the carbon peak intensity. One possible outcome of these results is that, in its final form, the SIBS analyzer may require less soil processing prior to analysis than a standard CHN analyzer. This also indicates a limitation of the current screw-feed design since it is evident that it does not deliver a consistent reproducible amount of soil to the spark gap within an individual soil sample. During data collection, it was observed the larger particles were delivered out of the screw-feeder into the spark gap at a more consistent rate than the smaller particles. This could be due in part by electrostatic interactions that occur between the soils and the various materials that make up the screw-feed and SIBS delivery system. The smaller particles are more susceptible to agglomeration because of the electrostatic interactions than the larger particles. Therefore, the 20 mesh samples do not interact with the screw-feed or sample delivery system as much as the smaller particles. Another possible explanation for the variation of carbon peak intensity within an individual soil sample is due to the ability of the screw to carry the soil through the screw-feed. The larger particles were picked up more easily and delivered to the spark gap. The smaller particles on the other hand, clogged the screw-feed chamber, which prevented a consistent flow of soil to the spark gap. Table 5.8 summarizes the raw average carbon peak intensity at 247.86 nm, standard deviation (STD) of the peak intensity and the relative standard deviation (RSD) for all samples. Since the 20 mesh samples had the lowest error in carbon intensity, removal of outliers from these data sets was performed in order to achieve the lowest RSD possible.

Table 5.9 indicates that by the removal of extreme outliers within a data set, RSD values of 8-16% were achieved for soils processed to 20 mesh.

Table 5.8 A comparison of the average carbon signal results of three soils with three different mesh sizes. Raw averaged data was used to determine average peak intensity, standard deviation and relative standard deviation. As the particle size increases in each sample, the relative standard deviation decreases.

Raw Averaged Data			
Soil ID	Average C Peak Intensity (a.u.)	Standard Deviation	Relative Standard Deviation
7, 200 mesh	6500.25	1847.78	0.28
7, 100 mesh	9370.01	1963.72	0.21
7, 20 mesh	8962.28	1560.36	0.17
8, 200 mesh	7663.25	1932.79	0.25
8, 100 mesh	9957.58	1524.53	0.15
8, 20 mesh	7777.92	1037.26	0.13
4, 200 mesh	13047.13	3706.78	0.28
4, 100 mesh	15238.76	2356.53	0.15
4, 20 mesh	13901.93	1490.09	0.11

Table 5.9 A comparison of the three soils of a 20 mesh particle size. Prior to averaging, all outliers were removed from the data set using PCA with a commercial software package (PLS Toolbox, Eigenvector). By removing outliers, the RSD is further decreased within each data set.

Outliers Removed			
Soil	Average C Peak Intensity (a.u.)	Standard Deviation	Relative Standard Deviation
7, 20 mesh	8890.76	1381.00	0.16
8, 20 mesh	7879.43	823.13	0.10
4, 20 mesh	13949.68	1104.03	0.08

5.6.3 Univariate Results of Soil Carbon Analysis

As previously mentioned, all 9 soils samples were analyzed at CSU in order to determine TC, IC and OC (Table 5.2). Initially, data was collected and analyzed based on CLS prior to regression analysis. This was done, in part, to understand the simplest relationship between carbon peak intensity and measured % C. Preliminary evaluation of the normalized spectral data was conducted using only the peak intensity of the carbon line. Both the OC and TC values were compared to the calculated carbon peak intensity at 247.86 nm. Figure 5.13 shows the response curve of TC compared to the baseline corrected peak intensities of the 9 soil samples. The total organic carbon values were also compared to signal intensity of the 9 soils (Figure 5.14). These results were from soil samples analyzed at PSI.

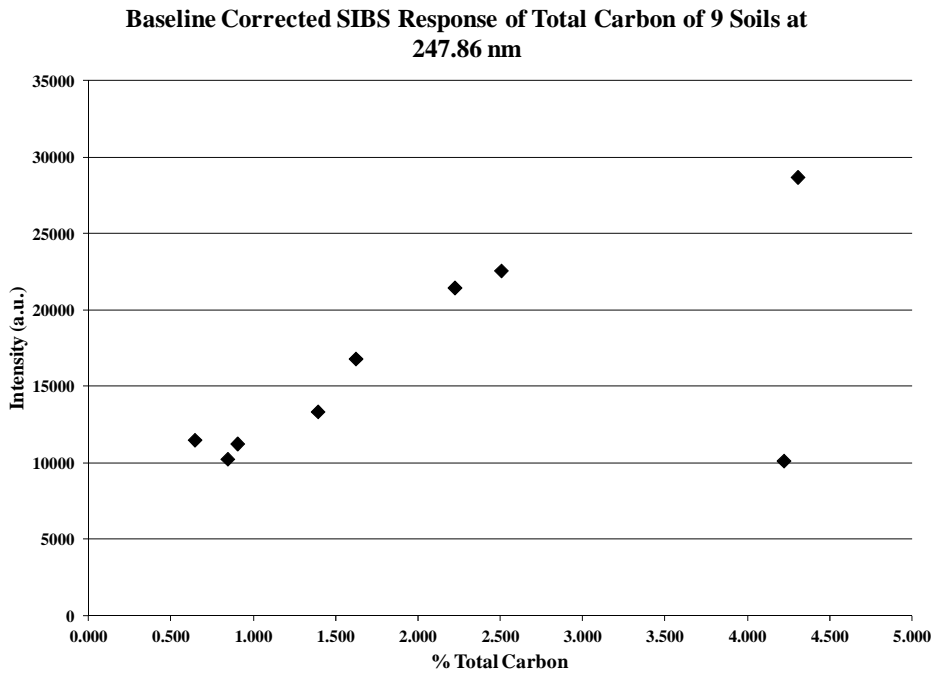


Figure 5.13 Total carbon of 9 soils compared to signal intensity.

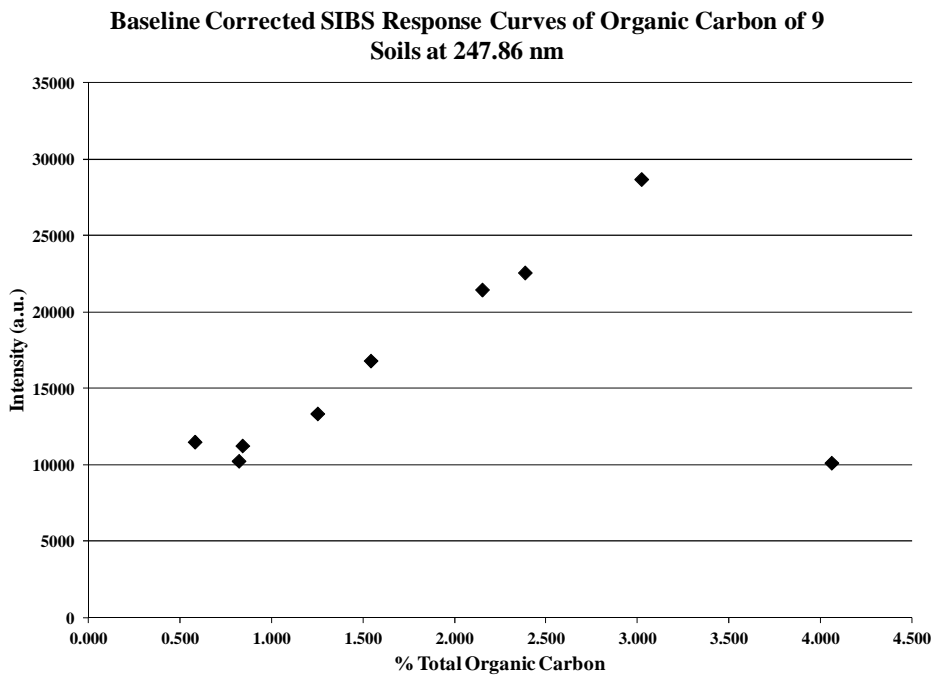


Figure 5.14 Total organic carbon of 9 soils.

In each case, the observed trend is very promising. However, in both graphs, one soil is an extreme outlier (soil 7). Based on the analytical data from CSU, it was observed that the OC value for soil 7 was higher than the TC value. In addition, close inspection of all the soil samples indicated that the overall signal intensity was significantly lower than the other eight samples, indicating a possible inconsistency in the sample delivery. Therefore, soil 7 was removed from the sample set and the data were re-evaluated. The plots of the remaining eight samples are provided in Figure 5.15 and Figure 5.16.

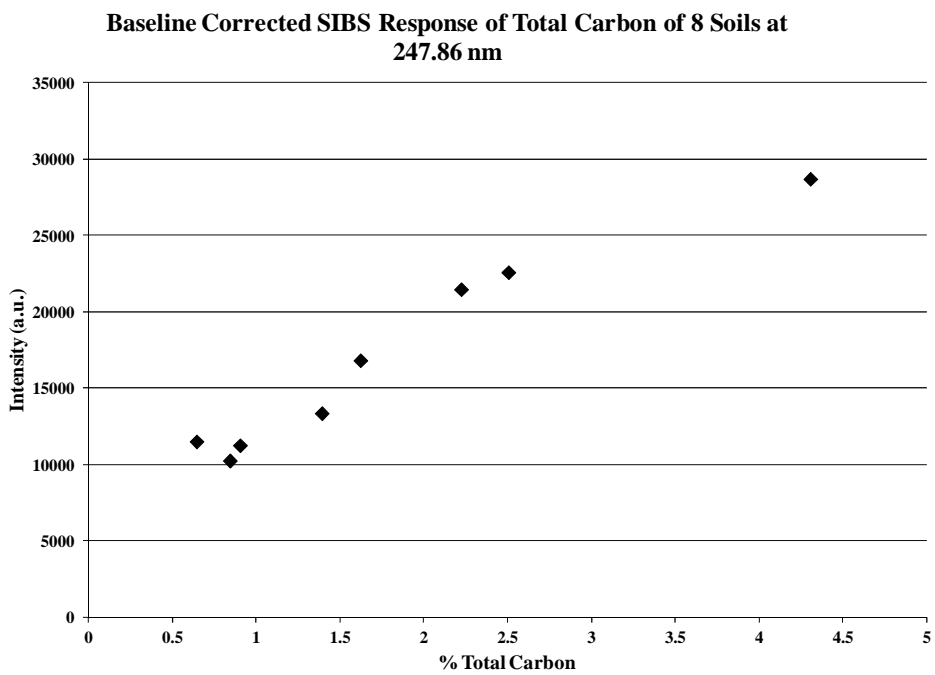


Figure 5.15 Total carbon of 8 soils, $R^2=0.94$.

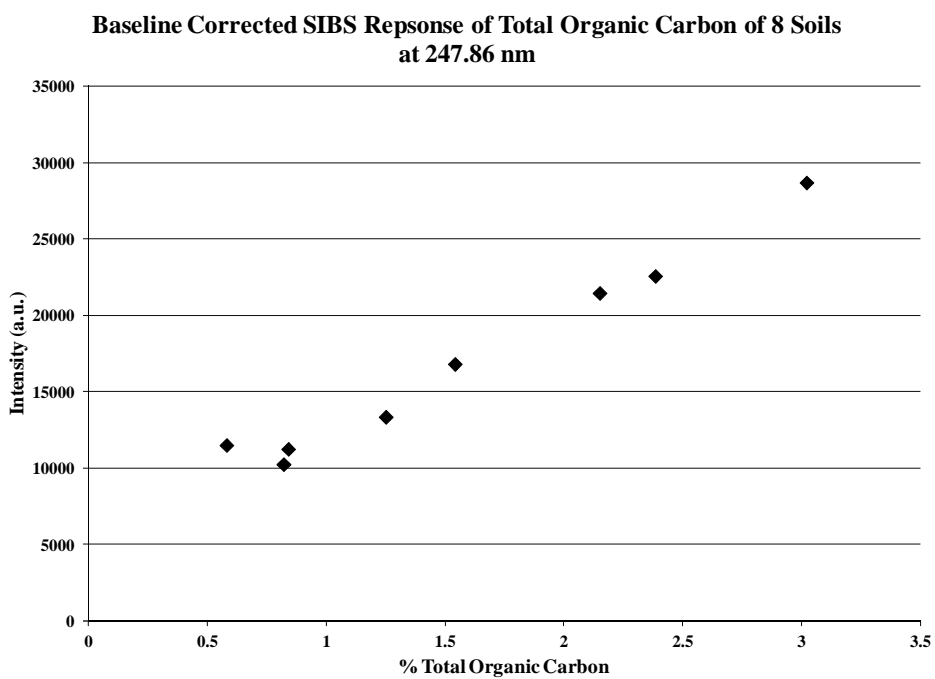


Figure 5.16 Total organic carbon of 8 soils, $R^2 = 0.97$.

After removing the soil 7 outlier from the comparison of total carbon and total organic carbon, both exhibit signs of a linear correlation over the range analyzed. However, on close inspection, Figure 5.15 indicates that the C intensity begins to saturate at approximately 4.5 % TC. This saturation is not evident when changing the x axis to reflect OC peak intensity as seen in Figure 5.16. This is due to the fact that the highest OC concentration is approximately 3%. Regardless, our first approximation of peak intensity as a function of concentration indicates good linearity. Thus, further research was conducted on the development of a robust PLS model for the prediction of C in soil.

5.6.4 Initial Multivariate Regression Analysis Results

SIBS spectra were collected on various types of soils, and a comparison was made between the measured total carbon from CHN and SIBS spectra of eight samples. Figure 5.17 shows a representative spectrum collected on soil 4 under the collection conditions specified in the 248 nm wavelength region. The intensity of the C (I) line at 247.86 nm can be clearly identified in the spectrum. Additionally, emission lines attributable to Si and Fe in the spectral region of interest are detectable in the SIBS spectra. Due to the spectral dominance of these three elements in this region, measured Fe and Si concentrations were included in the model and compared with the SIBS spectra in each of the 8 soils as potential predictors of elemental content. Figure 5.17 also indicates underlying Fe line at 247.978 nm by the shoulder on the C (I) line. However, our results indicate good correlation between measured and predicted total carbon despite the slight overlap between the C (I) and Fe lines [35].

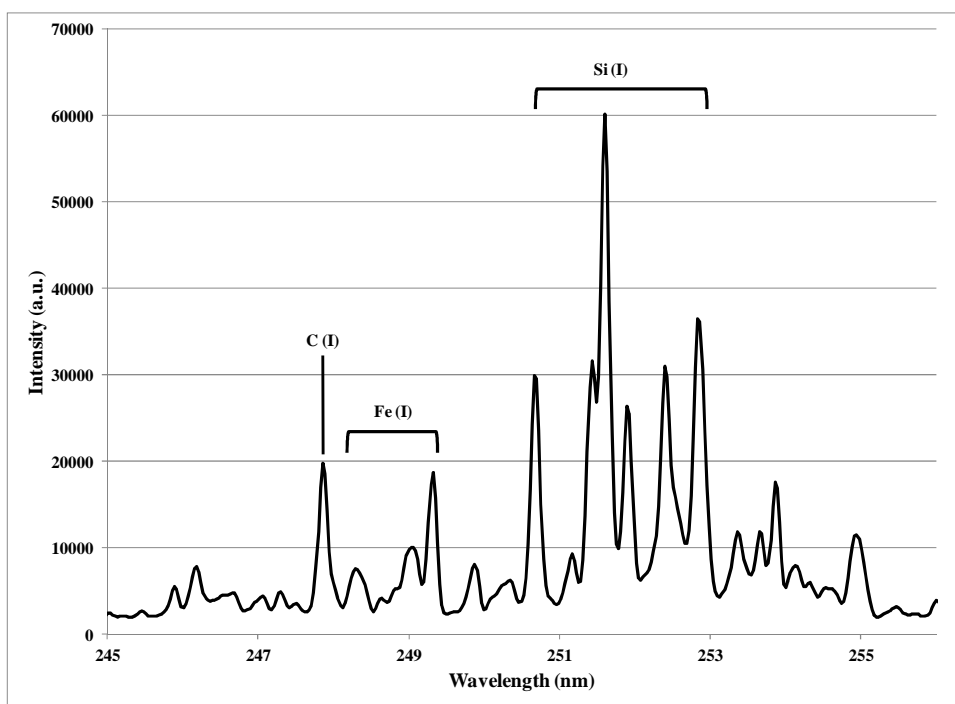


Figure 5.17 SIBS spectrum of soil 4 from 245 to 256 nm. Principal emission features in this region are C I (247.86 nm), Fe I (248 to 249 nm) and Si I (250 to 253 nm). These lines were used to evaluate the prediction models [18].

PLS was performed on the wavelength region of 243 nm to 253 nm. Figure 5.18 shows the resulting loadings plot from the first latent variable (LV1). Note that the most weighted wavelength in the spectrum corresponds to the neutral C line at 247.86 nm. Table 5.10 summarizes the results for the regression analysis for all 8 soils. Initially, only the TC values for the soils were used to build the PLS model. The resulting model with 2 latent variables (LVs) had an R^2 value of 0.945, with a root mean square error of cross-validation (RMSECV) of 0.264. Subsequent models were built using 3 LVs, which resulted in an improvement of the R^2 value (0.972) and RMSECV (0.189). Based on the initial spectral window selected, Fe and Si were dominant features in the region. Therefore, additional models were constructed to include either Fe and C, or Si and C to evaluate the impact of these additional elements on the predictive power for TC.

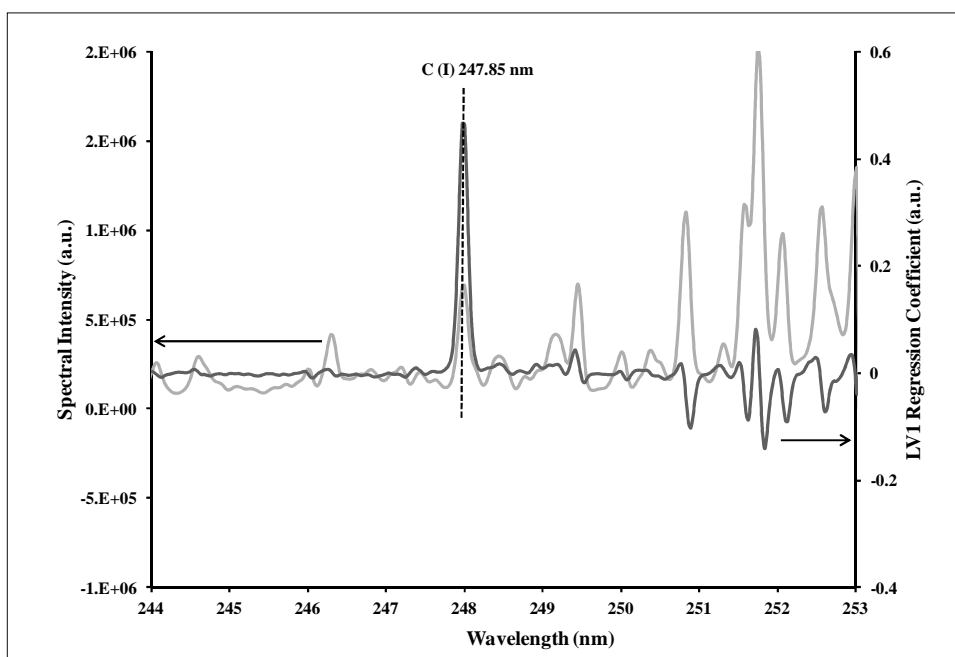


Figure 5.18 Loadings plot from the first latent variable (LV1) from SIBS, capturing 50.14% of the variance. A comparison is made between the LV1 regression coefficient and the spectral data in the 248 nm region. The most weighted wavelength in the spectrum corresponds to the neutral C line at 247.86 nm [18].

Table 5.10 Summary table of regression model which includes elements in the model, C prediction error, RMSECV when using 2 and 3 LVs. The RMSECV is reported as percent (%). Data includes the summation of 10 shots and 10 data points per soil sample [18].

Elements in Model	C Prediction Error	2 LVs	3 LVs
C	R^2	0.945	0.972
	RMSECV	0.264	0.189
C, Fe	R^2	0.922	0.968
	RMSECV	0.313	0.202
C, Si	R^2	0.925	0.970
	RMSECV	0.310	0.196
C, Fe, Si	R^2	0.909	0.967
	RMSECV	0.340	0.204

There was no improvement to the R^2 of the RMSECV values when C and Fe were used in the model. Similarly, there was also no improvement to the R^2 or RMSECV values when C and Si were used in the model, or when all three elements were included in the model (Table 5.10). A variance captured plot (Figure 5.19) shows the root mean square of error (RMSEC) and RMSECV against the number of latent variables. This plot was constructed using carbon values only, with a summation of 10 shots and 10 data points per soil sample. The variance captured plot is useful for determining the optimal number of latent variables to retain in a model that is built using the full data set. In principle, the RMSEC must always decrease as the number of latent variables retained in the model increases. However, because the RMSECV is determined from the cross-validation experiment, in which the test samples were not used to build the model that was used to test them, this value can actually increase when too many latent variables are added to the model. The optimal number of latent variables is typically the number at which the addition of another latent variable does not greatly improve the performance of the model and where there is less than a 10% difference between the RMSEC and RMSECV values [15, 119-121]. Based on this plot, a total of 5 LVs may be used without overfitting. However, a more conservative number of LVs (2 and 3) was used to predict carbon. This conservative approach was performed in response to the nature of the data used in the PLS model. Since random summed data was used to create 10 subsets of soil for each of the 8 soils, the use of latent variables that were consistent in other soil carbon analysis studies in order to avoid overfitting [15]. Figure 5.20 is a plot of the measured

vs. predicted carbon using the 8 soil samples. The resulting plot had an $R^2 = 0.97$, indicating good correlation between the predicted and measured carbon concentrations.

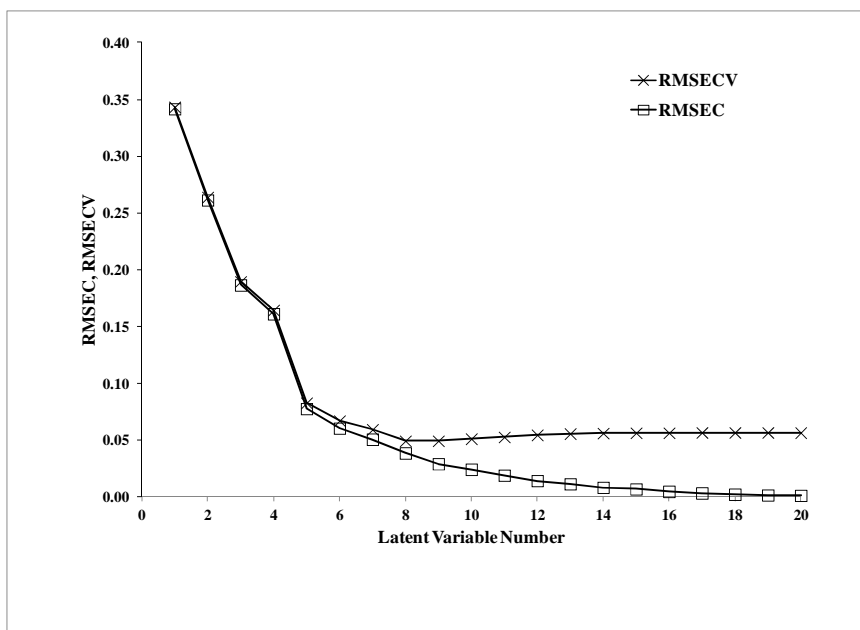


Figure 5.19 Plot of calibration error (RMSEC) and cross-validation error (RMSECV) as a function of the number of latent variables retained in the PLS model for carbon. The data set included a summation of 10 shots with 10 data points per soil sample [18].

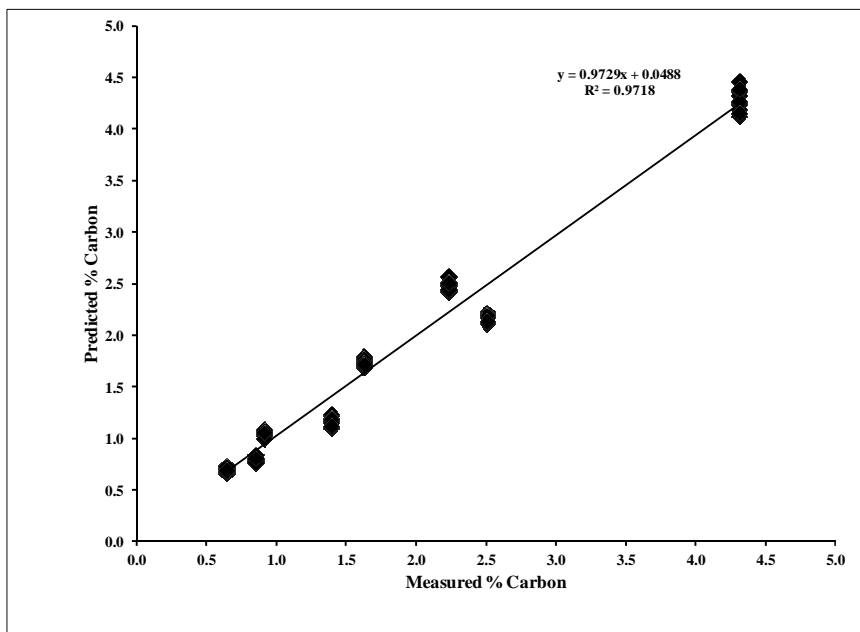


Figure 5.20 Plot of measured vs. predicted total carbon from 8 samples using SIBS. Use of Carbon only with 3 LVs, with a summation of 10 shots and 10 data points per soil sample [18].

The correlation indicates that SIBS might be a viable method to quantify carbon in soils. Eight soil samples were collected from a various locations throughout Colorado, Oklahoma and New Mexico, and gave a good representation of several different types of soils, as well as the range of TC (0.64 to 4.31%). Using a calculation of $([C]_{\text{PLS prediction}} - [C]_{\text{CHN}}) / [C]_{\text{CHN}} * 100$, we find that our accuracy ranges from 1-17% and our % RSD (calculated for each of the 8 samples) range from 1.7 to 3.5%. As noted earlier, sequestration studies have observed an increase in soil carbon that is of this same magnitude. Thus, this early work shows that SIBS will be a viable technique for monitoring sequestration. LODs are a less important metric, because the carbon content of agricultural soil is by definition high. However, we find our preliminary LOD using a PLS model created from these eight soils to be 0.08%. While this value is higher than those reported for LIBS, it is well below the value needed to quantify soil C in agricultural soils for carbon sequestration applications.

5.6.5 Replication of Regression Analysis on the Portable SIBS Instrument

One of the first objectives was to replicate the regression analysis as seen in section 5.6.4 on the portable SIBS instrument. Thus, SIBS spectra were collected on the 8 soils, and a comparison was made between the measured TC, Fe and Si from CHN and ICP-OES. Figure 5.21 shows a representative spectrum collected on soil 4. The intensity of the C (I) line can be clearly identified in the spectrum. Additionally, the Fe and Si emission lines in the spectral region of interest are detectable in the SIBS spectra. In this case, due to the increase in resolution, a better separation of the underlying Fe

lines to the C (I) line can be seen. Table 5.11 compares the results using 2 and 3 LVs from section 5.7.4 with the regression analysis from the portable SIBS analyzer. Although the number of summed data points per sample changed (from 10 to 7), the results are promising. The R^2 and RMSECV for each model improved. However, just as seen in the initial regression analysis model, the inclusion of Fe and Si did not improve the R^2 or RMSECV. This could be due, in part, to the fact that although Fe and Si do dominate the spectral region of interest, there is no correlation between the amount of C in the soil and the amount of Fe or Si. Also, self-absorption of the Fe emission lines near the C (I) line was observed in the surrogate Fe soils. Therefore, a linear correlation of Fe is potentially hindered due to the self-absorption, which in turn, might negatively impact the use of Fe in the model to predict carbon. Thus, including these elements in the model will not improve the overall prediction of C. In addition, the results show good linearity which further illustrates that there is no interference of the Fe lines with the C (I) line of interest. Finally, the overall improvement of the resolution improved our predictions.

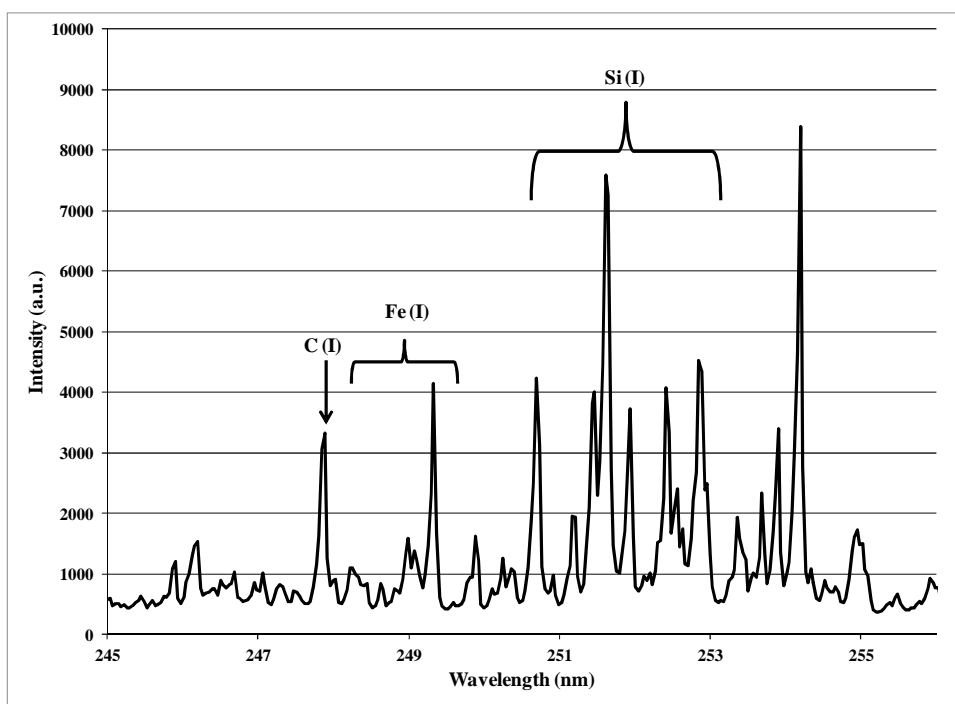


Figure 5.21 SIBS spectrum of soil 4 from 245 to 256 nm. Principal emission features in this region are C (I), Fe (I) and Si (I).

Table 5.11 A comparison of the two different SIBS instrumentation and the prediction.

Elements in Model	C Prediction Error	Data Taken At PSI		Portable SIBS Analyzer	
		2 LVs	3LVs	2 LVs	3LVs
C	R^2	0.945	0.972	0.981	0.994
	RMSECV	0.264	0.189	0.156	0.087
C, Fe	R^2	0.922	0.968	0.968	0.993
	RMSECV	0.314	0.202	0.200	0.092
C, Si	R^2	0.925	0.970	0.969	0.992
	RMSECV	0.310	0.196	0.200	0.103
C, Fe Si	R^2	0.909	0.967	0.974	0.992
	RMSECV	0.340	0.204	0.183	0.102

5.6.6 The Inclusion of TC, IC and OC

SIBS spectra were collected on the 8 soils, and a comparison was made between the measured TC, OC and IC from CSU and SIBS spectra of 8 samples. Figure 5.22 shows a representative spectrum collected on soil 4 in the 350 to 370 nm wavelength region. This figure identifies the 358 to 359 nm wavelength region used to evaluate the prediction models, and Table 5.12 illustrates the CN vibrational bands found in the UV wavelength region. Recall that Figure 5.21 represents a sample spectrum of soil 4 in the 248 nm spectral region collected from the portable SIBS analyzer. PLS was performed on the 245 to 250 nm region and the 352 to 366 nm region. As described in 5.6.4, the results indicated good correlation between measured carbon and predicted carbon despite the slight overlap between the C (I) and the Fe lines. In addition, the resolution is significantly improved due to the new spectrometers and separation of signals in the 248 nm region, which also may be a reason for the good correlation. Table 5.13 summarizes the results for the regression analysis for all 8 soils for the prediction of TC, IC and OC. Table 5.14 illustrates the resulting model with both 3 LVs and 4 LVs. Using 3 LVs, the resulting model had an R^2 value of approximately 0.97 for TC and OC, a RMSECV of 0.126 (OC) and 0.163 (TC), with a RMSEC of 0.128 (OC) and 0.165 (TC). Using 4 LVs, the resulting model had an R^2 value of approximately 0.99 for TC and OC, a RMSEC of 0.081 (OC) and 0.102 (TC), with a RMSECV of 0.083 (OC) and 0.104 (TC). Due to the fact that no improvement was seen when Fe and Si were included in the previous models, they were excluded from any further regression analysis. It is important to note that Table 5.13 also includes the relative error for each prediction. Although in

some cases, the difference between the actual and predicted values was small, the relative error is still rather large. This information gives good insight on how small changes in the prediction correlate to rather large relative error. For example, the samples with low C concentration have the largest relative error. This provides a preliminary sense of the detection limits of the instrumentation. In addition, the relative error for most of the IC predictions is high, indicating that the current method of determining IC by difference may not be the best approach.

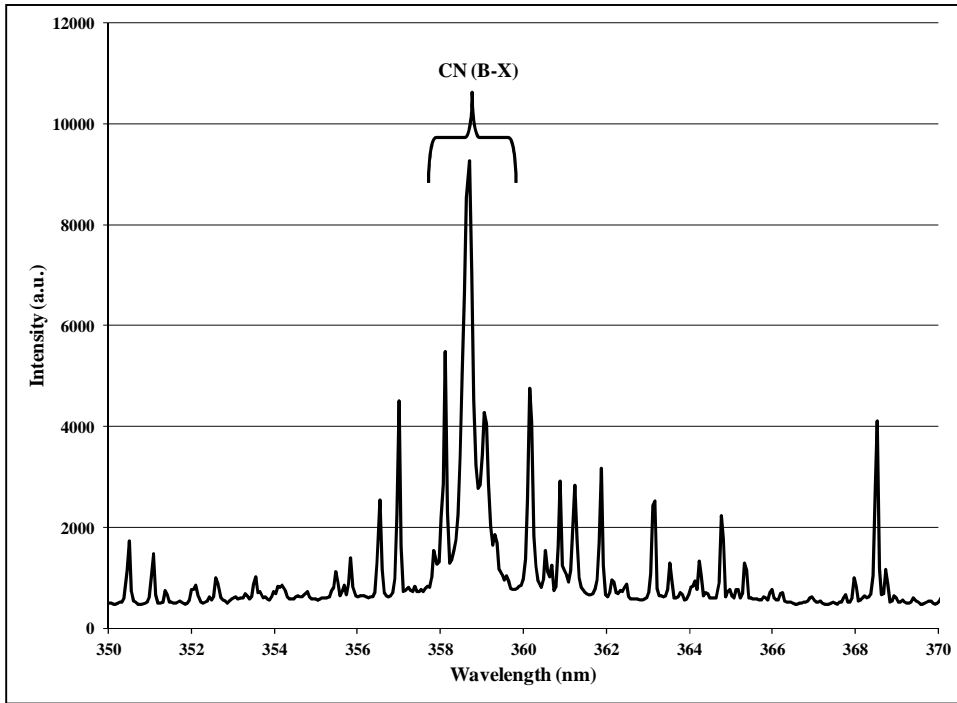


Figure 5.22 SIBS spectrum of soil 4 from 350 to 370 nm. The principal emission feature in this region is the CN (B-X) in the 358 to 359 nm region. The region of 352 to 366 nm was used to evaluate the prediction models.

Table 5.12 Peak wavelengths of the molecular bands of the CN emission lines found in the UV spectral region. The (1-0), (2-1) and (3-2) vibrational bands were used to evaluate the prediction models [122].

Molecular Species	Vibrational Band	Wavelength (nm)	Excitation Energy (eV)	Electronic Transition
CN System	(0-0)	388.34	3.2	$B^2\Sigma^+ \rightarrow X^2\Sigma^+$
	(1-1)	387.14		
	(2-2)	386.19		
	(3-3)	385.47		
	(4-4)	385.09		
	(1-0)	359.04		
	(2-1)	358.59		
	(3-2)	358.39		

Table 5.13 Prediction results using 3LVs of TC, OC and IC. IC was determined by the difference between the prediction of TC and OC.

Sample ID	3LVs								
	-----%-----			Prediction			Relative Error		
	OC	TC	IC	OC	TC	IC	OC	TC	IC
1	1.54	1.62	0.08	1.48	1.56	0.07	3.74	3.89	6.73
2	3.02	4.31	1.29	2.99	4.26	1.27	1.11	1.09	1.04
3	1.25	1.39	0.14	1.40	1.61	0.20	12.35	15.61	44.56
4	2.38	2.50	0.12	2.38	2.50	0.13	0.29	0.02	6.13
5	2.15	2.22	0.07	2.06	2.09	0.03	4.31	6.13	60.25
6	0.58	0.64	0.06	0.36	0.36	0.00	37.49	43.96	102.96
8	0.82	0.85	0.03	0.96	1.02	0.06	16.97	20.29	120.28
9	0.84	0.90	0.06	0.96	1.04	0.09	13.73	15.53	39.49

Table 5.14 TC and OC RMSEC and RMSECV values for both 3 and 4LVs. The R² values are also listed. The error is associated with each PLS model.

OC Prediction					
3LVs			4LVs		
RMSEC	RMSECV	R ²	RMSEC	RMSECV	R ²
0.126	0.128	0.975	0.081	0.084	0.989
TC Prediction					
3LVs			4LVs		
RMSEC	RMSECV	R ²	RMSEC	RMSECV	R ²
0.163	0.165	0.979	0.102	0.104	0.991

5.7 Chapter Conclusions and Future Work

To accurately determine small changes in soil C and consequently monitor soil carbon sequestration, an accurate, robust, and portable instrument must be developed. SIBS is a promising and potentially field-deployable instrument for the measurement of C in soil. During this phase, several surrogate soils were developed in order to study signal response of C (organic, inorganic and elemental) and Fe as a function of concentration. These results provided information on the limitations of the current screw-feed design, as well as the linear range of C and Fe. In addition, several soils were collected and characterized for TC, OC and IC. Three soils were used to study the effects of particle size on signal reproducibility. It was determined that the particle size does play a role in the shot-to-shot variability and reproducibility. During this phase, PLS analysis of a limited data set results in producing a good correlation between the predicted and measured carbon concentrations ($R^2 = 0.93$) without the inclusion of Fe and Si in the model.

A portable SIBS analyzer was built at PSI, and tested using a small sample set of soils. This limited data set resulted in producing a good correlation between the predicted and measured carbon concentrations ($R^2 = 0.98$). There was an overall improvement in the predictions seen in the portable analyzer when compared to the initial data collected at PSI. Furthermore, the 350 nm to 400 nm spectral region containing the CN (B-X) molecular feature was included to predict the fraction of organic carbon. As a result, the fraction of inorganic carbon was also predicted in a model. This preliminary

model of TC, IC and OC demonstrate that it may be possible to predict these fractions of soil using SIBS instrumentation.

Future work will include testing a large soil data set in order to expand and validate the current preliminary model. These soils will have a broad range of TC in order to better characterize the values of the accuracy, precision, LOD and LOQ of the instrument. In total, 100 well-characterized soil samples will be tested to validate an improved SIBS instrument prototype. The continuation of the evaluation of spectral windows to discriminate signals related to the presence of organic carbon from inorganic carbon will be performed. In doing so, a more robust model to predict carbon in soil samples will be constructed. Furthermore, the validation of the model will be performed using a portable SIBS soil analyzer prototype.

Chapter 6 : Preliminary Correlations of Feature Strength in SIBS of Bioaerosols

This chapter outlines the preliminary studies using SIBS as a possible future detection method for bioaerosols. The majority of research and text in this chapter was peer reviewed and published in 2010².

6.1 Introduction

Bacterial identification has long been an interest for many fields of science including microbiology, medicine, health care and military and civilian governmental organizations. For example, rapid detection and identification of harmful aerosols such as *Bacillus anthracis* (anthrax) are critical objectives of both military and civilian entities [123]. The use of Sarin gas in the 1995 Tokyo subway attack and the distribution of Anthrax spores through the U.S. Postal Service in 2001 are two examples that demonstrate the need for chemical and biological warfare agent sensors [124]. However, rapidly detecting and distinguishing between hazardous and nonhazardous bacteria is no easy task. Several optical systems have been developed in recent years in order to identify bacteria in the aerosol form. Most of these systems rely on fluorescence to distinguish between bioaerosols from non-bioaerosols [125-127]. In general, these instruments can run continuously and in real time to trigger and provide a warning for the

² Schmidt, M.S. and A.J.R. Bauer, *Preliminary correlations of feature strength in spark-induced breakdown spectroscopy of bioaerosols with concentrations measured in laboratory analyses*. Applied Optics, 2010. **49**(13): p. C101-C109

existence of potentially life threatening bioaerosol particles. One limitation in using fluorescence as a detection method is the fact that there are frequent false alarms. The UV-visible fluorescence systems are incapable of distinguishing or identifying between types of harmful or harmless micro-organisms. In addition, this type of system cannot determine the difference between molecules with similar fluorescence peaks, such as polycyclic aromatic hydrocarbons or [123].

Current biochemical techniques such as polymerase chain reaction (PCR) can be used to identify the genus and species of bacteria [128-130]. However, PCR and DNA sequencing methods require time. Although these methods are very specific, they do not provide real-time measurements required for fast action. In recent years, there has been several research efforts focused primarily on laser-based detection and identification of bacteria. Specifically, LIBS has been applied as a spectroscopic method of determining hazardous bioaerosols in air. A number of groups have demonstrated the ability of LIBS for chemical and biological detection as simulants and bioaerosols [10, 40, 131, 132]. The use of both nanosecond and femtosecond pulse width lasers have been used to produce the LIBS plasma [46, 133]. However, the use of LIBS as a detection method of bioaerosols is still a relatively immature technique, and the instrumentation is expensive.

This chapter focuses on the first fundamental studies conducted to compare the signal output of bioaerosols with SIBS with the optical collection placement. This chapter also focuses on both elemental and molecular features acquired in SIBS analysis, and the preliminary results of SIBS signals compared to laboratory elemental analysis

with proton-induced x-ray emission (PIXE) and combustion analysis for carbon, hydrogen and nitrogen (2400 Perkin-Elmer CHN Analyzer).

6.2 Bioaerosol Generation and Instrument Design

Aqueous droplets containing bacteria and spores were generated by feeding a suspension of sample material through a polydisperse atomizer nozzle (Sono-tek, Milton, NY). The operating principles of the nozzles employ high frequency waves. Disc-shaped ceramic piezoelectric transducers convert electrical energy into mechanical energy. The signal is amplified at the atomizing surface by two titanium cylinders. The nozzles are configured so that the excitation of the piezoelectric crystals creates a transverse standing wave along the length of the nozzle [134]. This frequency vibration is coupled into the fluid, which generates polydisperse aerosols. The size of the droplet is a function of the frequency and fluid flow rate through the nozzle orifice

$$D_p = \left(\frac{6Q}{\pi f} \right)^{1/3} \quad \text{Equation 6.1}$$

where Q is the fluid flow and f is the frequency. In the case of the Sono-tek unit, it generates droplets with an average output particle diameter of 18 μm . Aerosols generated in this way have been previously characterized with a TSI Aerodynamic Particle Sizer prior to spark analysis [16].

The droplet generator was situated at the top of a Plexiglas tube in a downward-directed orientation toward the drying column. During this process, these droplets were

entrained in air, and fall through a heated column (Figure 6.1). The air in the column was heated to 110°C to remove water from the particle droplets. The particles dry during the traverse and are delivered to the spark gap through a pumping system. The spark gap occurs between two rod-shaped electrodes that are placed approximately 3.5 mm apart and are placed at the centerline of the collection optics. Once the particles fall through the spark gap, they are collected on the bottom of a Plexiglas extension under the drying column that houses the spark gap. This filter prevents particles from exiting the generator and contaminating the air pump. These analyses demonstrated that under low density conditions described here, dry aerosol is formed of individual particles and that very few are presented in agglomerated form.

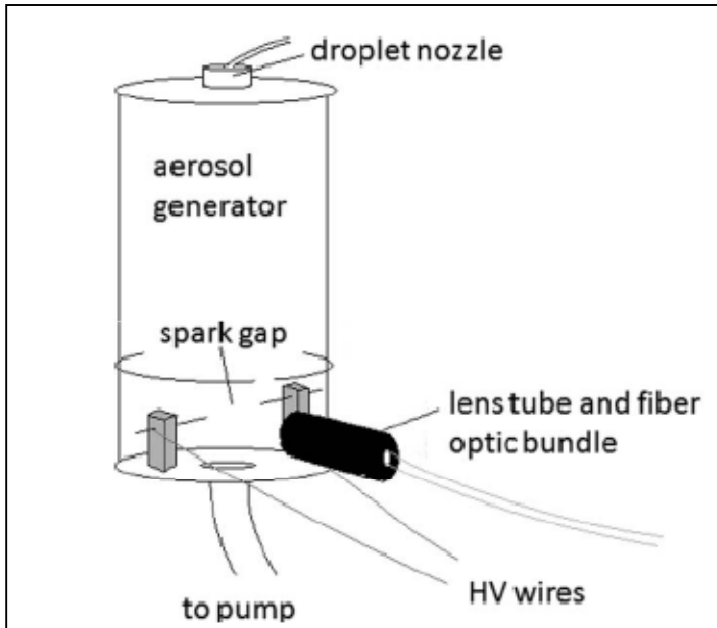


Figure 6.1 Drawing of spark gap and lens tube section interfaced to an aerosol generator that produces the sample described in the text. Air is pumped through the porous cylinder that forms the generator and dries and delivers the particles produced by the nebulizer to the spark gap [17].

The electrodes were mounted within the sampling assembly house, which also had a quartz window to pass the spark emission to optical fibers. This window was sealed to prevent any escape of the bioaerosols while allowing for the collection of the spark emission. As the particles were presented to the spark gap, the power supply was energized and 700 mJ sparks were generated at a rate of 1 Hz, while the aerosolized samples continued to flow through the gap at atmospheric pressure. The sparks produced at this power were cylindrical, and each spark typically processed many particles. The spark is a two-step phenomenon in which an initial arc event (high voltage and low current) occurs to reduce the electrical resistance of the air in the electrode gap before a capacitor bank discharges across the spark gap. Full discharge of the spark circuitry has a time constant of about 8–10 μ s, during which time the plasma is formed and the sample ablated. As the particles were processed by the spark, light from both atomic and molecular emission was focused into an optical fiber and transmitted to a 1/4 m spectrometer with a 1200 lines/mm grating and then to an Andor iStar ICCD. This instrumentation describes the general design for the SIBS bioaerosol analyzer. Further details will be described in the next section that deals with the focused optical position in relation to the electrodes.

6.3 Preliminary Electrode Position Correlations

The purposes of early experiments were to better characterize aspects of the plasma by varying the electrode placement relative to the optical collection in the apparatus in the presence of various sample types. This is necessary because the plasma is not homogenous. Therefore, temperature and ablative processing rates differ by location within the spark gap. Another purpose of these experiments was to identify and optimize atomic emission lines such as calcium, and molecular features such as CN (B-X) signals associated with *Bacillus thuringiensis* (Bt). Plasma shape changes as a function of time, and there are large temperature differences within the plasma which can be observed by changing the electrode position. A single bacteria sample, Bt, was used to correlate spectral intensity with respect to the electrode position. Bt aerosols were studied in the spectral regions around 279 nm and 380 nm. Specifically, calcium lines were studied to determine differences in signal behavior at the various electrode positions. Aerosolized DI water and electrode material alone were also studied as background. The electrodes were originally placed so that the focus of the optics covered the energized side (hot electrode) of the gap. The gap was then translated to allow optical probing of the center of the plasma. Finally, the gap was moved further until the emission at the ground side of the gap was in view of the collection optics. Figure 6.2 illustrates the SIBS design that houses the electrodes. During this experiment, the electrode position was translated in order to capture the spark emission at different focal points.

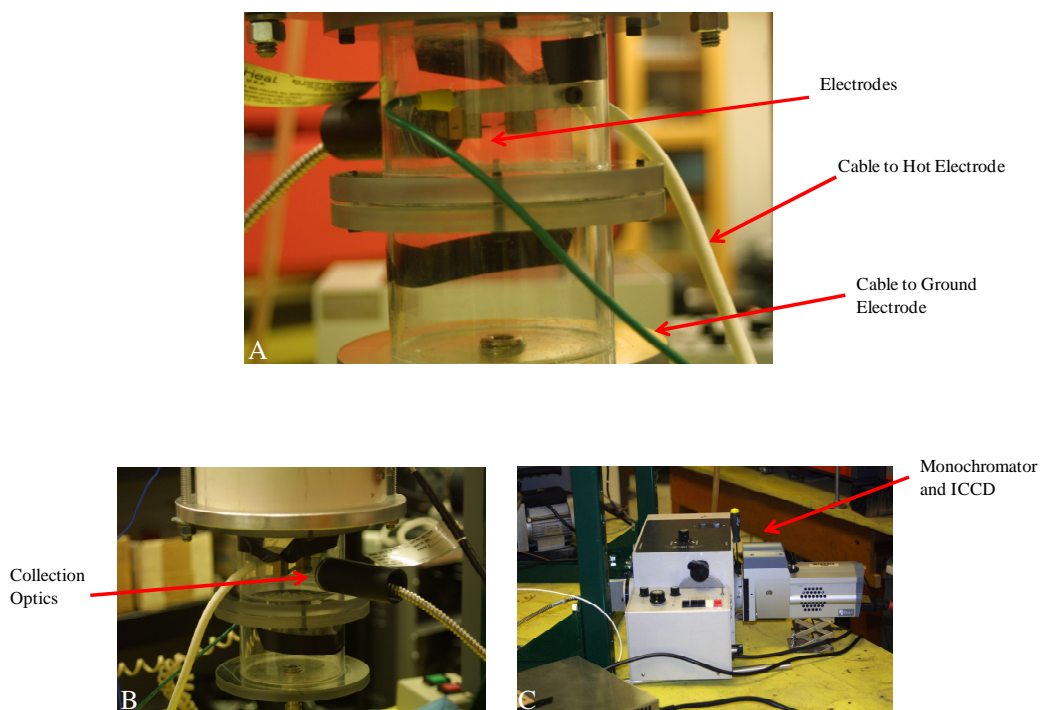


Figure 6.2 Photographs of the SIBS design. A). Close-up of the electrodes and the optical translation. B). Photograph the collection optics. C). The $\frac{1}{4}$ m monochromator coupled with the ICCD detector.

6.4 SIBS of Bioaerosol Samples

The following sections describe the three biological samples used to correlate feature strengths of SIBS with laboratory determined elemental composition. These samples were used as simulants for hazardous bioaerosols. In addition, specific details for this experiment are described in the appropriate sections.

6.4.1 Biological Simulants

Three biological samples were used as simulants for hazardous bioaerosols: *Bacillus thuringiensis* (Bt), Ragweed pollen (Rw), and Johnson grass smut (smut). Bt was obtained from Certis USA, (Javelin WG Tech Grade). Well-characterized ragweed and smut powdered samples were purchased from Thermo Scientific Particle Products. Bt particles have an average aerodynamic diameter of about 1.5 μm [36]. With an input suspension of 77mg in 100 mL of water, there are 4.6×10^5 particles/cm³ of air in the sample stream delivered to the analytical region. The spark gap is 3.5 mm wide, and the sparks appear to be about 1 mm in thickness. Given these dimensions, there are about 400 particles of Bt present in the spark gap at the time of each analytical spark. Johnson grass smut particles have an aerodynamic diameter of 8 μm [37]. Given the same concentration of aqueous suspension, there are about 3 particles of smut fungus in the gap for each analysis. Lastly, ragweed pollen has a reported aerodynamic diameter of about 20 μm , which statistically yields 1 particle per 6 sparks [37]. All samples are assumed to have the same mass present in the spark gap, 0.7 μg of particles, for each spark analysis.

In this system, the electrode tips are not protected from sample particle impact. Particles tend to settle on the electrodes, and it is likely that at the low repetition rate of the current work (1 Hz) there is a signal contribution from the sample material that accumulates between pulses on the electrodes. This will affect an actual system for the monitoring of hazardous bioaerosols more than the experiment described here, as the delivered mass per time is held steady and material buildup on the electrodes remains consistent for all three sample types.

6.4.2 Data Acquisition of Three Bioaerosols

Spectra of the three biological aerosols were collected in windows about 40 nm wide. The data acquisition delay times of the collected spectra were varied from 1 μ s to 30 μ s, with a gate width of 1 μ s. Data for 50 sparks were acquired at each delay time. Spectra were acquired in two principal wavelength windows to observe both atomic and molecular features of interest. Spectral windows were acquired of all samples with the central wavelength of the spectrometer system held at 300 nm and 366 nm. The biological samples were compared to background spectra of a filtered air flow containing relative humidity matched to that of the sample flow containing the bioaerosol.

6.5 Results

The following sections outline the results found from both the electrode position study as well as the spectral correlation between elemental compositions of the three biological samples as measured by combustion and PIXE analysis.

6.5.1 Electrode Position Results

The purpose of the electrode experiments was to better characterize aspects of the plasma by varying the electrode placement relative to the location of the probed volume in the apparatus in the presence of Bt. Plasma shape changes as a function of time and focal point. There are large temperature differences within the plasma, which can be observed by changing the electrode position. The electrode placement experiment indicated that by focusing the optics on the hot electrode, the full time profile of the peak intensity of the sample can be observed. Figure 6.3 shows the time profile of calcium II at the hot electrode compared to signals related to electrodes only and water. By observing the full time profile of calcium II, it appears that the maximum peak intensity occurs at 4 μ s. Figure 6.4 shows the time profile of calcium II at the ground electrode, which does not give a full time profile of the peak intensity. This experiment also confirmed spectral differences between the hot and ground electrode position. Figure 6.5 illustrates high-resolution data collected with optimized instrumentation configuration. Figure 6.5 shows spectral data in the 365 nm to 405 nm region, which depicts Ca II, N II, O II and CH (A-X) atomic and molecular features. This spectrum is representative of Bt with 81mg/100mL aerosol sample with the optics focused on the hot electrode. In addition, by focusing the data collections on the hot electrode, molecular features are observed where as these features were not observed while focusing on the ground electrode. Thus, all data were collected in the following sections while focusing on the hot electrode.

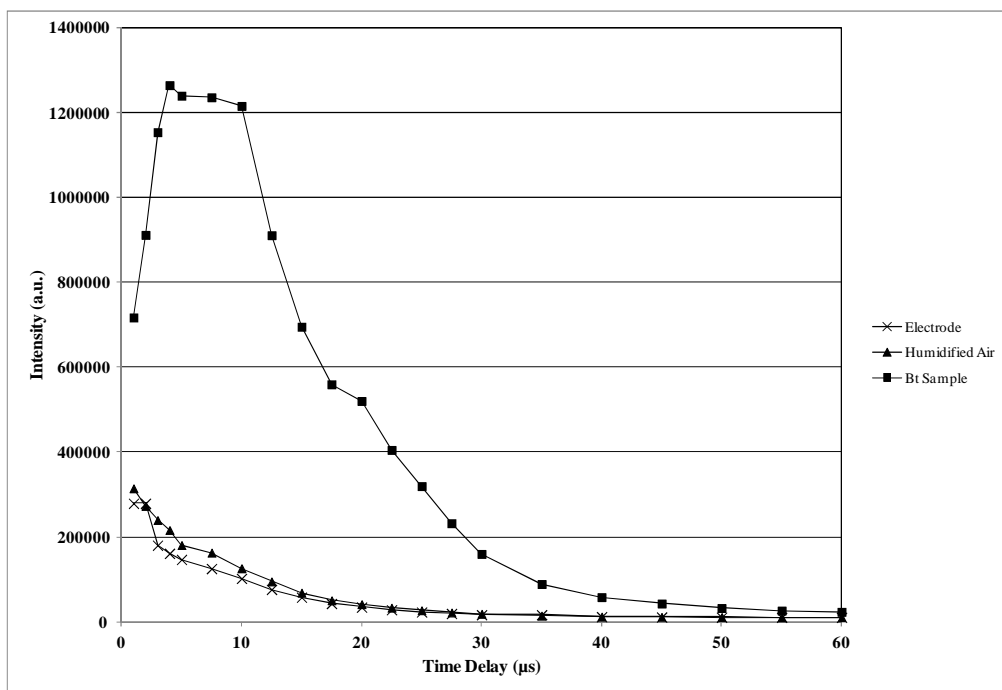


Figure 6.3 Time profile of calcium II (393.36 nm) focused at hot electrode.

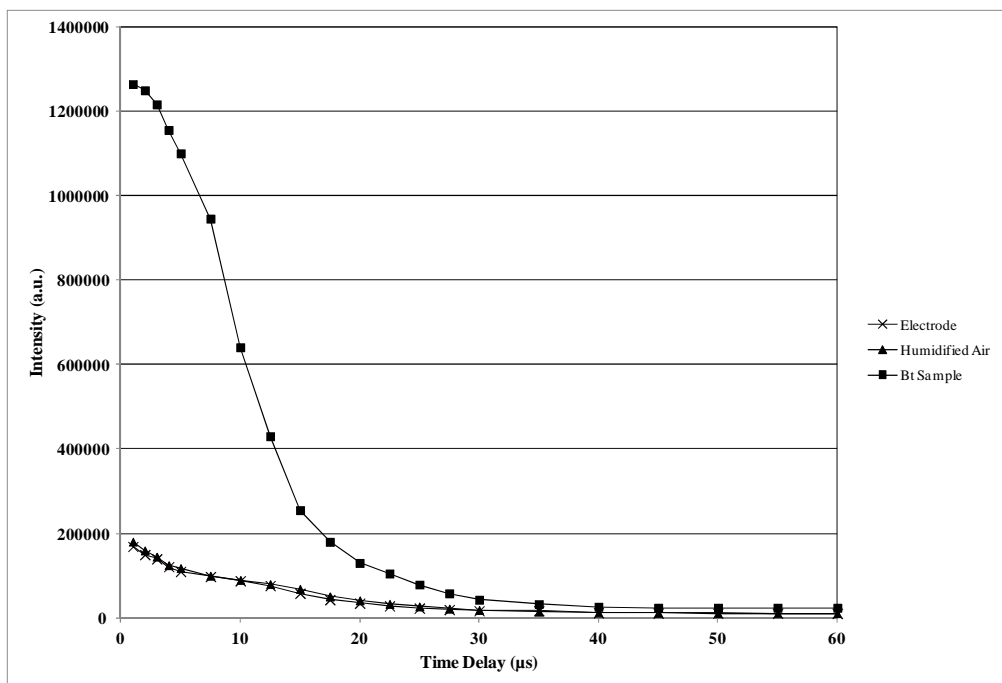


Figure 6.4 Time profile of calcium II (393.36 nm) focused at ground electrode.

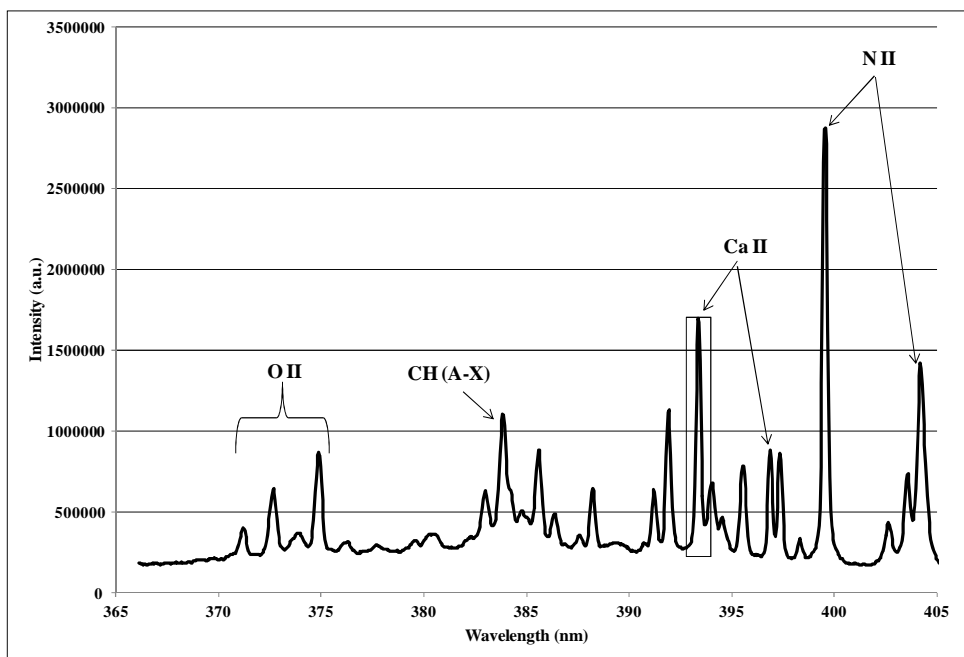


Figure 6.5 Bt 81 mg/100mL from 365-405 nm. Focused on hot electrode, and the Ca line at 393.36 nm is highlighted.

6.5.2 Elemental Composition Results

The major elements present in the three powdered biological samples are presented in Figure 6.6. Carbon, nitrogen, and hydrogen amounts were acquired with combustion analyses. Minor elements were acquired with PIXE and are shown in Figure 6.7. Concentration of oxygen was calculated in a mass balance from the other results. This information was used to create response curves. The carbon, nitrogen, and hydrogen concentrations of the samples vary widely, as do the trace elements. These preliminary data indicate that elemental composition may be useful in the classification of bioaerosol material, even though the sample set is not large enough to be statistically significant.

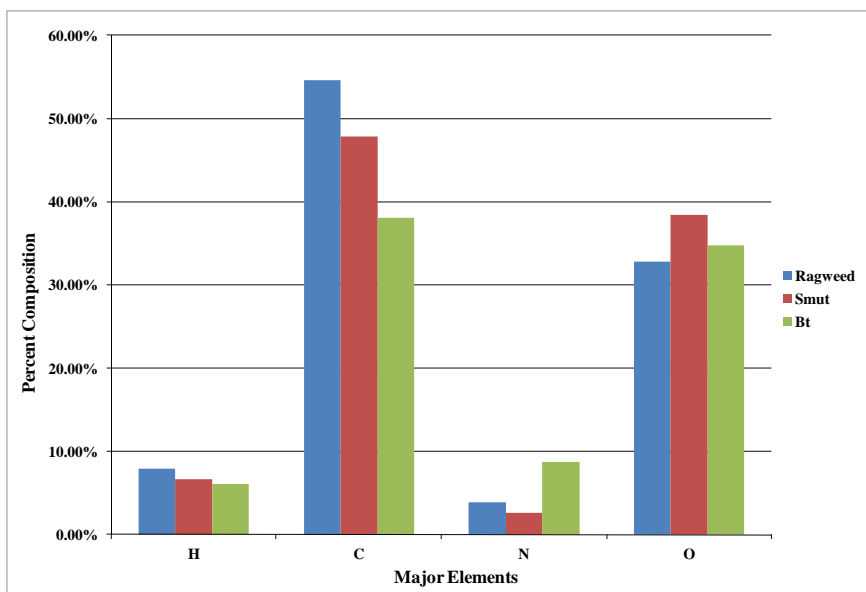


Figure 6.6 Elemental analysis of *Bacillus thuringiensis* (Bt), ragweed pollen, and Johnson grass smut. Major elements were measured with a Perkin-Elmer CHN analyzer by Elemental Analysis Inc., Lexington, Kentucky, USA [17].

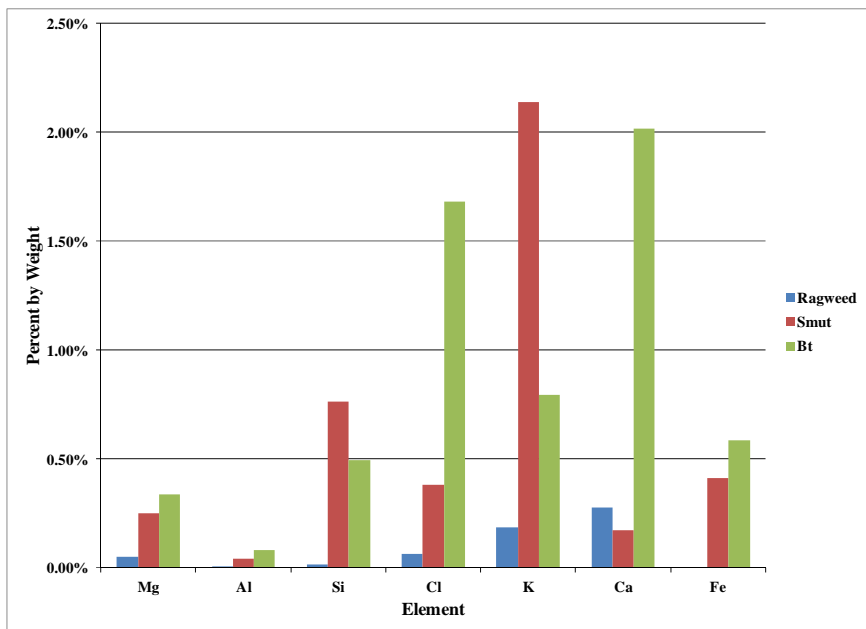


Figure 6.7 Elemental analysis of *Bacillus thuringiensis* (Bt), ragweed pollen, and Johnson grass smut. Minor elements were measured with proton-induced x-ray emission (PIXE) by Elemental Analysis Inc., Lexington, Kentucky, USA [17].

6.5.3 SIBS Atomic and Molecular Features

Understanding the relationship between the concentration of various elemental species and the SIBS signals is a key goal of this work. Besides the electrode lines, the atomic features most prominent in the wavelength regions under study are Ca, Fe, and Si. There are also ionized N lines present. Molecular emission features of CN ($B^2\Sigma^+ - X^2\Sigma^+$), OH ($A^2\Sigma^+ - X^2\Pi_i$), and N_2^+ ($B^2\Sigma_u^+ - X^2\Sigma_g^+$) are all known to be present in the region between 350 and 400nm [12]. The 0–0 band head of CN (B to X) is located at 388.3 nm, and the vibrational manifold extends to the blue (1–1 band head at 387.1 and 2–2 band head at 386.1 nm). These CN features are clearly apparent in all samples, particularly at times early in the plasma evolution. The OH features in this region coexist with N_2^+ features from 345nm to nearly 360nm. Because of the degree of overlap of these two species and their diffuse spectra, even though they are clearly visible in the spectroscopy, their relative abundances are difficult to assess. These are the chief emission features of interest to this study and are tabulated in Table 6.1. The molecular features were only evident by focusing the signal collection optics on the hot electrode.

Table 6.1 Principal lines observed in the SIBS analysis of bioaerosols [17].

Principal Lines Observed in the SIBS Analysis of Bioaerosols	
Species	Observed Lines (nm)
Ca	315.89
	317.93
	318.13
	370.60
	373.69
CN	387.07
	388.21
Fe	385.64
	388.63
Si	288.15
	390.55

6.5.4 Spectral Results

Representative spectral data in two wavelength regions are shown in Figure 6.8 and Figure 6.9. Both figures show only emission spectra for the three samples at one delay time (1 μs for the 300nm region, 2 μs for the 366nm region) for simplicity. Major features are labeled in the captions and are also found in Table 6.1. The elements from the bioaerosol samples are intermixed with lines from the electrode material, which is ablated each time the spark is fired. These electrode lines are well characterized, and their presence helps not only to calibrate wavelength, but to understand the temperature evolution of the spark.

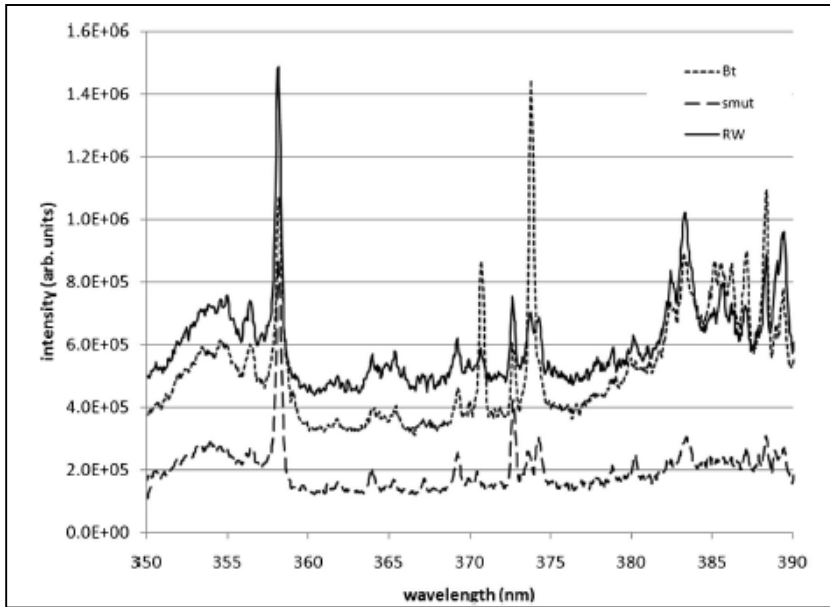


Figure 6.8 SIBS spectra of *Bacillus thuringiensis* (Bt), ragweed pollen (RW), and Johnson grass smut (smut) from 350 to 390nm. Principal emission features in this region are Ca (370.60 and 373.69 nm), CN (B to X, 387.1 and 388.2 nm), N_2^+ (between 350 and 360 nm) and Si (390.55 nm) [17].

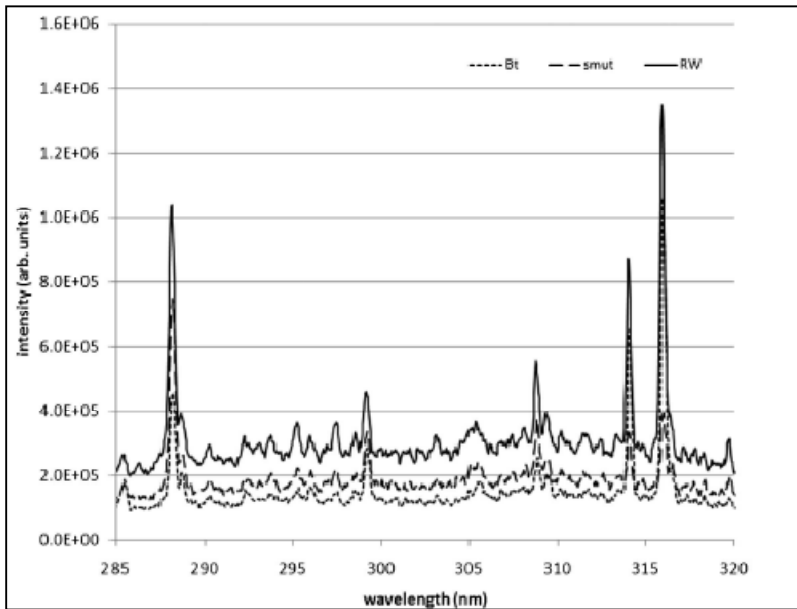


Figure 6.9 SIBS spectra of *Bacillus thuringiensis* (Bt), ragweed pollen (RW), and Johnson grass smut (smut) from 285 to 320nm. Principal emission features in this region are Ca (315.89, 317.93, and 318.13 nm) and Si (299.5 nm). The bright feature at 288.8 nm is an electrode line [17]

This spectral information was processed in a variety of ways. Time profiles of each important emission feature were created with background corrected peak height. Temporal evolution of CN signals from all the samples are shown in Figure 6.10. There is a small amount of CN generated in the sample-free plasma, produced from N and C in the plasma from N₂ and CO₂ in the air. Using laser-induced fluorescence database and spectral simulation software (LIFBASE) and National Institute of Standards and Technology (NIST) atomic line databases [122, 135], we have created a model spectrum at 6000 K that roughly reproduces the spectral data (alkalis and alkali metal elements, known to be present in many biological materials, are not included in the model for simplicity), and demonstrates the aforementioned molecular complexity in the 350–360nm region. This modeled spectrum is shown in Figure 6.11.

The temporal profile in Figure 6.10 shows the CN time profile associated with all three biological samples and a background with matched relative humidity. The profile in this figure seems to indicate the presence of two sources of CN emission, the first being from the sample as it is being processed by the spark, and a second as CN appears to also be generated in the plasma from the recombination of N₂ from the air with carbon in the sample. Error bars in Figure 6.10 indicate uncertainty by percentage (Bt 7%, ragweed 10% and 15% for both humid air and smut sample), which is correlated to the amount of uncertainty typically seen in electrode- only sparks at these signal levels. The background correction was performed by using one-point correction. Through this method, any remaining Bremsstrahlung and continuum emission is removed. As

previously mentioned, a small amount of CN is formed and can be detected when comparing the background signal to the signals produced by the three samples of interest.

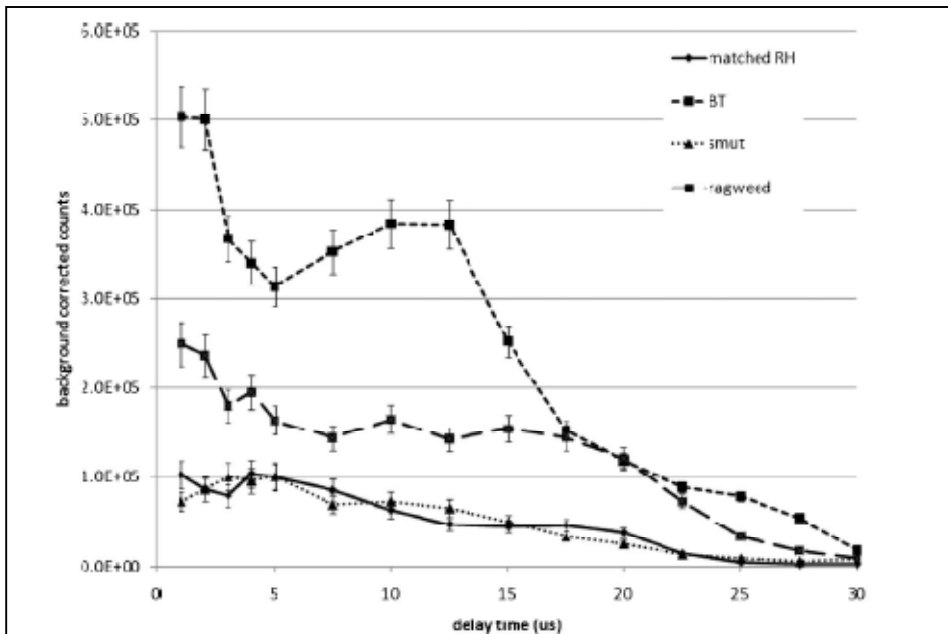


Figure 6.10 Background corrected CN temporal profile at 388.2nm (0 to 0 vibrational band) for Bt, RW, Johnson grass smut smut, and air with matched relative humidity as a background [17].

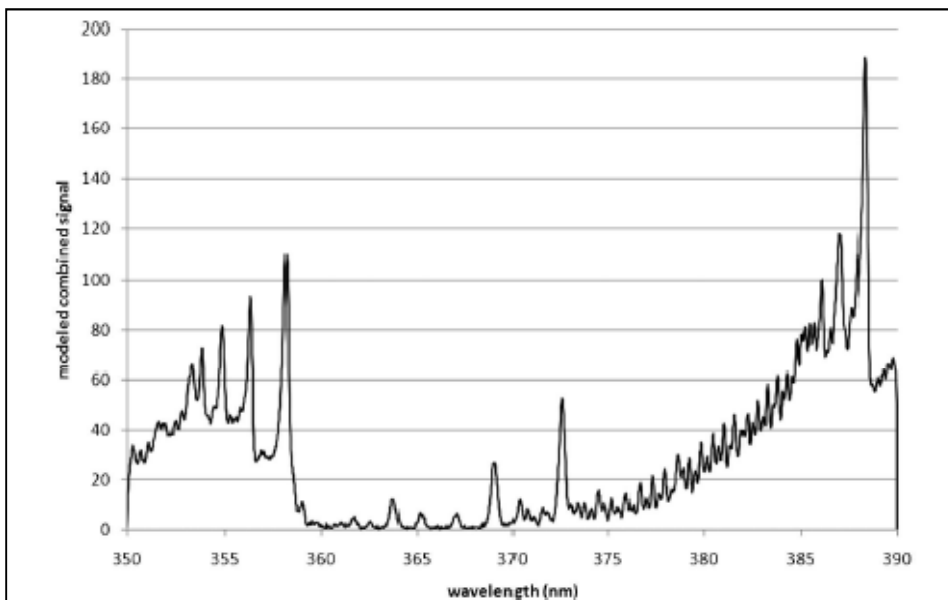


Figure 6.11 Modeled molecular spectra convolved with electrode lines. This synthetic spectrum models the same spectral region seen in Figure 6.8. Molecular features (CN and N_2^+) were modeled at 6000 K [17].

There are interesting differences in the time profiles of each of the samples. These data clearly appear different than CN spectra excited with both nanosecond and femtosecond lasers. Baudelet *et al.* reported that in the case of femtosecond LIBS, CN can be observed from bacterial samples and identified as originating from ablation of protein structures within the cells [46, 133]. They also performed the analysis on graphite samples, which show markedly different behavior, supporting a recombination CN production channel. In the case of the current SIBS data, the growth portion of the time profile actually takes place during the excitation spark, which complicates the analysis of the results. The time profile of Ca II at 373.69 nm is shown in Figure 6.12, and is background corrected through a one-point correction as performed on the CN feature in Figure 6.10. The time profile of ionized Ca is representative of the behavior of most elements in the post spark environment, in that it has a peak during the excitation pulse followed by emission decay. As expected, the decay of emission features is faster for ionized species than neutral ones. This graph is shown as a comparison to the time profile of the CN (Figure 6.10), which shows a period of signal growth before the decay begins, rather than the exponential decay expected in the case of most atomic features.

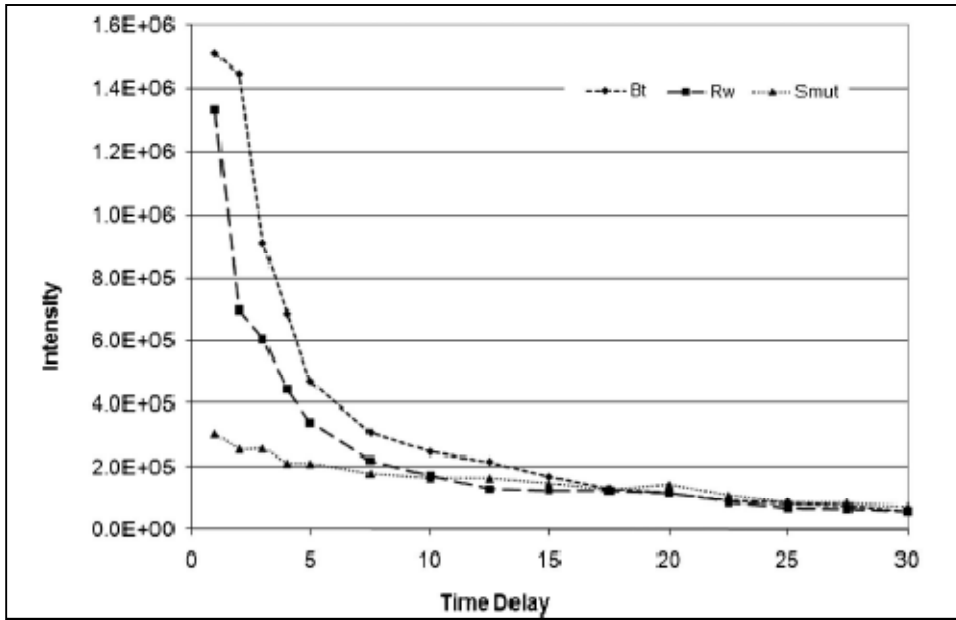


Figure 6.12 Background corrected Ca II temporal profiles (373.69 nm) for Bt, RW, and smut [17].

The temporal profiles are important for the signal optimization of the species of interest. While peak height and peak area measurements in direct plasma ablation spectroscopic techniques are only rarely related in a meaningful way to concentration, total emission over the duration of the feature is often related [16]. Therefore, the emission characteristic used to create the response curves is the sum of the signal in the time profile. In cases where the emission line is relatively free of interference from emissions of other species, the relationship between this signal summation and elemental analysis appears to be nearly linear. This type of relationship is shown in Figure 6.13 and Figure 6.14. Figure 6.13 shows integrated background subtracted signals of the CN vibrational features at 387.07nm (dashed line). Especially noteworthy in this preliminary data is the correlation between the measured concentration of nitrogen in the sample and the integrated signal of the CN spectral data. The correlation between these two values appears to be reasonable, at least in these three cases, in spite of the fact that there is about 2.5 μg of air in the spark gap and about 0.7 μg of sample. Background CN signal from excitation of humidified air is also present, from plasma excitation of N_2 and CO_2 in ambient air. A linear fit of these data has an R^2 of 0.934.

Similarly, we observed good correlations in the case of signals from Fe, Ca, and Al with elemental analysis in this wavelength region. The integrated Ca II (373.69 nm) data are plotted against PIXE Ca data in Figure 6.14. A linear fit of these data has an R^2 of 0.995. The silicon lines at 288.16 and 390.55 nm do not have linear relationships with the elemental composition data. There are electrode lines and other atomic lines underlying each of these features, complicating the interpretation of the emission strength

in these regions. Given a clear line, however, these preliminary data demonstrate good agreement between the summed atomic and molecular emissions and the independently measured elemental composition. However, these results are preliminary and do not yet indicate that SIBS can be used to classify biological aerosols. There are several challenges which make the ability to distinguish between biological species difficult. For example, it is not be probable to pre-test every possible type of bacteria to put into a database. Thus, while our research indicates linear correlation between measured elemental composition and signal emission, the preliminary data presented in this chapter does not show that SIBS can be used to distinguish and classify bioaerosols at this point.

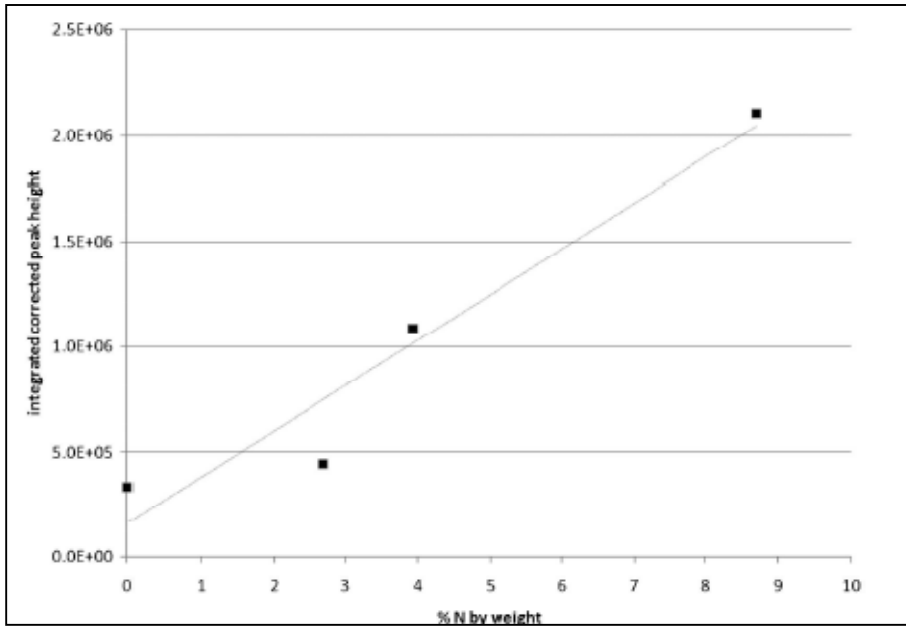


Figure 6.13 Plot of integrated background corrected peak height of CN (387.1nm) feature versus % N by weight as analyzed by combustion in the laboratory. R^2 of line drawn through these data is 0.934 [17].

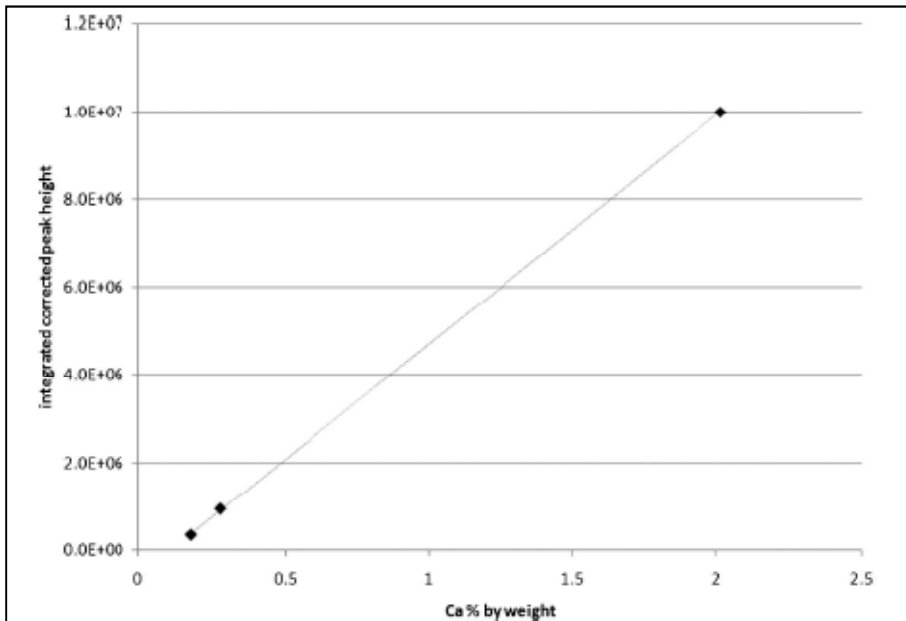


Figure 6.14 Plot of integrated background corrected peak height of Ca II (373.69 nm) versus % Ca by weight as analyzed by PIXE. R^2 of a line through these data is 0.995 [17].

6.6 Chapter Conclusions

First, the early electrode position study was important to the overall fundamental understanding of SIBS technology. As previously mentioned, SIBS is a relatively new analytical tool to quantify the elemental composition of samples. Therefore, the basic understanding of how the spectral signals behaved at different focused regions of the plasma is crucial for the optimization of SIBS. The data presented in this chapter indicated that by focusing on the hot electrode, a full intensity profile of calcium could be obtained. This is important when determining the optimal data acquisition profile for the elements of interest. In addition, it was observed that by focusing only on the hot electrode, molecular features were observed. The different time profiles achieved while focusing at different probed volume of the plasma indicates that the plasma is not homogenous. This is also evident in the fact that no molecular features were observed when focused on the ground electrodes in the preliminary data. Thus, all the data presented was collected while focusing on the hot electrode.

Second, the preliminary work lends credence to previous claims that the integrated emission strength has a relationship with independently established elemental composition measurements. In four out of five emission features, there appears to be a linear dependence between the temporally integrated feature strength and the concentration of the associated element. In the case of Si, the emission features in these wavelength regions are not free of interference from other elements. Additionally, it has been observed in this small and preliminary data set that the CN (B–X) emission has a linear relationship with the nitrogen content of the sample as determined with combustion

analysis. In addition, these data demonstrate varying decay kinetics from sample to sample. These results present preliminary data correlating atomic and molecular emission strengths with elemental analysis. However, further research must be performed in order to determine if SIBS is a viable application to classify biological aerosols.

Chapter 7 : LIBS Spectroscopic Studies of Hematite in Simulated Martian Atmosphere

7.1 Introduction

In recent years, the use of LIBS for planetary exploration has been proposed. In fact, NASA's Mars Science Laboratory (MSL) rover, named Curiosity, contains the first LIBS instrument (ChemCam) for the exploration of Mars [28]. The primary goal of ChemCam is to investigate and analyze the diversity of the Martian geochemistry [136]. Mars has an atmosphere which is comprised of approximately 95.3% carbon dioxide, 2.7% nitrogen and 1.6% argon, with an average atmospheric pressure of about 7 T (varies from 1 to 9 T), depending upon altitude and meteorological conditions. Earth, on the other hand, has an atmosphere which is comprised of approximately 78% nitrogen, 21% oxygen, 1% argon and trace amounts of carbon dioxide [29]. Thus, the atmospheric composition and pressure on Mars produces different physical properties of the plasma compared to Earth [28].

Several studies have been conducted to understand the effect of pressure on the LIBS spectra [5, 20, 137-140]. Yalçın *et al.* found that when using a femtosecond laser at low pressures, the emission peaks are better defined and background emission is reduced [138]. They also observed an increase in peak intensity at low pressures similar to the

Martian atmosphere (1 to 4 T). However, a simulated Mars atmosphere was not used during this study. Sallé *et al.* studied the influence of the ambient pressure, 7 Torr of CO₂, on the calibration curves prepared from soil and clay pellets [137]. Results indicated that useful calibration curves could be obtained at reduced pressure, and these curves from clays and soils showed that matrix effects appear less important at low pressures. Conversely, an atmosphere comprised of pure CO₂ was used to simulate the Martian atmosphere, when the Mars atmosphere is approximately 95% CO₂. Thus, the calibration curves produced under pure CO₂ could be inaccurate when applied to data from Mars. In fact, some researchers often use only CO₂ to represent the Martian atmosphere in laboratory simulations and calibration efforts [139, 140]. Many variables can affect LIBS signal such as, temperature, laser power, gating delay and width, sample surface conditions and the composition of the atmosphere. Further studies will improve the ability to optimize the use of LIBS in harsh environments such as Mars.

The objective of this study was to evaluate how different pressures and atmospheric compositions altered LIBS spectra of a simulant of a Martian mineral. Initially, this research focused on understanding how the changes in atmospheric composition would impact spectral linewidths. The hypothesis was that the LIBS spectra under a CO₂ atmosphere will behave differently than LIBS spectra under a more carefully simulated Martian atmosphere. Our research group hypothesized that the small amounts of N₂ and Ar under low pressure might significantly alter the behavior of the plasma formation, and therefore, the apparent atom emissions. This is due to the fact that a pure CO₂ atmosphere has a higher thermal conductivity than a Martian atmosphere. A high

thermal conductivity means that the heat transfer occurs faster than a low thermal conductivity. Thus, the Mars-simulated atmosphere would provide a plasma that transfers heat at a slower rate, which would result in a longer plasma lifetime. In addition, Ar has a high ionization potential which means it does not readily give up electrons. Thus, Ar easily ionizes elements within a sample compared to CO₂. Furthermore, the high ionization potential of Ar might increase the potential for plasma shielding, which would result in smaller plasmas compared to a CO₂ atmosphere [141]. These differences should influence plasma formation, and these differences should be observed in the linewidths, intensities, and plasma size as a function of atmospheric composition and pressure.

Comparisons between linewidths and pressures as well as plasma size versus pressure was studied to observe differences, if any, between the two different atmospheres. Another purpose of this research was to illustrate that the signal intensity is influenced not only by the concentration of the element in the sample, but also by the properties of the plasma itself [142].

7.2 Experimental Design

The following sections outline the different experimental details between the various studies. First, early LIBS work included building a vacuum chamber in order to study the LIBS spectra from hematite. An atmosphere comprised of CO₂ was analyzed at three different delay times. The goal of this study was to show the spectral behaviors as a function of delay time in a CO₂ atmosphere.

Second, later LIBS work included the use of a motorized XY stage while maintaining a similar vacuum chamber setup. This research also involved the use of a more accurate Martian-simulated atmosphere comprised of not only CO₂, but Ar and N₂. The purpose of this was to determine whether there are spectral differences based on the atmospheric make-up.

7.2.1 Establishment of Early LIBS Experiments

A large portion of this research included the design and building of a proper setup that would allow the study of hematite under varying pressures. Hematite was used as a Mars simulated surface due to iron rich nature of Martian soil [143]. An INNOV-X portable x-ray fluorescence device (PXRF, Olympus, Woburn, MA) was used to determine the elemental concentrations in the rock used during analysis. Table 7.1 includes the composition of the predominant elements found in the hematite. Figure 7.1 illustrates the design for this experiment. LIBS experiments were carried out using Q-switched Nd: YAG laser (Quantel, Bozeman, MT) that had an output wavelength of 1064 nm. The beam energy was 110 mJ per pulse, and the laser pulse width was 10.3 ns with a repetition rate of 20 Hz. The plasma that is created from the ablative pulse emits light that is collected by a fiber optic bundle situated at a 45° to the direction of the laser input focused onto sample surface. This information was delivered to a ¼ m spectrometer with a 1200 l/mm grating interfaced to an Andor iStar ICCD (Andor Technology, South Windsor, CT). For these initial experiments, an unpolished oolitic sample (containing hematite) was attached to a stationary platform. This platform was used to position the

hematite directly under the collection optics at a 45° angle. Thus, the sample was stationary during data collection, and was only moved periodically after several data points were collected. This was done primarily so that the vacuum was not broken during sampling. Three delay times were collected for this work (0.5, 1.0, 1.5 μs), with a gate width of 1 μs . 20 laser shots were taken at each pressure and averaged. The range of the collected spectrum is approximately 40 nm, and the center wavelength was set to 380 nm. The glass container was connected to a CO_2 cylinder through a flowmeter, as well as a capacitance manometer to measure the pressure inside the chamber.

A pure CO_2 atmosphere under reduced pressure was used to determine the effect of atmosphere on the spectra produced by the plasmas. A CO_2 atmosphere was measured from 0.1 to 600 Torr (T). To test this, a CO_2 cylinder was opened and allowed to fill the vessel. The pump was then turned on to create the vacuum at 0.1 T, which purged the chamber of Earth atmosphere. A continuous flow of CO_2 was regulated to maintain a constant pressure at each measurement. Each time the desired pressure was achieved, the laser was turned on and data collected. Data were collected approximately every 1 T from 0.1 to 15 T and then every 10 T after that up to 100 T. Subsequently, readings were only taken every 50 T, up to 600 T. This was repeated for each of the three delay times.

The spectra created by each of these pressures in each of the atmospheres were then fit to Gaussian profiles using WaveMetrics (Igor) software to determine the linewidths of the elements of interest. Ca II at 396.85 nm was the principal peak analyzed. The plasmas created by the pulses were also imaged by a digital camera ('night' setting in a dark room) to correlate the size of the plasma to the pressure at which

it was taken. These images were processed with Adobe Photoshop to determine the number of pixels in the plasma-illuminated region. These data were collected as a function of CO₂ pressures from 0.1 to 590 T.

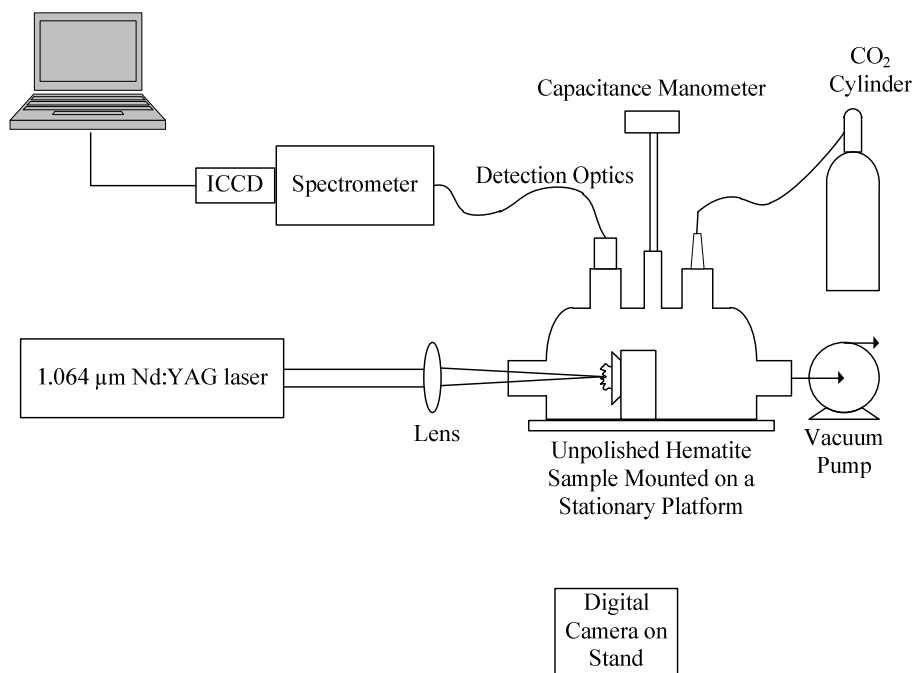


Figure 7.1 A schematic diagram of the early experimental LIBS setup for analyzing oolitic hematite sample under a CO₂ atmosphere. A digital camera mounted on a stand was used to collect plasma images.

Table 7.1 Elemental composition determined by XRF of the hematite used during data analysis.

Element	% Composition	±
S	3.68	0.27
K	1.76	0.04
Ca	6.06	0.11
Ti	0.61	0.02
Ba	0.05	0.005
Cr	0.01	0.002
Mn	0.14	0.004
Fe	>10%	

7.2.2 Experimental Design Comparing Earth, CO₂ and Mars Atmospheres

During these experiments, the laser and vacuum chamber design were maintained from the previous section. However, there were changes to the sampling platform and surface. First, a cut and polished hematite sample was used in order to maintain a constant focal distance between the focal lens and sampling surface, and therefore, reduce shot-to-shot variability during sampling. The hematite sample was also attached to a motorized XY stage, which was placed inside the evacuated glass chamber (Figure 7.2). The stage was motorized so that the position of the rock was controlled without breaking the vacuum inside the chamber. The primary reason for translating the hematite sample during analysis was to avoid repeated ablation at the same location which creates a crater and changes the focal distance between focusing lens and sample surface [144]. In addition, it is important to sample many areas of the hematite sample to account for inhomogeneity [145]. Averaging the spectra over different locations on the hematite sample gives a more accurate correlation with the bulk composition of the sample. The motorized XY stage was engineered in the lab. Two identical miniature dovetail manual translation stages were purchased from ThorLabs (Newton, NJ). These were attached together in such a way that one would move left and right (X plane) and the other would move up and down (Y plane). To motorize the manual stages, an RC controller with servo motors and gear wheels were purchased. The gear wheels were each attached to each of the stage translational knobs. Each stage had its own servo to control the movement in either the X or Y direction. The servos were secured to the stage inside the vacuum chamber, and a rubber band was used to connect the wheels on the servo motor

to the wheel on the stage. The motors were adapted so that they could turn 360° instead of 180° , and therefore be used for continuous operation. Continuous operation, allows for motion control of the stage in both the X and Y stage simultaneously. This method made it possible to reduce the number of shots in the same place while keeping the vacuum sealed during the experiment.

All the measurements were obtained using a 20-Hz repetition rate, with a delay time between plasma formation and data acquisition of $1.5 \mu\text{s}$ and an acquisition gate width of $1 \mu\text{s}$. Spectra from 40 laser shots were taken at each pressure and averaged. The range of the collected spectrum is approximately 40 nm, and the center wavelength was set to 380 nm. The glass container was connected to three different cylinders (CO_2 , Ar, and N_2) through flowmeters, as well as a capacitance manometer to measure the pressure inside the chamber. Therefore, the flow rates of the three gases were maintained to deliver the correct gas ratios for a simulated Martian atmosphere. While collecting data under a pure CO_2 environment, the Ar and N_2 values were closed, and only CO_2 was allowed to enter the chamber.

When using pure CO_2 , a continuous flow of CO_2 is added to the vacuum chamber until the desired pressure is achieved. However, when using a gas mixture from three different cylinders, one will only know the total pressure, not the fractions from each cylinder. In order to achieve the specific atmosphere needed to simulate a Martian atmosphere, the flow rate of the three tanks had to be calibrated. Each flowmeter was calibrated using a soap film bubble flowmeter. The cylinder and flowmeter was attached to the bottom of a volumetric glass tube containing a small amount of liquid soap. As the

cylinder valve pushed air through the tube, a flat soap bubble is interposed in the flow path. While the air flow causes the soap film to move from one volume mark to another, the travel time is measured with a stopwatch. The flow rate can then be directly calculated using the travel time and the known tube volume. The rate at which the bubbles traveled corresponded to a certain reading on the flowmeter at each pressure output from the cylinder valve. This procedure was repeated at several different valve settings for each gas cylinder, and a linear regression was performed for each. By using the information obtained from this calibration curve, it was possible to know the exact valve settings at which CO₂ accounted for 95% of the total gas flow, N₂ accounted for 3%, and Ar accounted for 2%.

Two main experiments were done to determine the effect of atmosphere on the spectra produced by the plasmas. First, a pure CO₂ atmosphere was measured from 0.1 to 200 T. To test this, the CO₂ cylinder was opened and allowed to fill the vessel. The pump was then turned on to create the vacuum at 0.1 T. CO₂ was used to slowly pressurize the chamber to get the remaining measurements. Each time the desired pressure was achieved, the laser was turned on and data collected. Data were collected approximately every 1 T from 0.1 to 15 T and then every 10 T after that until 100 T. Subsequently, readings were only taken every 25 T. Next, a more accurate Mars simulated atmosphere was tested, with 95% CO₂, 3% N₂, and 2% Ar. This was achieved by allowing the CO₂, N₂, and Ar valves connected to the flowmeters to be opened in proportional amounts to the representative percentages. The same procedure was used to evaluate from 0.1 to 200 T. In addition, spectral data was collected under Earth atmosphere from 0.1 to 600 T.

The objective of this was to observe differences in the spectral line widths and intensities between Earth ambient atmosphere compared to those of CO₂ and Mars.

The spectra created by each of these pressures in each of the atmospheres were then fit to Gaussian profiles and analyzed using WaveMetrics (Igor) software to determine the linewidths of the elements of interest. Ca II, Al I, and Fe I were the principal peaks analyzed. The plasmas created by the pulses were also imaged by a Phantom v7.3 high speed camera (Vision Research, Wayne, NJ) to correlate the size of the plasma to the pressure at which it was taken. These images were processed with Adobe Photoshop to determine the number of pixels in the plasma-illuminated region. These data were collected as a function of CO₂ and Martian-simulated atmospheres using pressures from 0.1 to 200 T.

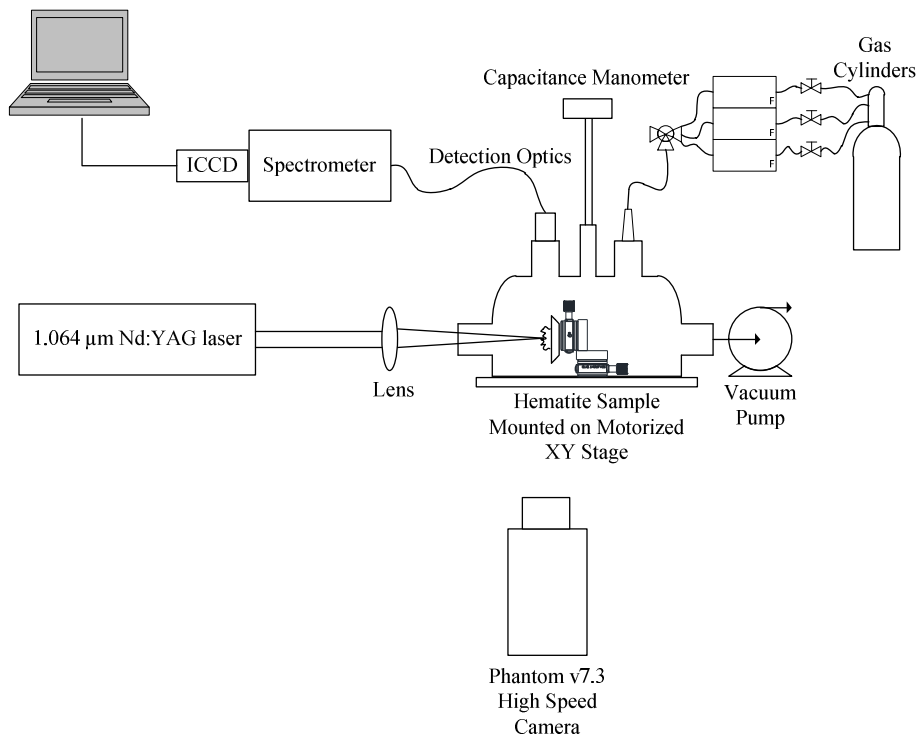


Figure 7.2 A schematic diagram of the LIBS setup for analyzing hematite sample under a CO₂ and Martian atmosphere. Each cylinder was attached to a valve and flowmeter. A mixing valve was in place prior to the glass chamber in order to allow proper gas ratios into the chamber.

7.3 Results

The following sections present results for both preliminary studies of pressures under a CO₂ atmosphere and a Mars-simulated atmosphere. The main purpose of this research was to observe differences, if any, between a pure CO₂ and a Mars-like atmosphere. Earth atmosphere was also analyzed under 0.1 to 600 T in order to make general observations of the differences between spectral line widths and intensities. Section 7.3.1 includes CO₂ data only using an unpolished, stationary hematite sample. Section 7.3.2 includes CO₂, Earth and Mars atmospheres using a polished hematite sample attached to a motorized stage for data collection.

7.3.1 Results of a Pure CO₂ Atmosphere

LIBS spectra of hematite samples were obtained at a variety of pressures at three delay times including 500 ns, 1.0 μ s and 1.5 μ s. Figure 7.3 shows sample spectra of the wavelength region of 360 nm to 400 nm under a CO₂ atmosphere at four different pressures with a 500 ns gate delay. The majority of lines in this region consist of Ca II, Al I, Si I and Fe I, and the line assignments were identified and referenced by the NIST Atomic Spectra Database [135]. Figure 7.4 represents sample spectra of the wavelength region 390 nm to 398 nm under a CO₂ atmosphere at four different pressures with a 500 ns gate delay. This narrow wavelength region illustrates the broadening of the spectral lines as the pressure increases. At extremely low pressures, the spectral line intensity is low. As the pressure increases, the spectral intensities of the various lines increase until a pressure of approximately 11 T is reached. At this point, the intensities remain

statistically constant until approximately 30 T. At this point, the intensities begin to decrease, and is illustrated in Figure 7.5.

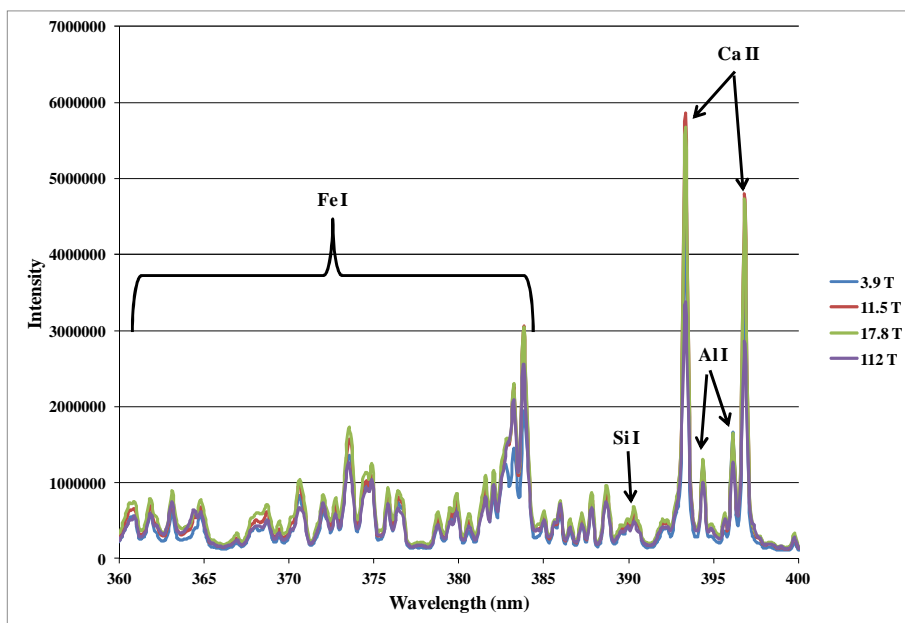


Figure 7.3 Sample spectra under a CO₂ atmosphere at a variety of pressures from 360 nm to 400 nm with a 500 ns delay. Key elemental features are labeled, and the majority of the lines in this region consist of Fe.

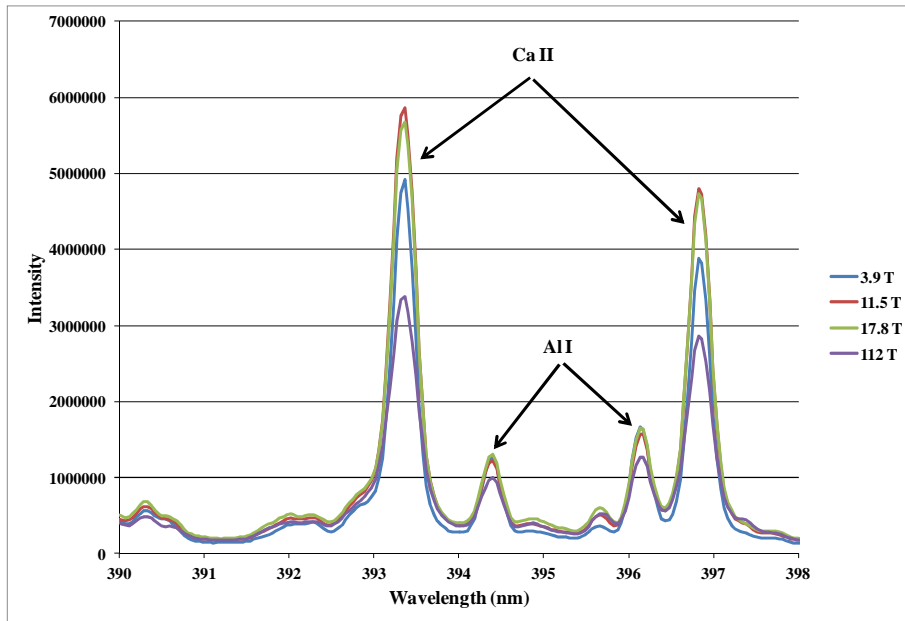


Figure 7.4 Four sample spectra under a CO₂ atmosphere in the 390 nm to 398 nm region. This narrow region illustrates the change in linewidth and intensity with an increase in pressure.

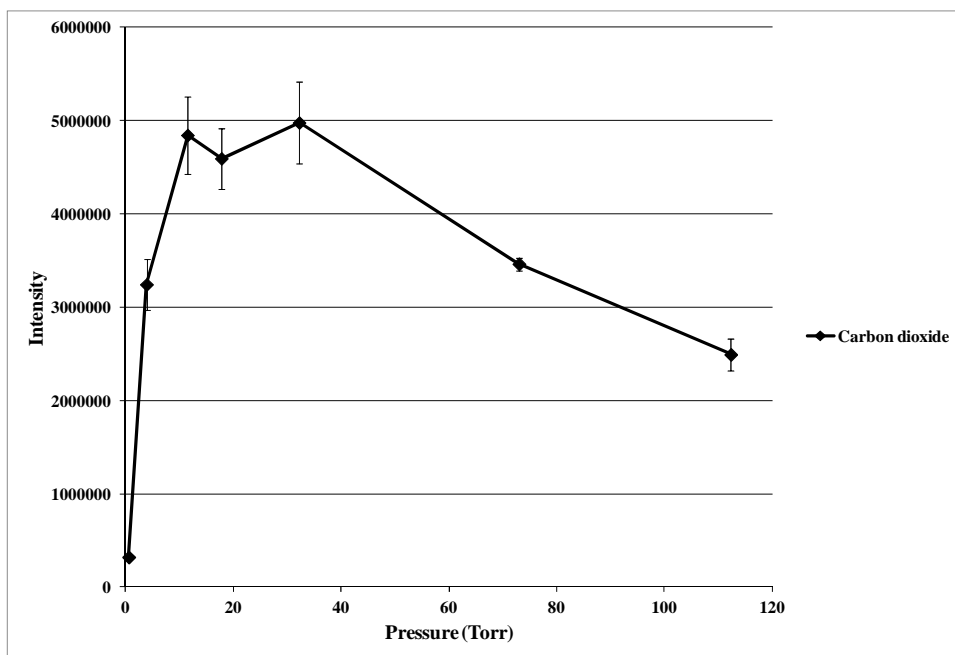


Figure 7.5 A comparison of the Ca (II) 396.85 nm baseline corrected line intensity of hematite under a CO₂ atmosphere. The intensity of the Ca line begins decreasing around 30 T.

To determine linewidths of spectra collected under different conditions, the widths of the Ca II peak (396.85 nm) at varying pressures under a CO₂ atmosphere were fit to Gaussian profiles. Figure 7.6 compares the Ca II line between the three different delay times at a variety of pressures. A comparison was made between the linewidth of the Ca (II) line at 396.85 nm with increasing pressures at three different gate delays of 500 ns, 1.0 μs and 1.5 μs while maintaining a gate width of 1.0 μs. The Ca (II) line is considerably narrower at low pressures (0.1 to 10 T) with the gate delays of the 1.0 μs and 1.5 μs delay times compared to the 500 ns time. As the pressure increases, the width of the Ca (II) line increases at each delay time. Ideally, one would evaluate several gated delay times in order to optimize the spectral signals of interest at pressures resembling Mars atmosphere. This would include maximizing signal intensity while providing the best S/N enhancement at 7 T. These preliminary results indicate that slight changes in the gate delay can have significant changes in linewidths. In addition, the linewidth increase is not linear under a CO₂ atmosphere, which is to be expected. The main line-broadening mechanism is the Stark effect (pressure broadening) which is related to electron number density. The Ca (II) at 396.85 nm has a low energy final level (connected to the ground state), which is known to exhibit self-absorption. At 7 T, self-absorption is minimized, and an improvement of the spectral data is observed. This is due to the fact that at low pressures, electron collisions are reduced, which results in narrow line profiles. At high pressures, there is an increase in collisions which result in broadening.

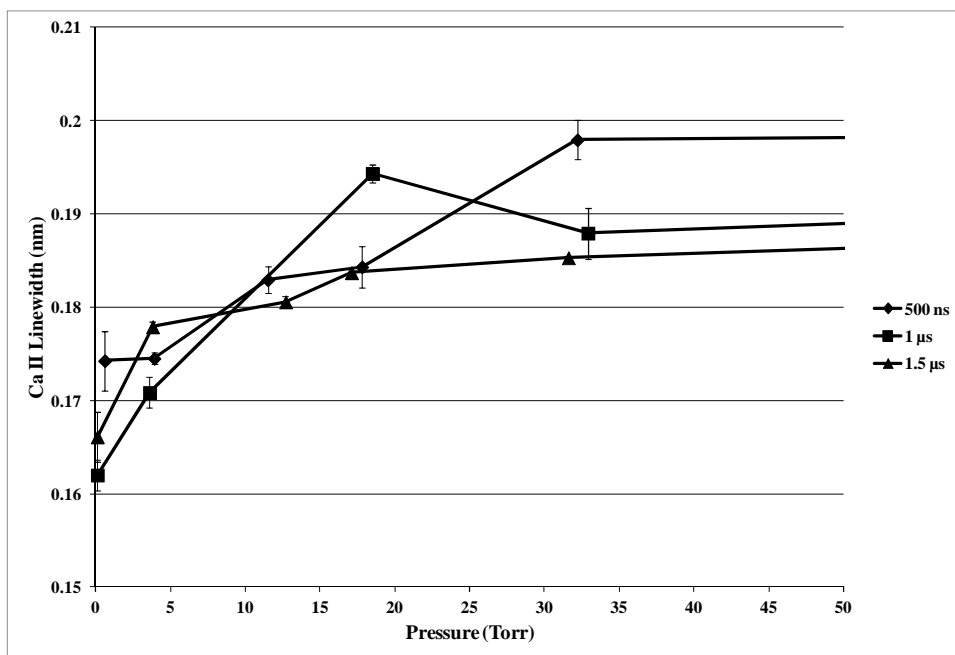


Figure 7.6 Ca (II) 396.85 nm linewidth comparisons of three different gate width delay times. As the pressure increases, the linewidth increases nonlinearly.

Another important aspect of this experiment is to compare the plasma size and pressure. Figure 7.7 relates the area of the plasma (pixels) in the images as the pressure increases under pure CO₂. These preliminary data do not include errors bars since minimal data were collected. However, the apparent size of the plasma drops with pressure, with the exception of behavior at the very low pressure region (< 1 T). At the low pressure region, it is increasingly difficult to form a plasma because of the increased expansion due to the lack of sufficient atmosphere to provide adequate plasma confinement, and decreased collision excitation. As the pressure increases, the plasma is confined to a small area and is expected to have a higher density. Although preliminary, these results are consistent with other research. For example, Yalçın *et al.* examined 2D plasma images of a Cu plasma at 760, 1.79, 0.85 and 0.167 Torr [138]. They found that the plasma becomes less ordered as the pressure decreases and expands more toward the laser as pressure is reduced. These results coincide with the results found in Figure 7.7.

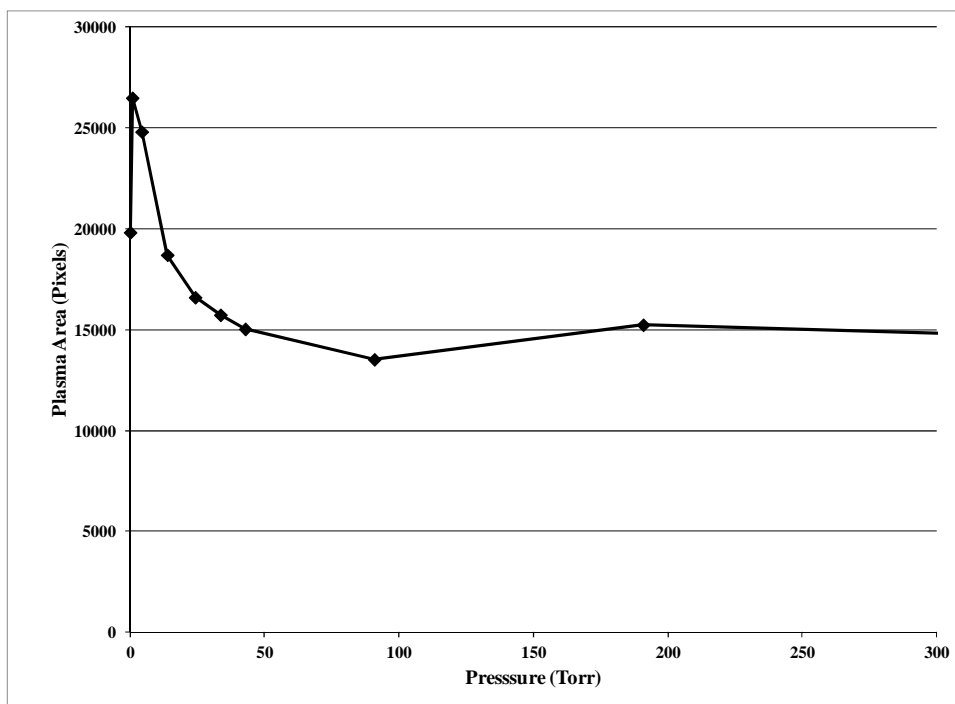


Figure 7.7 Plasma area (pixels) compared to pressure (T) under a CO₂ atmosphere.

7.3.2 Results of LIBS Spectra under Earth, CO₂ and Martian Atmospheres

LIBS spectra of hematite samples were obtained at a variety of pressures at a delay of 1.5 μs and a gate width of 1.0 μs under three different atmospheres. Figure 7.8 and Figure 7.9 are sample spectra of the wavelength region of 360 to 400 nm under a Mars-simulated atmosphere. The majority of lines in this region consist of Ca II, Si I, and Fe I, and the line assignments were identified and referenced by the NIST Atomic Spectra Database [135]. At very low pressures (0.1 T), the overall spectral intensity is considerably lower than in higher pressures. Figure 7.9 illustrates the change in spectral linewidths and intensities with a change in pressure.

In order to assess the effect of the varying ambient pressure, the widths of Ca II, Al I and Fe I peaks at varying pressures under both simulated atmospheres were fit to Gaussian profiles. Figure 7.10, Figure 7.11 and Figure 7.12 compare the Al (I) 396.1 nm, Ca (II) 396.8 nm and Fe (I) 362.1 nm lines, respectively, between the two different atmospheric (Mars and CO₂) conditions from 0.1 to 10 T. Just as seen in the preliminary results using CO₂ only, the linewidths increase with an increase in pressure, but non-linearly. However, using this preliminary data, there are no statistical differences between linewidth and pressure between CO₂ and a Mars-like atmosphere. Table 7.2 illustrates the linewidths of Al (II), Ca (II) and Fe (I) under three different atmospheres. However, for Ca (II) and Al (I), there are statistically significant differences between ambient Earth pressure (600 T) and the other two atmospheres at approximately 7 T. On the other hand the linewidth of Fe (I) remains relatively constant between the three atmospheres. These results found in Table 7.2 demonstrate self-absorption. The line

broadening observed in the Ca (II) and Al (I) lines are due to the fact that these lines have their energy of the lower level of transition to the ground state [135]. Thus, the line broadening in all three atmospheres indicates these lines suffer from self-absorption as the pressure increases. On the other hand, the Fe (I) line at 362.1 nm does not have its lower level of transition to the ground state, and its linewidth remains nearly constant across all atmospheres. These results are consistent with those obtained from Sallé *et al.* and Arp *et al.* at high pressure: the elements that are present at concentrations of more than a few percent by weight (Fe and Ca, Table 7.1) in the sample, and have ground state transitions, are those that show strong effects of a pressure increase by broadening and self-absorption [137, 140]. Elements that are present in low concentrations will not exhibit the strong effects of broadening with pressure increase even if they are resonance lines. These results also illustrate that the inclusion of Ar in the Mars-like atmosphere did not have an increase in plasma shielding, and therefore, a decrease in linewidths.

Similarly, the signal intensities of Fe (I), Al (I) and Ca (II) were compared between the three different atmospheres as they relate to pressure increase. Figure 7.13 is a comparison of the Ca (II) 396.85 nm emission line between CO₂ and Mars atmospheres. At low pressures, the electron density and plasma shielding are minimal, which results in an increase in signal intensity. In addition, ablation of the target sample increases with decreasing pressure. At low pressures, plasma shielding is reduced which permits more of the incident laser pulse energy to reach the sample surface [5]. At low pressures (< 1 T), there are reduced excitation and reduced collisions. As a result, species excitation and the element signal decrease with these extremely low pressures. For pressure below

0.001 T, ablated species are no longer confined near the target surface, and are ejected immediately upon laser irradiation. In this case, the time between collisions is so great that further pressure reduction does not affect excitation of sample species [5]. However, as the pressure increases, the electron density and the plasma shielding increase, which result in a decrease of signal intensity [76, 146]. With an increase in plasma shielding, part of the laser energy is absorbed by the plasma, and therefore the laser energy deposited on the sample is lower, resulting in weaker signal intensities [28, 147-149]. When the pressure around the plasma increases, the plasma cools more quickly due to the reduction of the plasma lifetime and the increase in collisions at higher pressures [141].

Figure 7.13 also indicates that the Mars plasma is brighter than the CO₂ plasma as seen by the overall more intense Ca (II) emission line at higher pressures. Table 7.3 compares the intensities of the Ca (II), Fe (I) and Al (I) lines in Earth, Mars and CO₂ atmospheres. Intensities at ambient conditions (600 T) are lower than at Martian or CO₂ conditions. This is due to the fact that the Mars atmosphere has a lower thermal conductivity than air, which reduces the cooling rate of the plasma and results in an extended plasma lifetime [5, 20, 138, 139]. A high thermal conductivity (Earth atmosphere) medium produces a relatively fast heat transfer which results in a fast cooling rate and plasma expansion [141]. This indicates that the Martian conditions are ideal for ablation and ionization [28]. However, statistical differences are seen between the Al (I) and Fe (I) lines under the Mars and CO₂ atmospheres. This, in part, could be attributed to data collection at different rock locations, and therefore, different compositional makeup. Composition analysis was not performed on the hematite

samples used during these experiments. But, this is the most likely cause for the differences of line intensities of Al (I) and Fe (I) since both line widths and plasma sizes were not statistically different.

Differences in emission intensity may also be due to the changes in the geometry of the plume as a function of pressure. As the pressure decreases, the plasma becomes larger and consequently, the plasma plume is impossible to fully image with the fiber optic at very low pressures (< 3 T) [146]. Thus, the overall percentage of light captured by the optics is low, which alters the emission line intensities [150]. Therefore, the change in emission intensities may be a result of a change in the alignment of the plasma light on the fiber as the pressure increases [140]. It is clear that the collection location in relation to the confined plasma contributes to the variation seen between experiments, and is a limitation under these conditions.

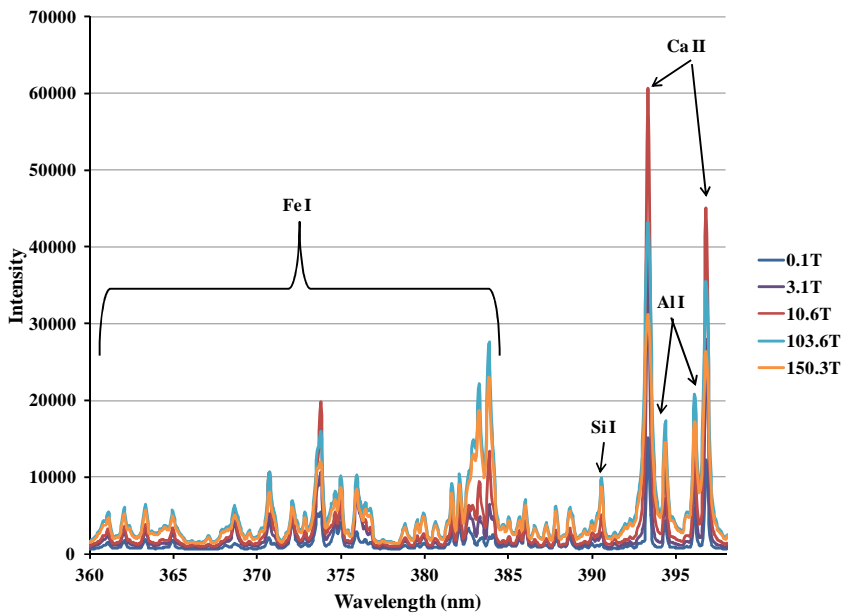


Figure 7.8 Sample spectra of five different pressures under a Mars-like atmosphere with a gate delay of 1.5 μ s.

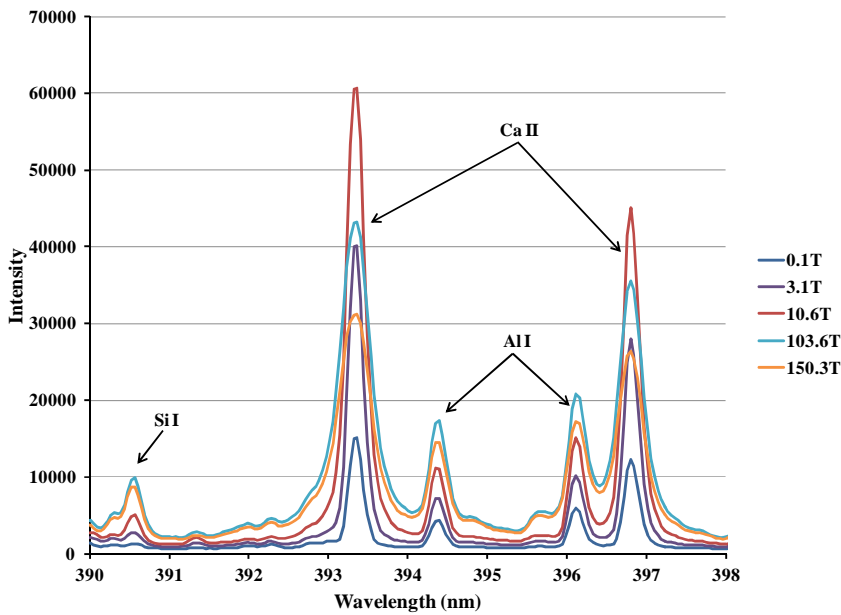


Figure 7.9 Sample spectra of five different pressures with a 1.5 μ s delay under a Mars-like atmosphere. These close-up spectra illustrate the change in line width with a change in pressure.

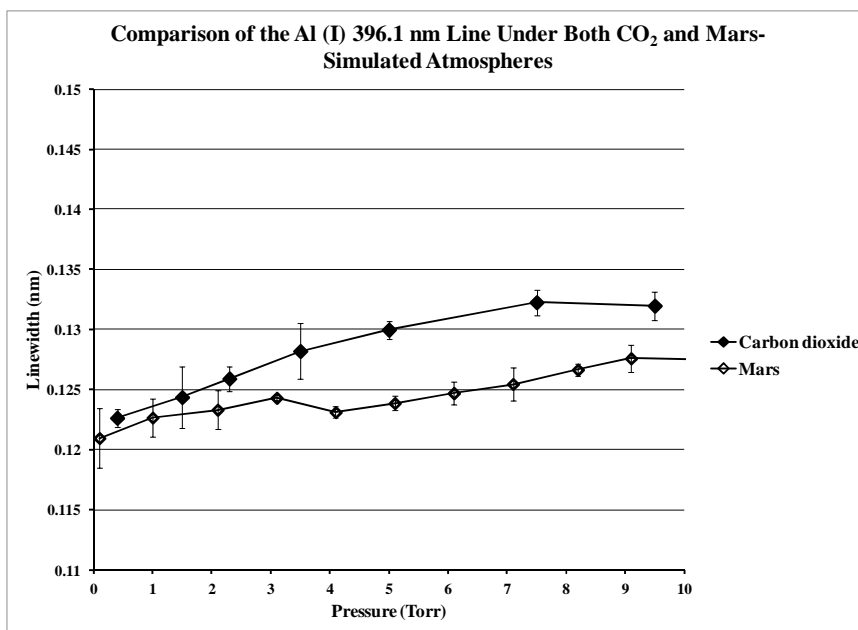


Figure 7.10 Comparison of an Al I line under two different atmospheres at a gate delay of $1.5 \mu\text{s}$ from 0.1 to 10 T.

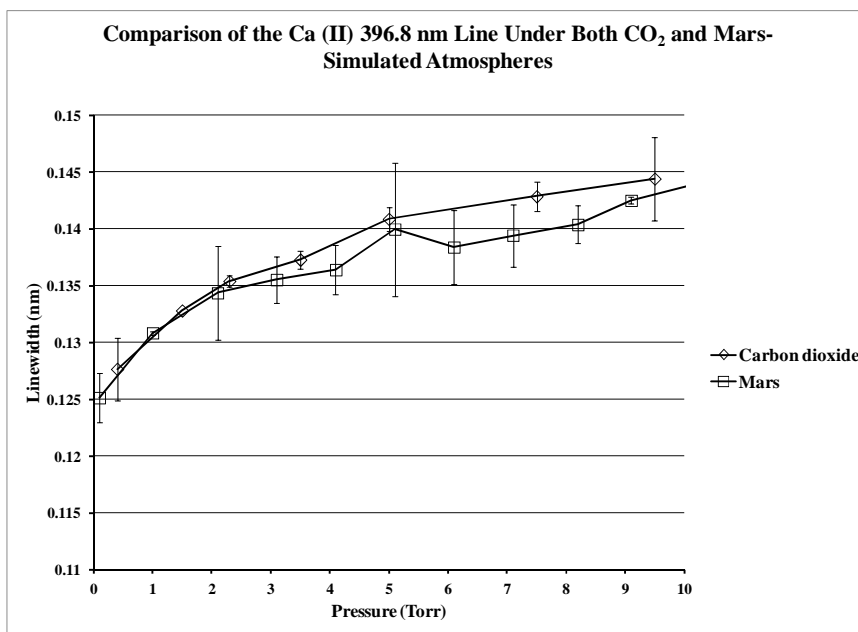


Figure 7.11 Comparison of a Ca II line under two different atmospheres at a gate delay of $1.5 \mu\text{s}$ from 0.1 to 10 T.

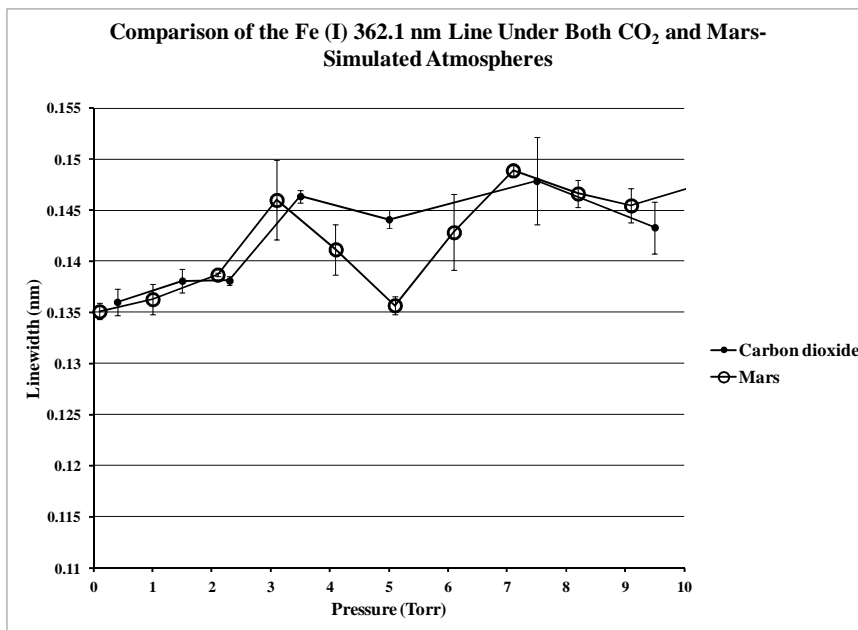


Figure 7.12 Comparison of a Fe I line under two different atmospheres at a gate delay of 1.5 μ s from 0.1 to 10 T.

Table 7.2 Widths of emission lines in the 360 nm to 400 nm range under various conditions. Error was determined from the line fits.

Emission Line	Wavelength (nm)	FWHM (nm)		
		Earth atm.	CO ₂ 7.5 T	Mars 7.1 T
Ca II	396.8	0.261	0.142	0.137
		$\pm .0067$	$\pm .0013$	$\pm .0027$
Al I	396.1	0.204	0.131	0.127
		$\pm .0115$	$\pm .0012$	$\pm .0014$
Fe I	362.1	0.184	0.144	0.148
		$\pm .0106$	$\pm .0043$	$\pm .0064$

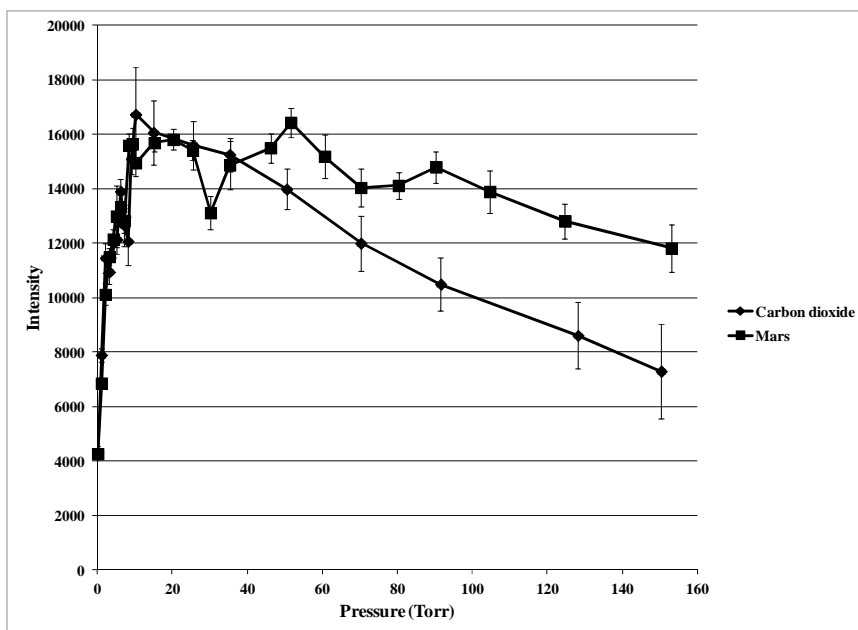


Figure 7.13 Signal intensity of the Ca (II) 396.85 nm line compared to the pressure.

Table 7.3 Intensities of emission lines in the 360 nm to 400 nm range in Earth, Mars and CO₂ atmospheres. Error determined from the number of repetitions.

Emission Line	Wavelength (nm)	Intensities (a.u.)		
		Earth atm.	CO ₂ 7.5 T	Mars 7.1 T
Ca II	396.8	6683.35	12650.08	12828.28
		± 1024.07	± 1545.08	± 893.30
Al I	396.1	3946.48	11807.85	4363.90
		± 557.40	± 895.66	± 354.35
Fe I	362.1	929.32	2729.73	1058.80
		± 172.10	± 233.07	± 116.13

Photographs of the plasmas were taken with a fast frame rate camera in order to compare the plasma size with the pressure. Figure 7.14 depicts the formation and degradation of the plasma under a Mars-simulated atmosphere at 5.1 T. Measurements of the plasma area were completed using Adobe Photoshop, and were taken during the brightest frame of the plasma. Figure 7.15 compares the plasma size and pressure for both atmospheric conditions. At low pressure (< 5 T), the two plasmas are different sizes and behave differently. However, at 5 T, the two plasmas are relatively similar in size. Additionally, although the plasma sizes are different, the overall trend of plasma size with increasing pressure is the same between the two atmospheres. Although slightly different sizes, this difference is not enough to produce differences seen in the linewidths seen in Ca (II), Al (I) and Fe (I). This could indicate that the electron densities are confined in a similar manner producing comparable results even though the atmospheric composition is slightly different. The initial hypothesis suggested that the inclusion of Ar in the atmosphere would produce a higher degree of plasma shielding, which would decrease the apparent linewidth due to a lower electron density. However, these results indicate that the slight compositional differences between the two atmospheres do not change the plasma confinement significantly.

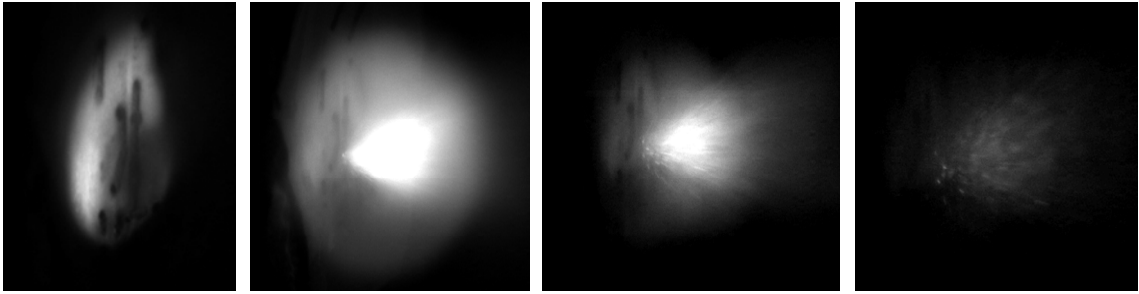


Figure 7.14 A-D (left to right), Output of plasma formation: A.) Laser flashlamp illuminating hematite sample just prior to laser pulse. B). During laser pulse, creation of plasma. This used to determine plasma size. C and D. Post laser pulse, the degradation of the plasma. These pictures were collected under Mars-simulated atmosphere at 5.1 T with 500 μ s, 700 μ s, 800 μ s, 900 μ s; frames and time from beginning of picture collection.

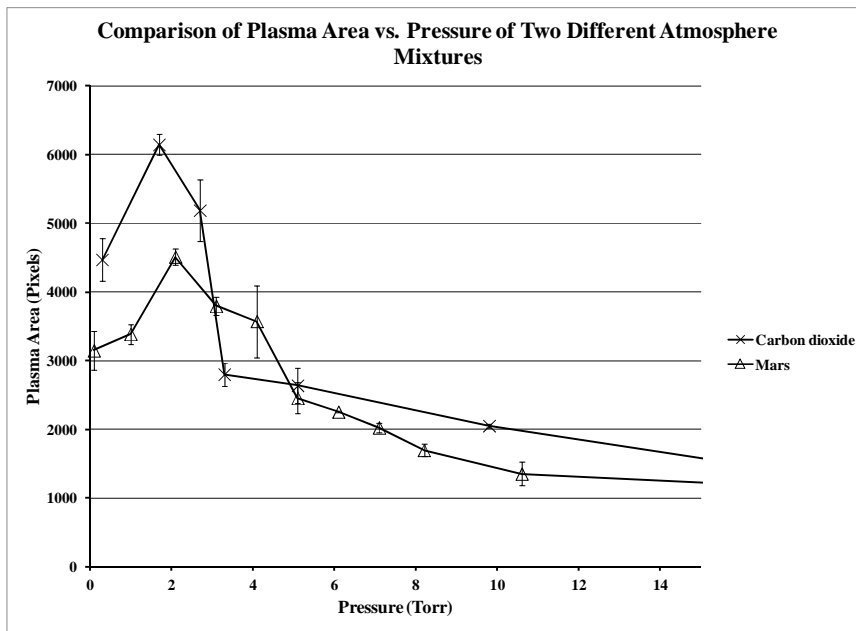


Figure 7.15 Plasma area compared to pressure of the two different atmospheres.

7.4 Chapter Conclusions and Future Research

It has been demonstrated that Mars-like conditions show significant effects on plasma. The results from this study did not produce clear statistical differences in both the linewidths and/or plasma size between the CO₂ and Mars atmospheres. However, it is evident that analyte signals (linewidths and intensities) are strongly dependent on pressure. Results from this study indicate that there is a significant change in plasma expansion as a function of pressure. In addition, the compositional differences between Mars atmosphere and Earth atmosphere affect the plasma expansion and lifetime of plasma. This is due to the thermal conductivity differences between the two atmospheres. Through this research, it is evident that plasma formation and emission depend on several factors: nature of the sample, timing delay and gate width, number of laser shots, angle at which irradiance is collected, pressure, and the nature of the surrounding gas to name a few. Therefore, quantifying elemental composition in geological formations on Mars will be a challenge.

Further research should be performed to ensure more data replicates, and confirm the preliminary findings. However, the preliminary results did correlate with other researchers performing similar experiments presented in this chapter. The change in plasma dynamics between 0.1 and 10 T under a Mars-simulated atmosphere in comparison to CO₂ alone is significant for Mars exploration. As expected, the linewidths did not increase linearly, and further studies should be conducted to better understand and identifying the nature of this relationship. Future research should also include a comparison of delay times for LIBS spectral optimization as well as a comparison

between elemental composition and peak intensities. These studies will aid in many approaches to making future analysis quantitative. Therefore, further careful examination of the LIBS plasma dynamics under Martian atmospheric pressures must be studied.

Chapter 8 : Conclusions and Future Work

This work addressed the study of two plasma spectroscopic techniques for the analysis of biological and environmental matrices. These methods included SIBS applied to the study of bioaerosols as well as the development of a portable SIBS analyzer for the measurement of carbon in soils. In addition, LIBS was studied to compare various atmospheric conditions, and the effect on plasma formation and spectral analysis. Conclusions and future work are presented for each set of experiments in the following sections.

8.1 The Development of a Portable SIBS Analyzer

This study encompassed several experiments towards the development of a soil carbon analyzer. The initial experiments described in Chapter 4 resulted in the development of sample delivery hardware to the spark gap of the SIBS instrument, and preliminary data analysis that demonstrated the possibility of the application of SIBS to a portable soil carbon monitor. The neutral carbon line in the 248 nm spectral region was used throughout this research to quantify carbon in soils. Local soil samples were collected and characterized for total carbon. Subsets of the SIBS spectra of these characterized soils were subjected to a variety of univariate and multivariate data analyses. Using SIBS and partial least squares fitting with 3-5 latent variables, an estimate of total carbon in soil over a range of 0.71 – 3.64 % with a detection limit of

between 0.2-0.3 % by dry weight was achieved. Although a small sample set was used for this experiment, reasonable results were found.

Chapter 5 included results built on the fundamental research found in Chapter 4. During this phase, several surrogate soils were analyzed in order to study signal response of C (organic, inorganic and elemental) and Fe as a function of concentration. These results provided information on the limitations of the current screw-feed design, as well as the linear range of C and Fe. In addition, several soils were collected and characterized for TC, OC and IC. Three soils were used to study the effects of particle size on signal reproducibility. It was determined that the particle size does play a role in the shot-to-shot variability and reproducibility. PLS analysis was performed on a small sample set of soils, and produced a good correlation between the predicted and measured carbon concentrations ($R^2 = 0.927$). Metal analysis was performed (ICP-OES) on the soils, and the concentrations of Si and Fe were determined. Fe and Si were included in the PLS model, because of their spectral dominance in the 248 nm region. Additionally, these elements were modeled to better understand the spectral response on the prediction of carbon. It was determined by including Fe and Si in the model in addition to C, the prediction of C was not improved. Thus, Fe and Si were not included in subsequent models throughout this research.

A portable SIBS analyzer was built by our collaborators at PSI, and tested using a small sample set of soils. Initially, a comparison was made between the early data collected using the SIBS instrumentation, and the first prototype. The purpose of this research was to ensure that the new instrumentation functioned properly, and that the

portable instrument provided C predictions similar or better than in previous studies. This limited data set resulted in producing a good correlation between the predicted and measured carbon concentrations ($R^2 = 0.98$). There was an overall improvement in the predictions seen in the portable analyzer when compared to the initial data collected at PSI. Furthermore, the 350 nm to 400 nm spectral region containing the CN (B-X) molecular feature was included to predict the fraction of organic carbon. As a result, the fraction of inorganic carbon was also predicted. This preliminary model of TC, IC and OC demonstrate that it may be possible to predict these fractions of soil using SIBS instrumentation.

Future work will include testing a large soil data set in order to expand and validate the current preliminary model using a portable SIBS soil analyzer prototype. These soils will have a broad range of TC in order to better characterize the values of the accuracy, precision, LOD and LOQ of the instrument. In total, 100 well-characterized soil samples will be tested to validate an improved SIBS instrument prototype. Once all 100 samples are analyzed, the chosen spectral windows to predict C in soil will be re-evaluated. Having a large sample set will provide more data to confirm our initial spectral regions of interest. The continuation of the evaluation of spectral windows will also allow the discrimination of signals related to the presence of organic carbon from inorganic carbon. The main purpose behind this research was to quantify TC in soil in order to verify the use of soils as land-sinks for carbon dioxide from the atmosphere. The current gold standard in quantifying total carbon in soil is through CHN. Additional, labor intensive, analyses are performed in order to also quantify the fractions of OC and

IC in soils. If SIBS can provide a method to determine TC, OC and IC in soils, then this will provide a portable, rapid technique for the determination of carbon in soils. To accurately determine changes in soil C, and consequently monitor soil carbon sequestration, an accurate, robust, and portable instrument must be developed. SIBS is a promising and potentially field-deployable instrument for the measurement of C in soil.

8.2 The Use of SIBS to Study Bioaerosols

The purpose of this research was to apply SIBS to the study of bioaerosols. First, the electrode position with relation to the collection optics was studied as part of the overall fundamental understanding of SIBS technology as it relates to plasma formation. Thus, the basic understanding of how the spectral signals behaved at different focused regions of the plasma is crucial for the optimization of SIBS. The data presented in Chapter 6 indicated that by focusing on the hot electrode (energized electrode), a full intensity profile of calcium could be obtained. This is important when determining the optimal data acquisition profile for the elements of interest. This research also illustrates the importance of how the position of the optics effects the collection of irradiation produced from SIBS signals. It was observed that by focusing on the hot electrode, molecular features were observed. The different time profiles achieved while focusing at different probed volume of the plasma indicates that the plasma is not homogenous. This is also evident in the fact that no molecular features were observed when focused on the ground electrodes in the preliminary data.

Second, the preliminary work provided data that illustrated the integrated emission strength has a relationship with independently established elemental composition measurements. For example, there was a linear dependence between the temporally integrated calcium feature strength compared to the concentration determined through an external laboratory. Additionally, it has been observed in this small and preliminary data set that the CN (B–X) emission has a linear relationship with the nitrogen content of the sample as determined with combustion analysis.

The SIBS instrumentation used during this research did not prevent the deposition of particles on the electrodes. Preliminary research on the use of a SIBS sheath flow system, seen in Figure 8.1, has been investigated. The sheath flow system is attached to the bottom of the heated drying column, and takes the place of the spark chamber. The sheath flow system allows for a 2 to 3 mm collimated particle stream to flow through the electrodes through a proper flow balance of air. First, the collimated particle stream will reduce the agglomeration of particles on the electrodes, which in turn, will reduce contamination and carry over from sample to sample. The use of this system will allow the determination of particle mass at any given time in the spark gap. In addition, no research has been reported on the complete vaporization of individual particles. Thus, this system would be used to determine the upper size limit for the complete particle size vaporization. Researchers in the LIBS community have reported the upper size limit for complete vaporization. For example, Carranza and Hahn studied a range of silica particles which consisted of 1.0 to 5.1 μm [151]. They reported an upper size limit of 2.1 μm diameter silica particle for a laser pulse energy of 320 mJ, as determined by the

deviation from a linear mass response of the silicon atomic emission signal [151]. These results depend on the laser pulse energy, and in turn, would also depend on the spark energy used during these experiments. However, these results would provide an understanding on the upper particle size vaporization limit using SIBS.

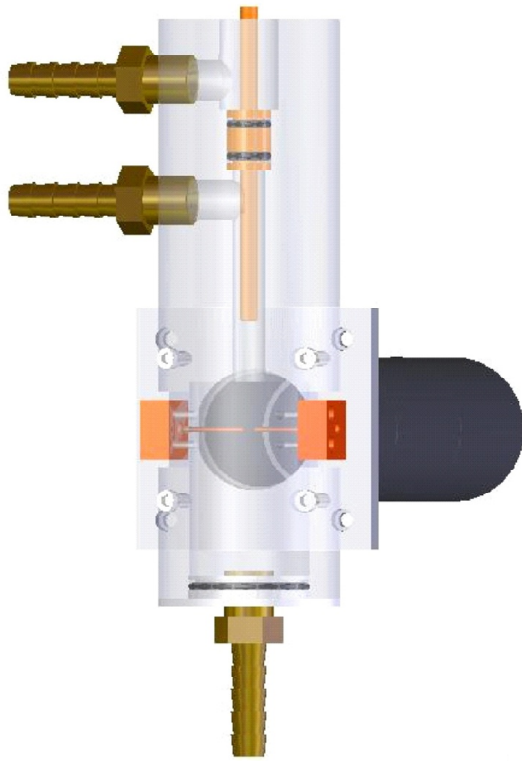


Figure 8.1 Diagram of the sheath flow design.

8.3 Plasma Dynamics as a Function of Pressure and Atmospheric Composition

The purpose of this research was to illustrate that the atmospheric conditions found on Mars show significant effects on plasma. Comparisons were made in the spectra of hematite collected in a pure CO₂ atmosphere and a Mars-simulated atmosphere under different pressures. First, the preliminary studies included the modeling of the Ca II linewidth at 396.86 nm as a function of pressure under CO₂. Peak intensity of this line was also studied as a function of pressure. Photographs of the plasma size under varying pressure were also analyzed through Photoshop. Second, linewidths, intensities and plasma size were studied under a Mars-simulated atmosphere and compared to the results found under a pure CO₂ atmosphere. The results from this study did not produce clear statistical differences in both the line widths and or plasma size between the CO₂ and Mars atmospheres. However, it is evident that analyte signals (linewidths and intensities) are strongly dependent on pressure. Results from this study indicate that there is a significant change in plasma expansion as a function of pressure. In addition, the compositional differences between Mars atmosphere and Earth atmosphere affect the plasma expansion and lifetime of plasma due to thermal conductivity. Thus, the plasma expansion affects the ability to capture the full plasma at low pressures through fiber optics. This research demonstrated that that plasma formation and emission depend on several factors including pressure, gate width and delay, and the composition of the surrounding atmosphere to name a few. Therefore, quantifying elemental composition in geological formations on Mars is a challenge.

Further research should be performed to collect more data to establish reproducibility and sources of variance, and confirm the preliminary findings. In addition, comparisons between elemental composition and peak intensities and widths should be made. This information will provide a better understanding as to how neutral and ionized lines behave under atmospheric conditions similar to Mars. This information is pertinent in order to build calibration curves, and therefore, determine concentrations of geological formations on Mars. The change in plasma dynamics between 0.1 and 10 T under a Mars-simulated atmosphere in comparison to CO₂ alone is significant for Mars exploration. As expected, the linewidths did not increase linearly, and further studies should be conducted to better understand and identifying the nature of this relationship. Future research should also include a comparison of delay times for LIBS spectral optimization as well as a comparison between elemental composition and peak intensities. The optimization of the optical collection in relation to the plasma expansion should be performed. These studies will aid in many approaches to making future analysis quantitative. Therefore, further careful examination of the LIBS plasma dynamics under Martian atmospheric pressures must be studied.

Works Cited

1. Skoog, H.a.C., *Principles of Instrumental Analysis*. Sixth ed. 2007: Thomson Brooks/Cole.
2. Thorne, A.P., *Spectrophysics*. 1974, London: Chapman and Hall Ltd.
3. Broekaert, J.A.C., *Analytical Atomic Spectroscopy with Flames and Plasmas*. 2002: Wiley-VCH.
4. Singh, J.P., Thakur, Surya N., *Laser-induced breakdown spectroscopy*. 1st ed. 2007, Amsterdam ; Boston: Elsevier.
5. Cremers, D.A. and L.J. Radziemski, *Handbook of laser-induced breakdown spectroscopy*. 2006, Chichester, West Sussex, England ; Hoboken, NJ: John Wiley & Sons.
6. Piper, A.J.R.H.a.L.G., *Spark-induced breakdown spectroscopy: a description of an electrically generated LIBS-like process for elemental analysis of airborne particulates and solid samples*, in *Laser-Induced Breakdown Spectroscopy: Fundamentals and Applications*, V.P.a.I.S. Andrzej W. Miziolek, Editor. 2006, Cambridge University Press.
7. Gallou, G., et al., *Aerosols Analysis by LIBS for Monitoring of Air Pollution by Industrial Sources*. *Aerosol Science and Technology*, 2011. **45**(8): p. 918-926.
8. Hunter, A.J.R., et al., *Continuous emissions monitoring using spark-induced breakdown spectroscopy*. *Journal of the Air & Waste Management Association*, 2000. **50**(1): p. 111-117.
9. Park, K., G. Cho, and J.H. Kwak, *Development of an Aerosol Focusing-Laser Induced Breakdown Spectroscopy (Aerosol Focusing-LIBS) for Determination of Fine and Ultrafine Metal Aerosols*. *Aerosol Science and Technology*, 2009. **43**(5): p. 375-386.
10. Boyain-Goitia, A.R., et al., *Single-pollen analysis by laser-induced breakdown spectroscopy and Raman microscopy*. *Applied Optics*, 2003. **42**(30): p. 6119-6132.
11. Samuels, A.C., et al., *Laser-induced breakdown spectroscopy of bacterial spores, molds, pollens, and protein: initial studies of discrimination potential*. *Applied Optics*, 2003. **42**(30): p. 6205-6209.
12. Hunter, A.J.R., et al., *Rapid field screening of soils for heavy metals with spark-induced breakdown spectroscopy*. *Applied Optics*, 2003. **42**(12): p. 2102-2109.
13. Dell'Aglio, M., et al., *Monitoring of Cr, Cu, Pb, V and Zn in polluted soils by laser induced breakdown spectroscopy (LIBS)*. *Journal of Environmental Monitoring*, 2011. **13**(5): p. 1422-1426.
14. Schmidt, M.S., et al., *Spark-induced breakdown spectroscopy (SIBS) for elemental analysis of soil and the development of a fieldable soil carbon monitor*. *Abstracts of Papers of the American Chemical Society*, 2011. **242**.
15. Martin, M.Z., et al., *Novel Multivariate Analysis for Soil Carbon Measurements Using Laser-Induced Breakdown Spectroscopy*. *Soil Science Society of America Journal*, 2010. **74**(1): p. 87-93.

16. Hunter, A.J.R., et al., *Spark-induced breakdown spectroscopy: A new technique for monitoring heavy metals*. Applied Spectroscopy, 2000. **54**(4): p. 575-582.
17. Schmidt, M.S. and A.J.R. Bauer, *Preliminary correlations of feature strength in spark-induced breakdown spectroscopy of bioaerosols with concentrations measured in laboratory analyses*. Applied Optics, 2010. **49**(13): p. C101-C109.
18. Schmidt, M.S., et al., *Spark-induced breakdown spectroscopy and multivariate analysis applied to the measurement of total carbon in soil*. Applied optics, 2012. **51**(7): p. B176-82.
19. Fraser, M.E., et al., *Fugitive emission measurements above a hard chromium plating tank using spark-induced breakdown spectroscopy (SIBS)*. Plating and Surface Finishing, 2000. **87**(1).
20. Miziolek, A.W., V. Palleschi, and I. Schechter, *Laser-induced breakdown spectroscopy (LIBS) : fundamentals and applications*. 2006, Cambridge, UK ; New York: Cambridge University Press.
21. Ogle, S.M., et al., *Uncertainty in estimating land use and management impacts on soil organic carbon storage for US agricultural lands between 1982 and 1997*. Global Change Biology, 2003. **9**(11): p. 1521-1542.
22. Kutsch, W., M. Bahn, and A. Heinemeyer, *Soil carbon dynamics : an integrated methodology*. 2009, Cambridge, UK ; New York: Cambridge University Press. xi, 286 p.
23. Purakayastha, T.J., et al., *Long-term impact of fertilizers on soil organic carbon pools and sequestration rates in maize-wheat.-cowpea cropping system*. Geoderma, 2008. **144**(1-2): p. 370-378.
24. Verheijen, F.G.A., et al., *Organic carbon ranges in arable soils of England and Wales*. Soil Use and Management, 2005. **21**(1): p. 2-9.
25. Ebinger, M.H., et al., *Extending the applicability of laser-induced breakdown spectroscopy for total soil carbon measurement*. Soil Science Society of America Journal, 2003. **67**(5): p. 1616-1619.
26. Scholes, R.J. and I.R. Noble, *Climate change - Storing carbon on land*. Science, 2001. **294**(5544): p. 1012-1013.
27. Fabre, C., et al., *Onboard calibration igneous targets for the Mars Science Laboratory Curiosity rover and the Chemistry Camera laser induced breakdown spectroscopy instrument*. Spectrochimica Acta Part B-Atomic Spectroscopy, 2011. **66**(3-4): p. 280-289.
28. Cousin, A., et al., *Laser induced breakdown spectroscopy library for the Martian environment*. Spectrochimica Acta Part B-Atomic Spectroscopy, 2011. **66**(11-12): p. 805-814.
29. Tillman, J.E., *Mars Global Atmospheric Oscillations - Annually Synchronized, Transient Normal - Mode Oscillations and the Triggering of Global Dust Storms*. Journal of Geophysical Research-Atmospheres, 1988. **93**(D8): p. 9433-9451.
30. Burakov, V.S., et al., *Development of a Laser-Induced Breakdown Spectroscopy Method for Soil and Ecological Analysis (Review)*. Journal of Applied Spectroscopy, 2010. **77**(5): p. 595-608.

31. Cremers, D.A., et al., *Measuring total soil carbon with laser-induced breakdown spectroscopy (LIBS)*. Journal of Environmental Quality, 2001. **30**(6): p. 2202-2206.
32. Martin, M.Z., et al., *Laser-induced breakdown spectroscopy for the environmental determination of total carbon and nitrogen in soils*. Applied Optics, 2003. **42**(12): p. 2072-2077.
33. Madhavi Martin, S.W., and Charles Garten Jr., *Laser-induced breakdown spectroscopy for environmental monitoring of soil carbon and nitrogen*. Proceedings of SPIE 2002. **4576**: p. 188-195.
34. Belkov, M.V., et al., *Comparison of two laser-induced breakdown spectroscopy techniques for total carbon measurement in soils*. Spectrochimica Acta Part B-Atomic Spectroscopy, 2009. **64**(9): p. 899-904.
35. Glumac, N.G., W.K. Dong, and W.M. Jarrell, *Quantitative Analysis of Soil Organic Carbon Using Laser-Induced Breakdown Spectroscopy: An Improved Method*. Soil Science Society of America Journal, 2010. **74**(6): p. 1922-1928.
36. Gibb-Snyder, E., et al., *Development of size-selective sampling of Bacillus anthracis surrogate spores from simulated building air intake mixtures for analysis via laser-induced breakdown spectroscopy*. Applied Spectroscopy, 2006. **60**(8): p. 860-870.
37. Kim, K.W., *Physico-chemical characteristics of visibility impairment by airborne pollen in an urban area*. Atmospheric Environment, 2007. **41**(17): p. 3565-3576.
38. Menetrez, M.Y., et al., *An evaluation of the protein mass of particulate matter*. Atmospheric Environment, 2007. **41**(37): p. 8264-8274.
39. Matthias Maser, S. and R. Jaenicke, *The size distribution of primary biological aerosol particles with radii >0.2 μ m in an urban rural influenced region*. Atmospheric Research, 1995. **39**(4): p. 279-286.
40. Morel, S., et al., *Detection of bacteria by time-resolved laser-induced breakdown spectroscopy*. Applied Optics, 2003. **42**(30): p. 6184-6191.
41. Hybl, J.D., G.A. Lithgow, and S.G. Buckley, *Laser-induced breakdown spectroscopy detection and classification of biological aerosols*. Applied Spectroscopy, 2003. **57**(10): p. 1207-1215.
42. Munson, C.A., et al., *Investigation of statistics strategies for improving the discriminating power of laser-induced breakdown spectroscopy for chemical and biological warfare agent simulants*. Spectrochimica Acta Part B-Atomic Spectroscopy, 2005. **60**(7-8): p. 1217-1224.
43. Gottfried, J.L., et al., *Multivariate analysis of laser-induced breakdown spectroscopy chemical signatures for geomaterial classification*. Spectrochimica Acta Part B-Atomic Spectroscopy, 2009. **64**(10): p. 1009-1019.
44. Cahoon, E.M. and J.R. Almirall, *Wavelength dependence on the forensic analysis of glass by nanosecond 266 nm and 1064 nm laser induced breakdown spectroscopy*. Applied Optics, 2010. **49**(13): p. C49-C57.
45. Rodriguez-Celis, E.M., et al., *Laser induced breakdown spectroscopy as a tool for discrimination of glass for forensic applications*. Analytical and Bioanalytical Chemistry, 2008. **391**(5): p. 1961-1968.

46. Baudelet, M., et al., *Spectral signature of native CN bonds for bacterium detection and identification using femtosecond laser-induced breakdown spectroscopy*. Applied Physics Letters, 2006. **88**(6): p. 3.
47. Merdes, D.W., et al., *The investigation of laser-induced breakdown spectroscopy for detection of biological contaminants on surfaces*. Spectroscopy, 2007. **22**(4): p. 28-38.
48. Dreyer, C.B., et al., *Study of sub-mJ-excited laser-induced plasma combined with Raman spectroscopy under Mars atmosphere-simulated conditions*. Spectrochimica Acta Part B-Atomic Spectroscopy, 2007. **62**(12): p. 1448-1459.
49. Buhler, C.R., Calle, C.I., Nelson, E., *Electrical Breakdown in a Martian Gas Mixture*. 2003.
50. Manning, H.L.K., et al., *Electric discharge in the Martian atmosphere, Paschen curves and implications for future missions*. Advances in Space Research, 2010. **46**(10): p. 1334-1340.
51. Bunsen, G.R.K.a.R., *Chemical analysis by spectrum-observation*, in *Philosophical Magazine*. 1860. p. 89-98.
52. Levine, I.N., *Quantum Chemistry*. Fifth ed. 2000, Upper Saddle River, New Jersey: Prentice-Hall, Inc.
53. Mika, T.T.a.J., *Analytical Emission Spectroscopy: Fundamentals*. 1974: Crane, Russak & Company, Inc.
54. Seth, S., *Quantum theory and the electromagnetic world-view*. Historical Studies in the Physical and Biological Sciences, 2004. **35**: p. 67-93.
55. Hoffmann, K.H., *Quantum thermodynamics*. Annalen Der Physik, 2001. **10**(1-2): p. 79-88.
56. Turro, N.J., V. Ramamurthy, and J.C. Scaiano, *Principles of molecular photochemistry : an introduction*. 2009, Sausalito, Calif.: University Science Books. xxi, 495 p.
57. Hobart H. Willard, L.L.M., Jr., John A. Dean, Frank A. Settle, Jr., *Instrumental Methods of Analysis*. Seventh Edition ed. 1988: Wadsworth, Inc.
58. Herzberg, G., *Molecular spectra and molecular structure*. 2d ed. 1950, New York,: Van Nostrand. v.
59. De Giacomo, A., et al., *The role of continuum radiation in laser induced plasma spectroscopy*. Spectrochimica Acta Part B-Atomic Spectroscopy, 2010. **65**(5): p. 385-394.
60. Pebay-Peyroula, B.C.a.J.C., *Modern Atomic Physics: Fundamental Principles*. 1971, New York - Toronto: John Wiley & Sons.
61. Griem, H.R., *Spectral line broadening by plasmas*. 1974, New York: Academic Press.
62. Griem, H.R., *Plasma Spectroscopy*. 1964, New York: McGraw-Hill Inc.
63. Herzberg, G., *Atomic Spectra and Atomic Structure*. 1944, New York: Dover Publications.
64. Diedrich, J., *Laser-induced breakdown spectroscopy on bacterial samples*, in *Physics*. 2007, Wayne State University: Detroit.

65. Kondratyev, V., *The Structure of Atoms and Molecules*. 1964, Groningen P. Noordhoff N.V.
66. Huhn, H.G., *Atomic Spectra*. 1969, New York and London: Academic Press.
67. Morgan, C.G., *Laser-induced breakdown of gases*. Rep. Prog. Phys., 1975. **38**: p. 621-665.
68. Ready, J.F., *Effect of High Power Laser Radiation*. 1971, New York: Academic Press.
69. Salamin, Y.I., et al., *Relativistic high-power laser-matter interactions*. Physics Reports-Review Section of Physics Letters, 2006. **427**(2-3): p. 41-155.
70. Salzmann, D., *Atomic Physics in Hot Plasmas*. International Series of Monographs on Physics 97. 1998, New York: Oxford University Press.
71. Radziemski, L.J. and D.A. Cremers, *Laser-induced plasmas and applications*. Optical Engineering. 1989, New York: M. Dekker. xiv, 445 p.
72. Lee Y., S.K., Sneddon J., *Laser Induced Plasmas for Analytical Spectroscopy*, in *Lasers in Analytical Atomic Spectroscopy*, T.T.L. Sneddon J., Lee Y., Editor. 1997, VCH publishers Inc: New York.
73. Milán M., L.J.J., *Diagnostics of silicon plasmas produced by visible nanosecond laser ablation*. spectrochimica Acta Part B, 2001. **56**: p. 275-288.
74. Shaikh N.M., R.B., Hafeez S., Jamil Y., Baig M.A., *Measurement of electron density and temperature of a laser-induced zinc plasma*. Journal of Physics D: Applied Physics, 2006. **39**: p. 1384-1391.
75. B. Le Drogoff, J.M., M. Chaker, M. Sabsabi, O. Barthelemy, T.W. Johnston, S. Larville, F. Vidal, Y. von Kaenel, *Temporal characterization of femtosecond laser pulses induced plasma for spectrochemical analysis of aluminum alloys*. Spectrochimica Acta Part B, 2001. **56**: p. 987-1002.
76. Aragon, C. and J.A. Aguilera, *Characterization of laser induced plasmas by optical emission spectroscopy: A review of experiments and methods*. Spectrochimica Acta Part B-Atomic Spectroscopy, 2008. **63**(9): p. 893-916.
77. McWhirter, R.W.P. and *Spectral intensities*, in *Plasma Diagnostic Techniques*, S.L.L. R.H. Huddleston, Editor. 1965, Academic Press.
78. Harmon, R.S., et al., *LIBS analysis of geomaterials: Geochemical fingerprinting for the rapid analysis and discrimination of minerals*. Applied Geochemistry, 2009. **24**(6): p. 1125-1141.
79. Robert, P., et al., *Optimization of micro-Laser Induced Breakdown Spectroscopy analysis and signal processing*. Spectrochimica Acta Part B-Atomic Spectroscopy, 2008. **63**(10): p. 1109-1116.
80. Eland, K.L., et al., *Energy dependence of emission intensity and temperature in a LIBS plasma using femtosecond excitation*. Applied Spectroscopy, 2001. **55**(3): p. 286-291.
81. Hohreiter, V., J.E. Carranza, and D.W. Hahn, *Temporal analysis of laser-induced plasma properties as related to laser-induced breakdown spectroscopy*. Spectrochimica Acta Part B-Atomic Spectroscopy, 2004. **59**(3): p. 327-333.
82. Camacho, J.J., et al., *Time-resolved optical emission spectroscopy of laser-produced air plasma*. Journal of Applied Physics, 2010. **107**(8).

83. Ciucci, A., et al., *Trace pollutants analysis in soil by a time-resolved laser-induced breakdown spectroscopy technique*. Applied Physics B-Lasers and Optics, 1996. **63**(2): p. 185-190.
84. Sabsabi, M. and P. Cielo, *Quantitative-Analysis of Aluminum-Alloys by Laser-Induced Breakdown Spectroscopy and Plasma Characterization*. Applied Spectroscopy, 1995. **49**(4): p. 499-507.
85. H.C. Liu, X.L.M., J.H. Yoo, R. E. Russo, *Early phase laser induced plasma diagnostics and mass removal during single-pulse laser ablation of silicon*. Spectrochimica Acta Part B, 1999. **54**: p. 1607-1624.
86. D. Bulajic, M.C., G. Cristoferetti, S. Legnaioli, V. Palleschi, A. Salvetti, E. Tognoni, *A procedure for correcting self absorption in calibration free-laser induced breakdown spectroscopy*. Spectrochimica Acta Part B, 2002. **57**: p. 339-353.
87. Aragón, J.A.A.a.C., *Multi-element Saha-Boltzmann and Boltzmann plots in laser-induced plasmas*. Spectrochimica Acta Part B, 2007. **62**: p. 378-385.
88. Aragón, J.A.A.a.C., *Characterization of a laser-induced plasma by spactially resolved spectroscopy of neutral atom and ion emissions. Comparison of local and spactially integrated measurements*. Spectrochimica Acta Part B, 2004. **59**: p. 1861-1876.
89. M. Essien, L.J.R., J. Sneddon, *Detection of cadmium, lead and zinc in aerosols by laser-induced breakdown spectrometry*. Journal of Analytical Atomic Spectrometry, 1988. **3**: p. 985-988.
90. M.R. Joseph, N.X., V. Majidi, *Time-resolved emission characteristics and temperature profiles of laser-induced plasmas in helium*. Spectrochimica Acta Part B, 1994. **49**: p. 89-103.
91. Skole, R.A.H.a.D.L., *Carbon*, in *The earth as transformed by human action*, W.C.C. B.L. Turner II, R.W. Kates, J.F. Richards, J.T. Mathews and W.B. Meyer Editor. 1990, Cambridge University Press: Cambridge.
92. Dumanski, J., et al., *Possibilities for future carbon sequestration in Canadian agriculture in relation to land use changes*. Climatic Change, 1998. **40**(1): p. 81-103.
93. Davidson, E.A. and I.L. Ackerman, *Changes in Soil Carbon Inventories Following Cultivation of Previously Untilled Soils*. Biogeochemistry, 1993. **20**(3): p. 161-193.
94. Paustian, K., et al., *Agricultural soils as a sink to mitigate CO₂ emissions*. Soil Use and Management, 1997. **13**(4): p. 230-244.
95. Robert, M., *Soil Carbon Sequestration for Improved Land Management*. 2001: p. <ftp://ftp.fao.org/agl/agll/docs/wsr96e.pdf>.
96. Lee, J.J. and D.L. Phillips, *The Effect of Trends in Tillage Practices on Erosion and Carbon Content of Soils in the United States Corn-Belt*. Water Air and Soil Pollution, 1993. **70**(1-4): p. 389-401.
97. Barnwell, T.O., et al., *An Approach to Assessment of Management Impacts on Agricultural Soil Carbon*. Water Air and Soil Pollution, 1992. **64**(1-2): p. 423-435.

98. da Silva, R.M., et al., *Total carbon measurement in whole tropical soil sample*. Spectrochimica Acta Part B-Atomic Spectroscopy, 2008. **63**(10): p. 1221-1224.
99. Staff, S.S. *Web Soil Survey, National Resources Conservation Service*. [cited 2011 September 25]; Available from: <http://websoilsurvey.nrcs.usda.gov/>.
100. Blaisdell, R. (2003) *Recommended Procedures for Collecting, Processing, and Analyzing Soil Samples in CSMGS Research Plots*.
101. Soil and Plant Analysis Council, I., *Soil Analysis Handbook of Reference Methods* CRC. 1999, New York.
102. Sweedler, J.V., *Charge-Transfer Device Detectors and Their Applications to Chemical Analysis*. Critical Reviews in Analytical Chemistry, 1993. **24**(1): p. 59-98.
103. Reu, P.L. and B.D. Hansche, *Optical temporal frequency low-pass filtering and heterodyning with a microchannel plate*. Optical Engineering, 2008. **47**(7).
104. Portnov, A., S. Rosenwaks, and I. Bar, *Emission following laser-induced breakdown spectroscopy of organic compounds in ambient air*. Applied Optics, 2003. **42**(15): p. 2835-2842.
105. Wong, D.M. and P.J. Dagdigan, *Comparison of laser-induced breakdown spectra of organic compounds with irradiation at 1.5 and 1.064 μ m*. Applied Optics, 2008. **47**(31): p. G149-G157.
106. Ma, Q.L. and P.J. Dagdigan, *Kinetic model of atomic and molecular emissions in laser-induced breakdown spectroscopy of organic compounds*. Analytical and Bioanalytical Chemistry, 2011. **400**(10): p. 3193-3205.
107. Otto, M., *Chemometrics : statistics and computer application in analytical chemistry*. 2nd ed. 2007: Weinheim : Wiley-VCH ; Chichester : John Wiley [distributor].
108. Brereton, R.G., *Chemometrics : data analysis for the laboratory and chemical plant*. 2003: West Sussex: John Wiley & Sons.
109. Picard, R.R. and R.D. Cook, *Cross-Validation of Regression-Models*. Journal of the American Statistical Association, 1984. **79**(387): p. 575-583.
110. Wold, S., M. Sjostrom, and L. Eriksson, *PLS-regression: a basic tool of chemometrics*. Chemometrics and Intelligent Laboratory Systems, 2001. **58**(2): p. 109-130.
111. Schumacher, B.A., *Methods for the determination of total organic carbon (TOC) in soils and sediments*, E.R.A.S. Center, Editor. 2002, U.S. EPA: Las Vegas.
112. Ellert, B.H., H.H. Janzen, and T. Entz, *Assessment of a method to measure temporal change in soil carbon storage*. Soil Science Society of America Journal, 2002. **66**(5): p. 1687-1695.
113. Brereton, R.G., *Chemometrics: Data Analysis for the Laboratory and Chemical Plant*. 2003, West Sussex: Wiley.
114. Hanrahan, G., *Environmental Chemometrics: Principles and Modern Applications*. 2009: CRC Press.
115. Geladi, P. and B.R. Kowalski, *Partial Least-Squares Regression - A Tutorial*. Analytica Chimica Acta, 1986. **185**: p. 1-17.
116. Naes, H.M.a.T., *Multivariate Calibration*. 1989: John Wiley & Sons.

117. Savolainen, M., et al., *Determination of amorphous content in the pharmaceutical process environment*. Journal of Pharmacy and Pharmacology, 2007. **59**(2): p. 161-170.
118. Davis, R.A., et al., *Novel feature selection method for genetic programming using metabolomic (1)H NMR data*. Chemometrics and Intelligent Laboratory Systems, 2006. **81**(1): p. 50-59.
119. Chen, Q., et al., *Feasibility study on qualitative and quantitative analysis in tea by near infrared spectroscopy with multivariate calibration*. Analytica Chimica Acta, 2006. **572**(1): p. 77-84.
120. Divya, O. and A.K. Mishra, *Combining synchronous fluorescence spectroscopy with multivariate methods for the analysis of petrol-kerosene mixtures*. Talanta, 2007. **72**(1): p. 43-48.
121. Kuriakose, S., et al., *Detection and quantification of adulteration in sandalwood oil through near infrared spectroscopy*. Analyst, 2010. **135**(10): p. 2676-2681.
122. Luque, J., Crosley, D.R., *LIFBASE: Database and spectral simulation (version 1.5)*, in *SRI International Report*. 1999.
123. Pan, Y.L., et al., *A puff of air sorts bioaerosols for pathogen identification*. Aerosol Science and Technology, 2004. **38**(6): p. 598-602.
124. Gottfried, J.L., et al., *Standoff detection of chemical and biological threats using laser-induced breakdown spectroscopy*. Applied Spectroscopy, 2008. **62**(4): p. 353-363.
125. Y.L. Pan, J.H., R.G. Pinnick, R.G. Hill, S.C. Halverson, and R.K. Chang, *Single-particle fluorescence spectrometer for ambient aerosols*. Aerosol Science and Technology, 2003. **37**: p. 627-638.
126. Pan, Y.L., et al., *Characterizing and monitoring respiratory aerosols by light scattering*. Optics Letters, 2003. **28**(8): p. 589-591.
127. J.D. Eversole, W.K.C., C.S. Scotto, R. Pierson, M. Spence, and A.J. Campillo, *Continuous bioaerosol monitoring using UV excitation fluorescence: Outdoor test results*. Field Analytical Chemistry and Technology, 2001. **5**: p. 205-212.
128. Ho, J., *Future of Biological Aerosol Detection*. Analytica Chimica Acta, 2002. **457**: p. 125-148.
129. F. Pourahmadi, M.T., G. Kovacs, K. Loyd, S. Sakai, T. Schafer, B. Helton, L. Western, S. Zaner, J. Ching, B. McMillan, P. Belgrader and M.A. Northrup, *Toward a Rapid, Integrated, and Fully Automated DNA Diagnostic Assay for Chlamydia Trachomatis and Neisseria Gonorrhoeae*. Clinical Chemistry, 2000. **46**: p. 1151-1153.
130. C. Hagleitner, A.H., D. Lange, A. Kummer, N. Kerness, O. Brand and H. Baltes, *Smart Single-chip Gas Sensor Microsystem*. Nature, 2001. **414**: p. 293-296.
131. DeLucia, F.C., et al., *Laser-induced breakdown spectroscopy (LIBS): A promising versatile chemical sensor technology for hazardous material detection*. Ieee Sensors Journal, 2005. **5**(4): p. 681-689.
132. Diedrich, J., S.J. Rehse, and S. Palchadhuri, *Pathogenic Escherichia coli strain discrimination using laser-induced breakdown spectroscopy*. Journal of Applied Physics, 2007. **102**(1).

133. Baudelet, M., et al., *Femtosecond time-resolved laser-induced breakdown spectroscopy for detection and identification of bacteria: A comparison to the nanosecond regime*. Journal of Applied Physics, 2006. **99**(8): p. 9.
134. Sono-tek. [cited 2012 March 25, 2012]; Available from: <http://www.sono-tek.com/ultrasonic-nozzle-technology/>.
135. Yu. Ralchenko, A.E.K., J. Reader, E.B. Saloman, J.E. Sansonetti, J.J. Curry, D.E. Kelleher, J.R. Fuhr, L. Podobedova, W.L. Wiese, and K. Olsen, *NIST Atomic Spectra Database, version 4*. 2010, National Institute of Standards and Technology: Gaithersburg.
136. Maurice, R.W.a.S. (2011) *The ChemCam instrument suite on the Mars Science Laboratory Rover curiosity: remote sensing by laser-induced plasmas*. Geochemical News **145**.
137. Sallé, B., et al., *Laser-induced breakdown spectroscopy for space exploration applications: Influence of the ambient pressure on the calibration curves prepared from soil and clay samples*. Spectrochimica Acta Part B-Atomic Spectroscopy, 2005. **60**(4): p. 479-490.
138. Yalçın, S., Y.Y. Tsui, and R. Fedosejevs, *Pressure dependence of emission intensity in femtosecond laser-induced breakdown spectroscopy*. Journal of Analytical Atomic Spectrometry, 2004. **19**(10): p. 1295-1301.
139. Radziemski, L., et al., *Use of the vacuum ultraviolet spectral region for laser-induced breakdown spectroscopy-based Martian geology and exploration*. Spectrochimica Acta Part B-Atomic Spectroscopy, 2005. **60**(2): p. 237-248.
140. Arp, Z.A., et al., *Feasibility of generating a useful laser-induced breakdown spectroscopy plasma on rocks at high pressure: preliminary study for a Venus mission*. Spectrochimica Acta Part B-Atomic Spectroscopy, 2004. **59**(7): p. 987-999.
141. Effenberger, A.J., Jr. and J.R. Scott, *Effect of Atmospheric Conditions on LIBS Spectra*. Sensors, 2010. **10**(5): p. 4907-4925.
142. Fortes, F.J. and J.J. Laserna, *The development of fieldable laser-induced breakdown spectrometer: No limits on the horizon*. Spectrochimica Acta Part B-Atomic Spectroscopy, 2010. **65**(12): p. 975-990.
143. Bibring, J.P., et al., *Mars surface diversity as revealed by the OMEGA/Mars Express observations*. Science, 2005. **307**(5715): p. 1576-1581.
144. Corsi, M., et al., *Effect of laser-induced crater depth in laser-induced breakdown spectroscopy emission features*. Applied Spectroscopy, 2005. **59**(7): p. 853-860.
145. Diaz Pace, D.M., et al., *Analysis of Minerals and Rocks by Laser-Induced Breakdown Spectroscopy*. Spectroscopy Letters, 2011. **44**(6): p. 399-411.
146. Colao, F., et al., *LIBS application for analyses of martian crust analogues: search for the optimal experimental parameters in air and CO2 atmosphere*. Applied Physics a-Materials Science & Processing, 2004. **79**(1): p. 143-152.
147. Bogaerts, A., et al., *Laser ablation for analytical sampling: what can we learn from modeling?* Spectrochimica Acta Part B-Atomic Spectroscopy, 2003. **58**(11): p. 1867-1893.

148. Mao, X.L. and R.E. Russo, *Observation of plasma shielding by measuring transmitted and reflected laser pulse temporal profiles*. Applied Physics a-Materials Science & Processing, 1997. **64**(1): p. 1-6.
149. Vadillo, J.M., et al., *Effect of plasma shielding on laser ablation rate of pure metals at reduced pressure*. Surface and Interface Analysis, 1999. **27**(11): p. 1009-1015.
150. Brennetot, R., et al., *Mars analysis by laser-induced breakdown spectroscopy (MALIS): Influence of mars atmosphere on plasma emission and study of factors influencing plasma emission with the use of Doehlert designs*. Applied Spectroscopy, 2003. **57**(7): p. 744-752.
151. Carranza, J.E. and D.W. Hahn, *Assessment of the upper particle size limit for quantitative analysis of aerosols using laser-induced breakdown spectroscopy*. Analytical Chemistry, 2002. **74**(21): p. 5450-5454.